Doctoral Dissertation

Numerical analyses of chemical reaction dynamics in plasma-irradiated phosphate-buffered saline (PBS) solutions

A thesis presented for the degree of
Doctor of Philosophy

Enggar Alfianto

July 2025

International Priority
Graduate Program on Applied and Engineering Physics,
Division of Precision Engineering and Applied Physics,
Graduate School of Engineering,
The University of Osaka
Japan

Abstract

The interaction between liquids and plasmas has been studied extensively in recent decades, driven by the burgeoning applications of atmospheric-pressure plasmas to the fields of medicine and biology. Plasma-based medical therapies necessitate a thorough understanding of plasma-liquid interactions, as most living cells are enveloped by fluids that mediate the plasma's contact with cells. Plasma interaction with liquids generates a plethora of reactive oxygen and nitrogen species (RONS). RONS are typically categorized into fast-reacting and slow-reacting species based on their reaction rates. Observation of fast-reacting RONS in a liquid phase, however, poses significant experimental challenges because their reactions are too fast to be observed optically. Furthermore, if fast-reacting RONS enter the liquid from the gas phase, their reactions typically take place in a very thin layer with a depth of about 1 μm at the gas-liquid interface (i.e., the liquid surface). Therefore, for a better understanding of the dynamics and chemical reactions of RONS in a liquid phase, sophisticated computational simulations are needed to unravel the intricate mechanisms of plasma-liquid interactions.

To investigate the critical reaction pathways in plasma-liquid interactions, this study utilized two simulation methodologies: a global (0-dimensional or 0D) model focusing on liquid-phase chemical reactions and a 1D model incorporating liquid-phase reactions and transport phenomena. The liquid of interest in this study was phosphate-buffered saline (PBS), in which the pH value stays at 7, and chlorine ions (Cl^+) typically produce hypochlorous acid (HOCl) when the solution is exposed to a plasma. This study initially investigated the influence of charge-neutral RONS generated in plasmas on chemical reactions within a PBS solution. Subsequently, the impact of time-dependent fluxes of electrically charged species (i.e., electrons and ions) on chemical reactions in a PBS solution was examined.

The global model investigation of neutral species unraveled two crucial reaction pathways leading to hydrogen peroxide (H_2O_2) decomposition by Cl^+ in PBS solutions; one is the "direction decomposition of hypochlorite ion (ClO^-)" and the other is the "chlorine monoxide (ClO) cycle." The 1D reaction-transport simulation also found that these were the main decomposition mechanisms for H_2O in a PBS solution, providing spatial resolution of reaction events within the solution. The study also examined liquid-phase chemical reaction dynamics for pulsed plasma discharges and demonstrated that the influxes of electrons and ions to a PBS solution led to the generation of stable chemical species such as H_2O_2, NO_2, and $NO_2{}^-$. Although electrons and ions are typically fast-reacting species, the overall reactions were found to be slow, and, therefore, pulsed discharges and steady-state fluxes of charged species caused similar effects on the generation of slow-reacting stable chemical species in a PBS solution.

Keywords: Plasma-liquid interactions, Reactive oxygen and nitrogen species (RONS), Global model, Reaction-transport simulation, PBS-like solution, H_2O_2, Chlorine monoxide cycle, Charged species, Pulse discharge, Continuous discharge

Dedication

For Ami, Yasa, Yuka , Hartono Family and Habib Family

Acknowledgement

During my PhD at the Osaka University, I have had the good fortune to work with many amazing people, and I can only begin to thank them here. First, I would like to thank my advisor, Prof. Satoshi Hamaguchi. He has always taken the time to give me advice when I needed it, and has been incredibly supportive of all of my goals. He is an inspiration through his hard work and his dedication to all of his students as well as the broader research community.

I would like to express my sincere gratitude to the staff at the Hamaguchi Lab for always providing us with their best assistance. I am particularly thankful to Ikuse-san, Umemura-san, Ito-san, Isobe-san, Nagao-san, and Yano-san for their invaluable support. During my time in Japan, I have learned a great deal about Japanese culture, which I have come to appreciate for its emphasis on politeness, sincerity, and thoroughness. I am also grateful for the guidance and advice you have provided me, which has instilled in me a strong desire to return to Japan in the future. It has been an honor to meet such kind and exceptional individuals.

During my stay in Osaka, Professor Hamaguchi also introduced me to his exceptional and highly inspiring colleagues. I am particularly grateful to Professor Zoltan Donko for his willingness to collaborate, guide, and support me on my third project. I hope to have the opportunity to collaborate with you again on future research endeavors. I would also like to express my gratitude to Professor Štefan Matejčík for his warm welcome during my time in Slovakia and for the stimulating discussions we had about research.

I would also like to extend my gratitude to all my lab-mates, past and present, for many insightful conversations, collaborations, and hiking talks. I have learned so much from each of you and I am grateful for all the time we have spent together. Thanks to Anjar, Nicolas, Charise, Erin, Abdul, Jaber, Nina, Jomar, Kawabata-

kun, Taira-kun, Hojun, Kita-kun, Ichikawa-kun, Sarah, Pierre, and all students in Hamaguchi lab.

Last but not least, I would also like to express my sincere gratitude to Dr. Febdian for paving the way for me to pursue my doctoral studies at Osaka University. Finally, I would like to extend my heartfelt appreciation to the Indonesian students in Japan, especially those in Osaka, who have become my extended family. They have provided invaluable support during challenging times, such as the COVID-19 pandemic. I cherish the memories of our shared sports activities, meals, and prayers at the mosque.

Contents

List of Figures

List of Tables

Chapter 1

Introduction

Plasma is the fourth state of matter, distinct from the three familiar states: solid, liquid, and gas. It is created by ionizing a gas, which means stripping electrons away from atoms, leaving them as positively charged ions. However, not all ionized gases are considered plasma. According to Francis F. Chen in his book "Introduction to Plasma Physics and Controlled Fusion," plasma is a quasi-neutral gas of charged and neutral particles that exhibit collective behavior.[40]

- Quasi-neutral means that the net charge of the plasma is approximately zero, with an equal number of positive and negative charges. However, this does not imply that there is no recombination between positive and negative charges. At certain conditions, such as low temperatures, recombination can occur, leading to a neutral charge state.

- Collective behavior refers to the tendency of charged particles in plasma to be influenced by other charged particles in their vicinity. This is in stark contrast to the behavior of neutral gas molecules, where particle motion is primarily affected by collisions.

In contrast to ordinary air, where molecules are neutral and collisions dictate their movement, plasma exhibits unique properties due to its charged nature:

- Current formation: Charged particles in plasma can move under the influence of electric and magnetic fields, creating electric currents.

- Magnetic field generation: The motion of charged particles in plasma can generate magnetic fields, which can further influence the behavior of the plasma itself and surrounding materials.

The term “plasma” was first introduced by Irving Langmuir in his 1928 publication in the Proceedings of the National Academy of Sciences. Langmuir, along with Tonks and their collaborators, conducted the initial research on plasma in the 1920s.[246] This research was driven by the need to develop vacuum tubes capable of storing large amounts of charge, which led to the investigation of gas ionization within these tubes. Their studies yielded the observation of a weakly ionized phenomenon with glowing charges. These early investigations laid the foundation for the utilization of plasma in semiconductor manufacturing, where it plays a crucial role in the etching process.

Subsequent advancements expanded the applications of plasma beyond its initial use in vacuum tubes. While most plasma is generated within vacuum systems, it can also be produced at atmospheric pressure. For instance, plasma jets utilizing argon and helium gases can be ionized using radio frequency power. This breakthrough enabled the development of pencil-sized devices that have found applications in the biomedical field.

1.1 Low temperature and atmospheric pressure plasma

The first recorded observation of low-temperature plasma (LTP) can be attributed to Jean (Félix) Picard in 1676. During his experiments with a barometer tube, Picard noticed a visible glow emanating from the tube. This glow was attributed to the friction between the tube and the mercury atoms within.[251] While the concept of plasma was not formally introduced until 1927 by Irving Langmuir, Picard’s observation laid the foundation for the understanding of LTP phenomena.

Low-temperature plasma (LTP) and atmospheric pressure plasma (APP) are essential for the utilization of plasma in medical applications. This is due to the sensitivity of biological cells to heat and the impracticality of subjecting them to low-pressure environments.[134, 132, 133] Several plasma generators are employed

in LTP and APP systems, including dielectric barrier discharge (DBD) and plasma jet. Plasma jets are particularly prevalent due to their portability and additional advantages.

In this study, a non-equilibrium atmospheric pressure plasma jet (NAPPJ) was employed. The plasma jet consisted of a 1 mm diameter tungsten electrode with a sharp tip, encased within a quartz tube having outer and inner diameters of 3 mm and 1.9 mm, respectively. The gas flow rate was maintained at 1.5 standard liters per minute (slm). The gases utilized were pure argon, argon with 0.27% humidified water, argon with 0.1% air, and argon with 0.1% oxygen.[240]

1.2 Plasma for medical and biological science

In recent years, plasma has emerged as a transformative force in the fields of medicine and biology. Its unique properties have propelled it to the forefront of innovative treatment strategies, offering distinct advantages over traditional chemical and other therapeutic methods. Plasma's remarkable attributes include:

- Minimally Invasive: Plasma therapy offers a non-invasive or minimally invasive approach, minimizing tissue damage and discomfort for patients.
- Broad-Spectrum Efficacy: Plasma exhibits a broad spectrum of therapeutic effects, effectively targeting a wide range of pathogens, including bacteria, viruses, and fungi.
- Faster Treatment Times: Plasma therapy often demonstrates accelerated healing and treatment times compared to conventional methods, leading to quicker patient recovery.

These compelling advantages have positioned plasma as a frontrunner in the development of next-generation treatment modalities for a variety of medical conditions, including:

- Wound Healing: Plasma therapy has demonstrated remarkable efficacy in promoting wound healing, accelerating tissue regeneration, and reducing inflammation.

- Cancer Treatment: Plasma's ability to selectively target cancer cells while minimizing harm to healthy tissues holds immense promise for cancer treatment.

- Antimicrobial Properties: Plasma's broad-spectrum antimicrobial activity offers a powerful tool against drug-resistant pathogens and infections.

The therapeutic applications of plasma in medicine are intrinsically linked to its interactions with cells. However, cells are typically surrounded by a complex biological fluid environment, posing a challenge for direct plasma-cell interactions. To overcome this barrier, plasma interacts with the surrounding fluid, which in turn mediates its effects on the target cells. This intricate interplay between plasma and liquid necessitates a deep understanding of plasma-liquid interactions, giving rise to a dedicated field of research.

Investigating plasma-liquid interactions is essential for comprehending the intricate mechanisms underlying plasma's therapeutic effects. Researchers employ a combination of experimental and simulation techniques to delve into this complex interplay. Among the various studies exploring plasma-liquid interactions, Wende et al.'s research on plasma interaction with PBS (phosphate-buffered saline) solution stands out. PBS, closely resembling human body fluids, serves as a surrogate environment to understand plasma's interactions before it encounters cells. Wende's study employed four different gas feed mixtures: pure argon, humidified argon (0.27%), to argon/oxygen (1%) and argon/air (1%).

Investigation by Wende et al.[240] reveals that the feed gas significantly impacts cell viability within PBS subjected to plasma irradiation. Apart from the feed gas, the distance between the jet tip and the solution also influences cell viability. Simulation results indicate that plasma emission generates various gas species. The density of the generated gas species is dependent on the feed gas. Additionally, the distance from the jet tip also affects the density of the generated species. This aligns with the theory that gases passing through the RF jet acquire charge. These charged gases subsequently interact or collide with air, producing charged species. Ultimately, the charged species react with oxygen and nitrogen in ambient air, forming reactive oxygen nitrogen species (RONS). RONS concentration varies in accordance with the jet tip distance.

Pre-existing RONS interact with PBS and infiltrate it, leading to subsequent reactions and the formation of new species. These newly formed species inevitably contain chlorine, as NaCl is a major component of PBS. Chlorine-related species are known to act as antimicrobial agents, suggesting that their presence likely influences the lifespan of cells within PBS. Additionally, hydrogen peroxide (H_2O_2), a common component of solutions, also plays a crucial role in determining cell viability. Understanding the reaction mechanisms within these solutions is both essential and challenging.

Direct observation of chemical reaction processes during plasma-liquid interactions is extremely challenging, if not impossible. This is due to the rapid formation and decomposition of numerous species within a short time-frame. To facilitate investigation, modeling and simulation tools are essential for elucidating the mechanisms governing plasma-liquid interactions.

1.3 Modelling

The inherent limitations of experimental techniques in capturing the intricacies of interspecies interactions necessitate the adoption of simulation-based approaches to address these shortcomings. Conventional investigative strategies for plasma-liquid interactions predominantly rely on global models (0D) and liquid simulations.

Global models (0D) represent a simplified modeling approach, assuming a homogeneous liquid phase, where the solution is considered to be rapidly and perfectly stirred. Despite their simplicity, global models can be effectively employed to analyze chemical reactions occurring within the solution induced by plasma-gas interactions. The goal of employing global models is to elucidate reaction mechanisms that remain elusive to experimental observation. A detailed discussion of global models is provided in sub-section 2.1.

The second model employed is 1D reaction-transport simulation, a one-dimensional fluid flow model that solely considers the depth dimension of the solution. This model assumes that the solution moves into the reactor along with the occurrence of chemical processes between species. This assumption leads to more realistic calculations that align with actual experimental conditions. The key distinction

between 0D and 1D models lies in the assumption of solution homogeneity. While 0D models assume a homogeneous solution due to fast stirring, 1D models eliminate this assumption and perform reaction calculations at each depth point. Consequently, computations in 1D models are slower compared to 0D models. A detailed discussion of 1D models is provided in sub-section 2.2.

Both 0D and 1D models were employed in this study to investigate reaction mechanisms among species within a PBS-like solution, aiming to gain a comprehensive understanding beyond the reach of experimental observation. These models were selected due to their widespread use by other researchers and their proven accuracy. Both models were originally developed in our lab by Kazumasa Ikuse, and we modified them to suit our specific needs. The modifications involved adjusting the number of reactions considered, the number of species involved, and the code for post-processing computational results.

1.4 Motivation

Plasma-based medical therapies hold immense promise due to unique advantages over conventional treatment methods. These advantages include the absence of systemic drug administration, enabling targeted treatment of specific areas, unlike chemotherapy. Consequently, plasma therapy represents a promising frontier in medical advancements. Despite extensive experimental investigations, the underlying mechanisms of plasma irradiation remain elusive. A thorough understanding of the interactions between plasma irradiation and cells, along with their surrounding fluids, is crucial for optimizing plasma therapy applications in medicine.

Recognizing the critical importance of elucidating the fundamental mechanisms governing plasma interactions with cells and their surrounding fluids, we are driven to investigate the intricate interplay between plasma and phosphate buffered saline (PBS) solution. PBS serves as a surrogate for biological fluids due to its compositional similarity to human body fluids. This research aims to unravel the reaction mechanisms between plasma and PBS, leading to the identification of the reaction pathway within PBS. Determining the reaction sites is paramount, as it will reveal the chemical species that can penetrate the solution and interact with cells. Furthermore, plasma is a charged gas emitted in a pulsed mode, necessitating a

thorough understanding of the influence of charge on PBS and the effects of pulsed irradiation. Ultimately, this comprehensive investigation will unravel the holistic nature of plasma-PBS interactions.

PBS is a solution composed of 137 mM NaCl, 2.7 mM KCl, 10 mM Na_2HPO_4, and 1.8 mM KH_2PO_4. Among these components, NaCl is present at the highest concentration. It is well-established that plasma irradiation typically generates reactive oxygen and nitrogen species (RONS), with hydrogen peroxide (H_2O_2) being one of the dominant species.

H2O2 plays a crucial role in various biomedical applications, including disinfection, sterilization, therapeutic treatments, and pollutant degradation. It is also known that H_2O_2 can react with chlorine solutions, commonly found in several liquids, including PBS. When chlorine encounters H_2O_2, it will inevitably react, yielding byproduct species.

Understanding the decomposition process involving chlorine and H_2O_2 is paramount in the field of plasma-liquid interaction, as H_2O_2 generated by plasma will invariably encounter chlorine solutions in numerous applications. Comprehending how H_2O_2 interacts with ClO^-/HOCl is critical due to:

1. Synergy and Antagonism: The reactions between H_2O_2 and chlorine species can produce other highly reactive free radicals (e.g., $Cl^\bullet$, $O_2{}^{\bullet-}$) that enhance disinfection efficiency or pollutant degradation. However, under certain conditions, these reactions can also serve as undesirable decomposition pathways for H_2O_2 or ClO^-/HOCl, thereby reducing the overall effectiveness of the plasma-liquid system.

2. Process Optimization: To optimize the performance of plasma-liquid systems (e.g., for bacterial inactivation, pollutant degradation, or plant growth stimulation), it is essential to control the type and concentration of reactive species generated. Understanding the kinetics of H_2O_2 decomposition by chlorine species enables researchers to refine plasma parameters and liquid composition.

To facilitate a well-structured and efficient investigation, we have divided the research into three distinct phases:

1. Global Model Investigation: This phase focuses on elucidating the reaction mechanisms within the PBS solution using a global model. The primary objective is to identify the reaction pathway in the PBS-like solution. The global model enables extended time-scale investigations.(Chapter 3)

2. Reaction Site Investigation: This phase employs 1D reaction-transport simulation to pinpoint the locations of chemical reactions. The outcome is to determine the depth at which chemical reactions occur, thus revealing the reaction sites. (Chapter 4)

3. Pulsed Injection and Charged Species Investigation: This phase utilizes pulsed injection to investigate the behavior of charged species within the PBS-like solution. The goal is to understand the effects of charged species upon entering the solution and to determine whether pulsed injection has a distinct impact compared to continuous injection.(Chapter 5)

Chapter 2

The description on how mathematical model work to simulate plasma condition in the real life

In this study, a comprehensive investigation of plasma interaction with PBS was conducted utilizing two models: a Global model and a 1D reaction-transport simulation. These two models are complementary, as each possesses distinct advantages and limitations.

Within the Global model framework, the primary benefits include rapid and computationally efficient simulations. Furthermore, its implementation requires only a single processor. The Global model is particularly well-suited for calculations necessitating the simulation of prolonged plasma-liquid interaction durations.

A key assumption inherent in the Global model is the rapid mixing of the solution, leading to the consideration of uniform solution conditions. Consequently, the Global model does not incorporate distinct regions representing the solution surface or depth. This is predicated on the assumption of homogeneous solution conditions irrespective of spatial location. This very assumption constitutes a limitation of the Global model, thereby precluding detailed analysis of solution conditions at the surface or within the bulk liquid.

To address the limitations inherent in the Global model, we also employed a 1D reaction-transport simulation. The advantage of this model lies in its ability to perform detailed calculations based on the solution depth profile. We partitioned the solution depth into two distinct regions: the reaction boundary layer (RBL) and the solution bulk. The RBL constitutes the layer proximate to the solution surface, directly interfacing with the gas phase, and typically exhibits a depth of less than 1 micrometer. Subsequently, the second region, the bulk of the solution, represents the solution depth accessible only to dominant chemical species.

The 1D reaction-transport simulation also presents certain limitations, notably the significantly extended simulation time. This is attributed to the very fine computational grid step employed, which necessitates more complex computations by the computer. In these calculations, we utilized parallel computing with 40 processors. Nonetheless, the time required to complete complex cases remained substantial. To illustrate, simulating a duration of 0.1 seconds necessitated a computational time frame of 4 to 6 months.

2.1 Global Model (zero dimensional reaction simulation)

Liquid model

The solution model employed in this study resembles PBS (Phosphate-Buffered Saline), a commonly used buffer solution. It is numerically configured to maintain a constant pH of 7, analogous to the buffering mechanism of PBS. This constant pH is achieved by numerically regulating the concentrations of H^+ and OH^-. When the supply of H^+ increases, the numerical supply of OH^- is also augmented, ensuring a consistent pH of 7. The modeled PBS solution volume is 3 ml, contained within a container with a surface area of 10 cm^2 (a petri dish with a diameter of 3.6 cm).

For the plasma jet simulation, we assume a highly tapered jet with an area of 0.1 cm^2 (a diameter of 3.6 mm in contact with the solution). During plasma irradiation, the solution is assumed to be in thermal equilibrium with the ambient air (80% N_2 and 20% O_2) at a pressure of 1 atm (101,325 Pa) and room temperature

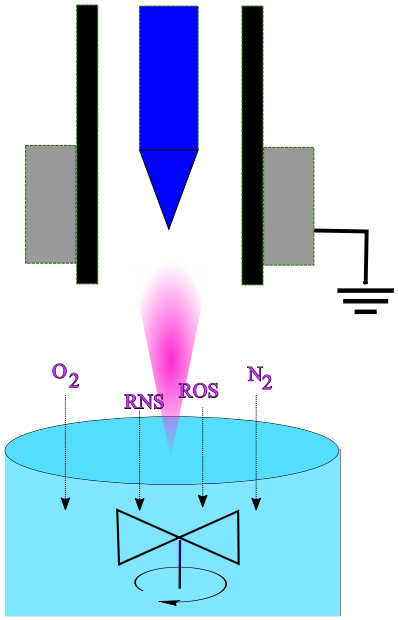

Figure 2.1: Conceptual diagram of global model

(298.15 K). The initial concentrations of N_2 and O_2 in the solution are assumed to be 4.76×10^4 mol l^{-1} and 2.72×10^4 mol l^{-1}, respectively. NaCl is assumed to be fully ionized into Na^+ and Cl^- with a concentration of $[Na^+] = [Cl^-] = 0.137$ mol l^{-1}.

Figure 2.1 presents a conceptual diagram illustrating the overall model calculation process. The plasma irradiation is depicted interacting with the surrounding air. Charged species collide with air particles, generating various Reactive Oxygen Nitrogen Species (RONS). These RONS subsequently diffuse into the PBS solution and are assumed to mix rapidly, resulting in uniform concentrations of each species throughout the solution. Based on this assumption, the concentration changes of each species within the solution can be evaluated using a 0D model.

Semi-implicit Euler method

When the independent variable associated with the change of dependent variables in two or more first-order differential equations has vastly different scales, the differential equations can become "stiff." While a precise definition of stiff differential equations remains elusive, it is generally understood that instabilities, such

as solution divergence or the emergence of solutions significantly different from the true solution, can arise in numerical methods depending on the time step width and the computational method.

Numerical methods are a class of computational techniques employed to approximate solutions of differential equations. The accuracy and stability of numerical calculations vary depending on the specific method utilized. In general, larger time steps in simulations lead to shorter computation times but reduced accuracy. Conversely, excessively small time steps increase computation time while potentially diminishing accuracy due to the accumulation of numerical errors. Therefore, selecting an appropriate time step is crucial for both the numerical method and the computational model.

In this research, as in the numerical analysis of chemical reaction systems, chemical reaction equations with vastly different rate constant scales are involved. Consequently, selecting a computational method that accounts for stiff differential equations is essential. We employs the semi-implicit Euler method, renowned for its ability to construct relatively simple algorithms with superior accuracy and stability. The semi-implicit Euler method is recognized as an effective tool for solving the stiff differential equations.

Implementation of the Semi-implicit Euler Method for Chemical Reactions

The semi-implicit Euler method is a numerical technique employed to solve differential equations, particularly those arising from chemical reaction systems. Here's a step-by-step implementation of this method in the context of chemical reactions:

1. Define Chemical Species as Elements Treat the concentration of each chemical species involved in the reaction as an element. This allows for a systematic representation of the system.

2. Formulate Reaction Rate Equations Based on the reaction equations, derive the reaction rate equations for each element. These equations represent the change in concentration of each species over time. Example: Consider the reaction rate equation for the concentration of $[e^-]$ from e^-, as expressed in

Equation 2.1.

$$f_1 = \frac{d[e^-_{aq}]}{dt} = k_1[e^-_{aq}][e^-_{aq}] + k_2[e^-_{aq}][H^+_{aq}] + \cdots \tag{2.1}$$

Here K_1 and K_2 represent the rate constants for the reaction equations presented in Equations (R_o02) and (R_o03) of Appendix A Table A.1. By assigning initial values to each element in the differential equations derived from the reaction rate equations and employing the numerical method to perform the calculations, the temporal changes for each element can be obtained.

$$y_1^{t+\Delta t} = y_1^t + \Delta \cdot f_1(y_1^t, y_2^t, \cdots, y_n^t) \tag{2.2}$$

The explicit Euler method, a numerical technique for solving single-variable differential equations, can be extended to handle multivariable systems. The equation for element y_1 can be expressed as Equation 2.2. In this equation,y_1^t, y_2^t, $\cdots$, y_n^t represent the concentrations of the respective chemical species at time t, and Δt corresponds to the magnitude of the time step.

3. Constructs the series equation.

   The equation for the implicit Euler method (equation 2.2) can be expanded into a series up to the nth order for f_1, resulting in equation below

$$\begin{aligned} y_1^{t+\Delta t} &= y_1^t + \Delta \cdot f_1(y_1^t, y_2^t, \cdots, y_n^t) \\ &= y_1^t + \Delta \cdot f_1\left(y_1^{t+\Delta t} - y_1^t + y_1^t, y_2^{t+\Delta t} - y_2^t + y_2^t, \cdots, y_n^{t+\Delta t} - y_n^t + y_n^t\right) \\ &\approx y_1^t + \Delta t \left[f_1(y_1^t, y_2^t, \cdots, y_n^t) + \frac{\partial f_1}{\partial y_1} \cdot (y_1^{t+\Delta t} - y_1^t) \right. \\ &\quad \left. + \frac{\partial f_2}{\partial y_2} \cdot (y_2^{t+\Delta t} - y_2^t) + \cdots + \frac{\partial f_1}{\partial y_n} \cdot (y_n^{t+\Delta t} - y_n^t) \right] \end{aligned} \tag{2.3}$$

   Averaging Equations 2.2 and 2.3 results in Equation below

$$\begin{aligned} y_1^{t+\Delta t} &= y_1^t + \frac{\Delta t}{2} \left[2f_i\left(y_1^t, y_2^t, \cdots, y_n^t\right) + \frac{\partial f_i}{\partial y_1} \cdot \left(y_1^{t+\Delta t} - y_1^t\right) \right. \\ &\quad \left. + \frac{\partial f_i}{\partial y_2} \cdot \left(y_2^{t+\Delta t} - y_2^t\right) + \cdots + \frac{\partial f_i}{\partial y_n} \cdot \left(y_n^{t+\Delta t} - y_n^t\right) \right] \end{aligned} \tag{2.4}$$

Putting the $t+\Delta t$ term on the left side and the t term on the right side from equation 2.4, we get the equation below

$$\begin{aligned}\therefore\quad & \left(1-\frac{\Delta t}{2}\cdot\frac{\partial f_1}{\partial y_1}\right)y_1^{t+\Delta t}-\frac{\Delta t}{2}\cdot\frac{\partial f_1}{\partial y_2}\cdot y_2^{t+\Delta t}-\cdots-\frac{\Delta t}{2}\cdot\frac{\partial f_1}{\partial y_n}\cdot y_n^{t+\Delta t}\\ = \quad & \left(1-\frac{\Delta t}{2}\cdot\frac{\partial f_1}{\partial y_1}\right)y_1^{t}-\frac{\Delta t}{2}\cdot\frac{\partial f_1}{\partial y_2}\cdot y_2^{t+\Delta t}-\cdots-\frac{\Delta t}{2}\cdot\frac{\partial f_1}{\partial y_n}\cdot y_n^{t}\\ & +\Delta t\cdot f_i(y_1^t,y_2^t,\cdots,y_n^t)\end{aligned}\tag{2.5}$$

4. Constructing matrix

Resolving equations using numerical methods is often facilitated by transforming them into matrix-vector form. Equation 2.5 is transformed into a matrix form separated by vectors $y_1^{t+\Delta t}, y_2^{t+\Delta t}, ..., y_n^{t+\Delta t}$. The resulting matrix transformation is presented in the following equation.

$$\begin{bmatrix}\left(1-\frac{\Delta t}{2}\cdot\frac{\partial f_1}{\partial y_1}\right) & -\frac{\Delta t}{2}\cdot\frac{\partial f_1}{\partial y_2} & \cdots & -\frac{\Delta t}{2}\cdot\frac{\partial f_1}{\partial y_n}\\ -\frac{\Delta t}{2}\cdot\frac{\partial f_2}{\partial y_1} & \left(1-\frac{\Delta t}{2}\cdot\frac{\partial f_2}{\partial y_2}\right) & \cdots & -\frac{\Delta t}{2}\cdot\frac{\partial f_2}{\partial y_n}\\ \vdots & \vdots & \ddots & \vdots\\ -\frac{\Delta t}{2}\cdot\frac{\partial f_n}{\partial y_1} & -\frac{\Delta t}{2}\cdot\frac{\partial f_2}{\partial y_2} & \cdots & \left(1-\frac{\Delta t}{2}\cdot\frac{\partial f_n}{\partial y_n}\right)\end{bmatrix}\begin{bmatrix}y_1^{t+\Delta t}\\ y_2^{t+\Delta t}\\ \vdots\\ y_n^{t+\Delta t}\end{bmatrix}=$$
$$\begin{bmatrix}\left(1-\frac{\Delta t}{2}\cdot\frac{\partial f_1}{\partial y_1}\right) & -\frac{\Delta t}{2}\cdot\frac{\partial f_1}{\partial y_2} & \cdots & -\frac{\Delta t}{2}\cdot\frac{\partial f_1}{\partial y_n}\\ -\frac{\Delta t}{2}\cdot\frac{\partial f_2}{\partial y_1} & \left(1-\frac{\Delta t}{2}\cdot\frac{\partial f_2}{\partial y_2}\right) & \cdots & -\frac{\Delta t}{2}\cdot\frac{\partial f_2}{\partial y_n}\\ \vdots & \vdots & \ddots & \vdots\\ -\frac{\Delta t}{2}\cdot\frac{\partial f_n}{\partial y_1} & -\frac{\Delta t}{2}\cdot\frac{\partial f_2}{\partial y_2} & \cdots & \left(1-\frac{\Delta t}{2}\cdot\frac{\partial f_n}{\partial y_n}\right)\end{bmatrix}\begin{bmatrix}y_1^{t}\\ y_2^{t}\\ \vdots\\ y_n^{t}\end{bmatrix}+\Delta t\begin{bmatrix}f_1^t\\ f_2^t\\ \vdots\\ f_n^t\end{bmatrix}\tag{2.6}$$

If A is a matrix $n \times n$

$$A=\begin{bmatrix}\left(1-\frac{\Delta t}{2}\cdot\frac{\partial f_1}{\partial y_1}\right) & -\frac{\Delta t}{2}\cdot\frac{\partial f_1}{\partial y_2} & \cdots & -\frac{\Delta t}{2}\cdot\frac{\partial f_1}{\partial y_n}\\ -\frac{\Delta t}{2}\cdot\frac{\partial f_2}{\partial y_1} & \left(1-\frac{\Delta t}{2}\cdot\frac{\partial f_2}{\partial y_2}\right) & \cdots & -\frac{\Delta t}{2}\cdot\frac{\partial f_2}{\partial y_n}\\ \vdots & \vdots & \ddots & \vdots\\ -\frac{\Delta t}{2}\cdot\frac{\partial f_n}{\partial y_1} & -\frac{\Delta t}{2}\cdot\frac{\partial f_2}{\partial y_2} & \cdots & \left(1-\frac{\Delta t}{2}\cdot\frac{\partial f_n}{\partial y_n}\right)\end{bmatrix},$$

$F(t)$ is a vector

$$F(t) = \begin{bmatrix} f_1(y_1^t, y_2^t, \cdots, y_n^t) \\ f_2(y_1^t, y_2^t, \cdots, y_n^t) \\ \vdots \\ f_n(y_1^t, y_2^t, \cdots, y_n^t) \end{bmatrix},$$

$y(t + \Delta t)$ and $y(t)$ is a vector

$$y(t + \Delta t) = \begin{bmatrix} y_1^{t+\Delta t} \\ y_2^{t+\Delta t} \\ \vdots \\ y_n^{t+\Delta t} \end{bmatrix}, y(t) = \begin{bmatrix} y_1^t \\ y_2^t \\ \vdots \\ y_n^t \end{bmatrix},$$

we can write equation 2.6 in more simple equation form

$$\begin{aligned} Ay(t + \Delta t) &= Ay(t) + \Delta t \cdot F(t) \\ \therefore y(t + \Delta t) &= y(t) + \Delta t \cdot A^{-1} F(t) \end{aligned} \tag{2.7}$$

After we get equation 2.7, then we can implement it into the numerical model to calculate concentrations of each species inside the solution.

Implementation to numerical model

The 13 chemical species from the gas dissolve to the 3 ml NaCl solution with surface area 10 cm^2. The influx of the gaseous species to NaCl solution given by the boundary condition in the gas and NaCl solution. The gas influx is assumed to penetrate the solution with thermal velocities, and the outward flux of reactive species from the solution to the gas phase is determined using Henry's law.

The initial concentration from the gas influx is taken from the calculation data [240]. The initial NaCl solution is set using the buffer, so the pH in the solution is assumed in constant condition (pH=7). This assumption is to achieve the experimental using phosphate buffer saline (PBS) solution. The temperature we used in this simulation is room temperature (298.15 K).

The concentration n_i of chemical species i in the solution is determined from the governing equation [97];

$$\frac{\partial n_i}{\partial t} = \hat{\Re}_i + \frac{1}{V} \cdot v_{th} \left(S_{\text{in}} \cdot n_i^{\text{gas}} - S_{\text{out}} \cdot \frac{n_i}{K_i^{\text{H}} \cdot R \cdot T_{\text{g}}} \right)$$

with

$$v_{\rm th} = \frac{1}{2}\sqrt{\frac{2k_{\rm B}T_{\rm g}}{\pi m_i}}.$$

Here $n_i(t)$ is the concentration of the i-th chemical species in the solution at time t, V denotes the volume of the liquid, $S_{\rm in}$ is the area of plasma exposure on the water (i.e., solution) surface, $S_{\rm out}$ is the area of the water surface, $K_i^{\rm H}$ is Henry's constant for the species i, R is the gas constant, $T_{\rm g}$ is the gas temperature, $k_{\rm B}$ is the Boltzmann constant, and m_i is the mass of the species i. The thermal velocity $v_{\rm th}$ is defined in such a way that $\Gamma_i = v_{\rm th} n_i^{\rm gas}$ represents the flux of the gas-phase species i entering the water surface under the assumption that the gas-phase species i forms a Maxwellian distribution with temperature $T_{\rm g}$.

The production/loss rate $\hat{\Re}_i$ of species i by the liquid-phase chemical reactions is given by

$$\hat{\Re}_i = -\sum_{i\in{\rm A,B,C,\cdots}}(abc\cdots)k^{\rm PQR\cdots}_{\rm ABC\cdots}\,[{\rm A}]^a\,[{\rm B}]^b\,[{\rm C}]^c\cdots \quad +\sum_{i\in{\rm P,Q,R,\cdots}}(abc\cdots)k^{\rm PQR\cdots}_{\rm ABC\cdots}\,[{\rm A}]^a\,[{\rm B}]^b\,[{\rm C}]^c\cdots \tag{2.8}$$

for the chemical reaction

$$a{\rm A} + b{\rm B} + c{\rm C} + \cdots \quad \xrightarrow{k^{\rm PQR\cdots}_{\rm ABC\cdots}} p{\rm P} + q{\rm Q} + r{\rm R} + \cdots$$

where the reaction among chemical species A, B, C, ... generate chemical species P, Q, R, ... with rate constant $k^{\rm PQR\cdots}_{\rm ABC\cdots}$. In Eq. (2.8), [A] denotes the concentration of species A. The summation $\sum_{i\in{\rm A,B,C,\cdots}}$ is taken over all such reactions with one (or some) of A, B, C, ... species being the i-th species. Similarly, the summation $\sum_{i\in{\rm P,Q,R,\cdots}}$ is taken over all such reactions with one (or some) of P, Q, R, ... species being the i-th species.

2.2 1D Reactions-transport simulation (1 dimensional calculation)

Liquid model

We use a 1-dimensional reaction-transport simulation to simulate phenomena of plasma irradiated PBS-like solution to achieve that motivation. The illustration

of the system is shown in figure 2.2. Plasma jet produces various chemical species when discharge happens (illustrated in pink).[240] Each species penetrate the PBS-like solution through boundary condition of gas and solution (illustrated as dotted line arrow). The chemical reaction proceeds in parallel with the diffusion from the surface into the solution (line arrow). In the layer close to the surface, various chemical reactions occur. This reaction produces stable species and decomposes unstable species. The stable species (e.g., H_2O_2, NO_3^-, and NO_2^-) can penetrate the bulk liquid by diffusion. Otherwise, reactive species (e.g., O, O_3, and O_3^-) only appear in-depth near the surface or less than ten micrometers, which we call the area as a reaction boundary layer (RBL).

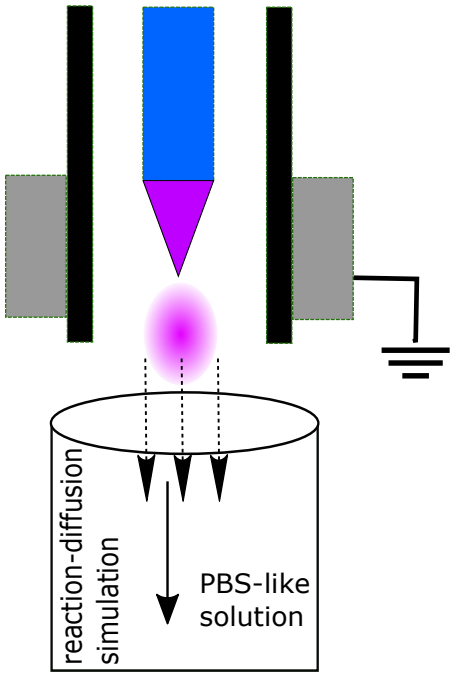

Figure 2.2: Schematic model of the PBS-like solution irradiated by Atmospheric Pressure Plasma (APP) jet. Gases produced by plasma (illustrated in pink) penetrated the solution through boundary between gas and solution. After penetration, chemical species from the gas react with chemical species in the solution. The reaction occurs in the reaction boundary layer (RBL) to form the dominant species and then diffuses to the bulk of the solution. Calculation of changing the concentration of every chemical species and the diffusion calculated using the reaction-diffusion (transport) simulation.

A 1-dimensional reaction-diffusion simulation governs the calculation of the concentration profile of each species and the transport process inside the PBS-like solution. The initial condition of the solution is set up close to phosphate-buffered saline; we call it phosphate-buffered saline-like (PBS-like) solution. The initial condition of the liquid using Na^+ and Cl^- at 0.137 mol l^{-1} with constant pH of 7. Oxygen and Nitrogen are dissolved in equilibrium with air at 1 atm to approach the actual condition. Eighty-two chemical species and 210 chemical reactions are applied in the calculation model. The models are assumed to be room conditions with a temperature of 298K and pressure of 1 atm.

Mathematical models

The equation governing the calculation of species concentration changes over time ($\frac{\partial n_i^{liq}}{\partial t}$)is given by the Equation below

$$\frac{\partial n_i^{liq}}{\partial t} = \hat{\Re}_i - \nabla \cdot \left(n_i^{liq} \boldsymbol{v}_i \right)$$

with n_i^{liq}, v_i are concentration of species i, liquid velocity, and $\hat{\Re}_i$ is reaction rate following formulation bellow

$$\hat{\Re}_i = \sum_{i \in \mathrm{A,B,C,\cdots}} k_{\mathrm{ABC\cdots}}^{\mathrm{abc\cdots}} \left[\mathrm{A}\right] \left[\mathrm{B}\right] \left[\mathrm{C}\right] \cdots \quad - \sum_{i \in \mathrm{a,b,c,\cdots}} k_{\mathrm{ABC\cdots}}^{\mathrm{abc\cdots}} \left[\mathrm{A}\right] \left[\mathrm{B}\right] \left[\mathrm{C}\right] \cdots$$

The calculation of mass and momentum conservation for species entering the fluid is obtained using the Equation below.

$$m_i n_i^{liq} \frac{d\boldsymbol{v_i}}{dt} = \underbrace{-k_B T_w \nabla n_i^{liq}}_{\text{temp}} + \underbrace{q_i n_i^{liq} \boldsymbol{E}}_{\text{charge}} - \underbrace{\nu_i m_i n_i^{liq} \left(\boldsymbol{v_i} - \boldsymbol{v_c} \right)}_{\text{mass and momentum}} \tag{2.9}$$

The right-hand side of the equation is decomposed into three distinct groups. The species concentration is influenced by water temperature (T_w) and the Boltzmann constant(k_B), the impact of charge (q_i) and the electric field ($\boldsymbol{E}$), and momentum calculations. $\boldsymbol{v_i}, \boldsymbol{v_c}$ and ν_i represent fluid velocity, the convective flow velocity of water, and collision frequency of species i with water molecules, respectively.

The electric field is calculated using the following Poisson's equation 2.10

$$\nabla \cdot E = \frac{\rho}{\epsilon_w} \tag{2.10}$$

with ρ is the total charge density and ϵ_w is permittivity of pure water.

To simplify Equation 2.9, manipulations are performed until the left-hand side represents the solution velocity, resulting in the following Equation

$$\boldsymbol{v_i} = \boldsymbol{v_c} + \frac{q_i n_i^{liq} \boldsymbol{E}}{\nu_i m_i n_i^{liq}} - \frac{k_B T_w \nabla n_i^{liq}}{\nu_i m_i n_i^{liq}}. \tag{2.11}$$

If we consider μ_i and D_i as

$$\mu_i = \frac{q_i}{\nu_i m_i}$$

and

$$D_i = \frac{k_B T_w}{\nu_i m_i},$$

Equation 2.11 become

$$\boldsymbol{v_i} = \boldsymbol{v_c} + \mu_i \boldsymbol{E} - \frac{D_i}{n_i^{liq}} \nabla n_i^{liq}$$

where μ_i and D_i denote the mobility and diffusion coefficient.

The Nernst-Einstein equation, to calculate the ionic diffusion coefficients from experimental determinations of conductivity,

$$\mu_i = \frac{q_i D_i}{k_B T_w} \tag{2.12}$$

is satisfied. The divergence of water flow velocity is set to zero with the assumption that water is incompressible i.e.

$$\nabla \cdot \boldsymbol{v_c} = 0. \tag{2.13}$$

The governing equation for our simulation model is obtained by substituting Eq. 2.11 for $\boldsymbol{v_1}$ into Eq. 2.2, considering Eq. 2.13, resulting in Equation below

$$\frac{\partial n_i^{liq}}{\partial t} = \hat{\Re}_i - \boldsymbol{v_c} \cdot \nabla n_i^{liq} - \mu_i \nabla \cdot \left(n_i^{liq} \boldsymbol{E} \right) + D_i \Delta n_i^{liq} \tag{2.14}$$

The generated gas plasma species will encounter the liquid surface. Based on their charge, these species are categorized into two groups: charge-neutral species and charged species. For charge-neutral species, typical room-temperature pressure and temperature are assumed, resulting in the adherence of charge-neutral gas-phase species to the liquid surface. Upon surface attachment, the possibility

of re-adsorption exists, allowing some species to penetrate the liquid while others may re-gasify or desorb. This behavior follows Henry's constant of each species, which governs thermal equilibrium. To model this process, boundary conditions such as Equation 2.15 are required.

$$\boldsymbol{v}_i^{th}\left(n_i^{gas}-\frac{n_i^{liq}}{k_i^H R T_g}\right)\cdot\boldsymbol{n}=-D_i\boldsymbol{n}\cdot\nabla n_i^{liq} \tag{2.15}$$

The detailed calculations for the solution surface and depth are presented in the following equations:

$$\boldsymbol{v}_i^{th}\left(n_i^{gas}-\frac{n_i}{k_i^H R T_g}\right)=-D_i\left.\frac{\delta n_i}{\delta x}\right|_{x=0} \tag{2.16a}$$

$$0=-D_i\left.\frac{\delta n_i}{\delta x}\right|_{x=L} \tag{2.16b}$$

Boundary condition for charged-neutral species 2.16. in the surface is 2.16a, In the bulk of liquid equation is 2.16b. Where $\boldsymbol{v}_i^{th}$, n_i^{gas}, and k_i^H represent the thermal velocity, concentration in the gas phase, and Henry's constant of species i. The constants R and T_g denote the gas constant and temperature and $\boldsymbol{n}$ is the unit vector normal to the boundary. Here we assume $T_g = T_w$.

Note that the dissolution (or solvation) rate of the gaseous species i is provided by Eq. 2.15. The dissolving rate drops to zero as the liquid phase concentration n_i^{liq} rises and approaches the solubility limit. The greatest concentration of a species soluble in water at the point of thermal equilibrium between the water and the gas at its partial pressure is known as the solubility limit. Expression for solubility limit shown below

$$n_i^{liq}=k_i^H R T_g n_i^{gas} \tag{2.17}$$

Equation 2.17 shows that the solubility of a specific species is low if its Henry's constant is low.

We can determine the incident fluxes of charged gas-phase species, such electrons and ions, by measuring their electric currents. We formulate the boundary conditions for charged species corresponding to Eq. 2.15 as follows, assuming that no charged species desorbs from the surface thermally.

$$\frac{\boldsymbol{j}_i\cdot n}{q_i}=\left(-D_i\nabla n_i^{liq}+\mu_i n_i^{liq}\boldsymbol{E}\right)\cdot\boldsymbol{n} \tag{2.18}$$

where $\boldsymbol{j}_i$ represents the current density carried by charged species i and $\boldsymbol{n}$ is the unit vector normal to the boundary. Boundary condition for charged species in the surface is 2.19a. in the bulk of liquid is 2.19b

$$\frac{\boldsymbol{j}_i \cdot n}{q_i} = \left(-D_i \frac{\delta n_i}{\delta x} + \mu_i n_i E \right) \Big|_{x=0} \tag{2.19a}$$

$$0 = -D_i \left. \frac{\delta n_i}{\delta x} \right|_{x=L} \tag{2.19b}$$

In this work, we solve the aforementioned equations as a one-dimensional model moving from the liquid's surface to its bottom. In this case, we take the x coordinate in the direction of depth, where the water surface is indicated by the origin $x = 0$. Equations 2.15 and 2.18 provide the boundary conditions at $x = 0$. Given that the water container's bottom depth in our system is L and that there is no current flowing through it, the boundary condition at the bottom of the container, $x = L$, can be expressed as follows.

$$0 = \left(-D_i \nabla n_i^{liq} + \mu_i n_i^{liq} \boldsymbol{E} \right) \Big|_{x=L} \tag{2.20}$$

for both charged and charge-neutral species, or written in Eq. 2.16b and 2.19b.

Our numerical simulation employs a finite-difference approach to discretize the governing equation (Eq. 2.14) in space (along the x-axis). Non-uniform grids are used to capture the sharp variations in concentration gradients. The Scharfetter-Gummel (SG) scheme is implemented for solving the discretized equation (reference [204]). Due to the potential stiffness of the rate equations, a second-order semi-implicit scheme is utilized for time advancement.

This study compiles the diffusion coefficients and Henry's constants for the utilized chemical species in Tables B.12. For certain species, diffusion coefficients were not readily available in the literature. In such cases, a tentative value of $2.0x10^{-}9$ m^2/s was assigned. This value is considered a reasonable approximation for most species due to the generally limited variation in diffusion coefficients within liquids, with the exception of the hydrogen ion (H^+) or hydronium ion (H_3O^+). These ions exhibit significantly higher diffusion coefficients.

Similarly, for species lacking reported Henry's constants in the literature, we assume they are non-desorbable from the surface. This implies an infinitely large Henry's constant for these species.

Table A.1 summarizes the chemical reactions employed in this study. These reactions are presented in the general form:

$$aA + bB + cC \rightarrow p_1P_1 + p_2P_2 + \cdots \tag{2.21}$$

where A, B, and C represent the chemical formulas of the reactants, and P_1, P_2, etc. represent the products. The stoichiometric coefficients a, b, c, p_1, p_2, etc. (all non-zero) are positive integers with no common factors greater than 1. The sum $o = a + b + c$ defines the reaction order.

For our simulation, the rate of reaction (2.21) is expressed as the rate of change of reactant A:

$$\nu = -\frac{1}{a}\frac{d}{dt}[A] \tag{2.22}$$

This rate is further assumed to follow the power law rate expression:

$$\nu = k[A]^a[B]^b[C]^c \tag{2.23}$$

The symbol $[A]$ denotes the concentration of species A. Concentration is typically expressed in units of molarity (M), which represents moles of solute per liter of solution (mol l^{-1}). The rate constant, denoted by k, is characteristic of a specific reaction. Units for the rate constant depend on the reaction order (o). Generally, the units are expressed as $M^{1-o}s^{-1}$, where o represents the overall reaction order. The use of this unit is displayed in Table A.1. The term $\hat{\Re}_i$ signifies the net rate of change in the number of moles of species i (n_i^{liq}) within the liquid phase due to all the considered chemical reactions.

Within this simulation, the calculation of the reaction term ($\hat{\Re}_i$) leverages Message Passing Interface (MPI) to enable parallel processing across discretized mesh points. This approach allows the simulation to execute computations representing many seconds of physical time within a practical time-frame.

Chapter 3

Zero dimensional calculation of Plasma irradiated PBS-like solution

3.1 Introduction

Low-temperature atmospheric-pressure plasmas (APPs) have been widely used for various applications,[105, 249, 235, 214, 176, 130, 206, 87, 41, 30, 4, 239, 3] including surface treatment of materials,[111, 110, 234, 221, 171, 199, 12, 13, 193, 210, 165, 228, 63, 129] gas and liquid treatment,[118, 150, 218, 240, 164, 20, 109, 211, 37, 250] nano-particle synthesis,[68, 195, 67, 106, 227, 122, 120] sterilization, wound healing and other medical applications.[131, 213, 96, 248, 219, 149, 56, 65, 134, 160, 18, 162, 161, 193, 17, 76, 225], and plant treatment and other agricultural applications.[5, 53, 100, 189, 29, 16, 124, 191, 187] For many such applications, plasma-liquid interactions play important roles in generating relevant chemically reactive species.[113, 14, 216, 177, 217, 215, 31]

Typical low-temperature APPs are operated as pulsed discharges to avoid the heating of the ambient gas. Their ionization rates are typically low but the high collisionality between charged species, especially electrons, and ambient gas molecules leads to the generation of a large amount of highly reactive species. APPs generated in humid air can be efficient sources of reactive oxygen species (ROS) and

reactive nitrogen species (RNS). It has been known that water vapor mixed with an APP generates hydrogen peroxide H_2O_2. When liquid water is exposed to APPs, water vapor interacts with the plasma and generates gaseous H_2O_2, which can then dissolve into the liquid water. Some ROS generated in the gas phase, such as the hydroxyl radical OH, can also dissolve directly into water and form H_2O_2 in the liquid phase. Typically H_2O_2 is one of the most dominant species found in liquid water exposed to APPs.[151]

It is known that, if a saline solution is exposed to an APP, hypochlorous acid HOCl is generated in the solution. HOCl is known to have bactericidal effects.[6, 66] A recent study by Wende *et al.* [240] has found that, if a phosphate-buffered saline (PBS) solution is exposed to APPs, the amount of H_2O_2 formed in the solution can be reduced especially when the amount of admixed oxygen gas O_2 is high for plasma generation. Based on their experimental observations, they have concluded that hypochlorite anion ClO^- formed in the plasma-exposed solution react with H_2O_2 and generate water H_2O and molecular oxygen O_2.

The goal of this study is to confirm the reaction mechanism for the H_2O_2 decomposition in plasma-exposed PBS solutions proposed by Wende *et al.*,[240] using self-consistent chemical reaction simulations based on known liquid-phase chemical reactions. A set of chemical reactions is nonlinear and highly complex in the sense that several competing chemical reactions can take place simultaneously. An experimentally observed reaction can be a combination of separate chemical reactions, involving various intermediates, rather than a single chemical reaction. Under the experimental conditions presented in Ref. [240], we examine all possible reactions among the 318 chemical reactions we employ for this study and extract the dominant reactions for the phenomena of interest. The obtained numerical simulation results are compared with experimental data presented in Ref. [240].

Numerical simulations of chemical reactions in APP-exposed solutions have been studied extensively with different degrees in spatial dimensions, temporal and spatial resolutions, and complexities of chemical reactions, depending on the research goals.[80, 224, 148, 142, 146, 97, 155, 98] The chemical species observed in plasma-exposed liquids are typically much different from gas-phase chemical species in the plasma but, of course, strongly depend on them. Gas-phase chemical reactions generally involve a far more variety of species and a much larger number

of chemical reactions.[101] Therefore a detailed numerical simulation of gas-phase chemical reactions in an APP remains as a challenging research subject.[125, 200, 144, 119, 166, 168] In this study, we use the global (i.e., zero-dimensional) version of the liquid-phase chemical-reaction code presented in Ref. [98] with a few additional liquid-phase chemical reactions.

The rest of this article is organized as follows: Sectoin 3.2 presents the assumptions used for the model systems, i.e., a PBS solution exposed to low-temperature APPs under different conditions, that are numerically simulated in this study. In Sec. 3.3, the global model of liquid-phase reactions used in this study is explained. Section 3.4 presents the simulation results and analyses to identify the dominant reactions that lead to the decomposition of H_2O_2. The simulation results are also compared with the corresponding experimental data. Finally, the conclusions of this study are presented in Sec. 3.5.

3.2 PBS solution exposed to plasmas

Chemical species in the gas phase

We consider chlorinated water exposed to APPs studied by Wende *et al.* in Ref. [240]. In their study, APPs were generated with an argon (Ar) gas and possible admixtures under four different conditions; argon only (whose conditions we denote by "Ar"), argon mixed with 0.27% of water vapor H_2O ("Ar/H_2O"), argon mixed with 1% of air ("Ar/Air"), and argon mixed with 1% of O_2 ("Ar/O_2"). The densities of various gaseous species generated in those plasmas were evaluated with numerical simulations in Ref. [240]. From the simulation data, we extracted the densities of dominant chemically reactive species in the plasma at positions 0.8 cm, and 1 cm away from the nozzle exit of the plasma system, using WebPlot-Digitizer[196]. The extracted data for Ar, Ar/H_2O, Ar/air, and Ar/O_2 are summarized in Tables 3.1 and 3.2. The constituents and proportions of gas-phase species in these plasmas are shown in Fig. 3.1.

Table 3.1: Densities of gas-phase species generated under the conditions denoted by Ar, Ar/H_2O, Ar/Air, and Ar/O_2 at 0.8 cm from the nozzle exit, extracted from the numerical simulation data given in Ref. [240]. The discharge conditions are described in the main text.

Species	Gas-phase densities (cm^{-3})			
	Ar cm^{-3}	Ar/H_2O cm^{-3}	Ar/Air cm^{-3}	Ar/O_2 cm^{-3}
H	2.71×10^{11}	1.45×10^{11}	1.01×10^{12}	1.28×10^{11}
H_2O_2	1.36×10^{14}	3.83×10^{14}	9.34×10^{13}	6.48×10^{13}
HNO_2	1.63×10^{14}	1.48×10^{14}	3.34×10^{14}	7.09×10^{13}
HNO_3	1.86×10^{13}	2.08×10^{13}	3.69×10^{13}	1.30×10^{13}
HO_2	1.67×10^{13}	2.54×10^{13}	9.44×10^{12}	9.54×10^{12}
N	6.65×10^{13}	4.82×10^{13}	5.03×10^{13}	2.98×10^{13}
N_2O_5	8.00×10^{12}	2.74×10^{11}	4.09×10^{12}	6.23×10^{11}
NO	1.47×10^{14}	1.40×10^{14}	1.53×10^{14}	1.41×10^{14}
NO_2	2.81×10^{13}	2.94×10^{13}	3.31×10^{13}	2.49×10^{13}
O	1.63×10^{15}	6.17×10^{14}	1.17×10^{15}	1.50×10^{15}
O_3	9.67×10^{14}	3.13×10^{14}	1.31×10^{15}	2.63×10^{15}
OH	3.74×10^{13}	4.09×10^{13}	2.26×10^{13}	2.67×10^{13}

Table 3.2: Densities of gas-phase species generated under the conditions denoted by Ar, Ar/H_2O, Ar/Air, and Ar/O_2 at 1 cm from the nozzle exit, extracted from the numerical simulation data given in Ref. [240]. The discharge conditions are described in the main text.

Species	Gas-phase densities (cm^{-3})			
	Ar cm^{-3}	Ar/H_2O cm^{-3}	Ar/Air cm^{-3}	Ar/O_2 cm^{-3}
H	5.65×10^{11}	3.87×10^{11}	1.81×10^{11}	2.64×10^{11}
H_2O_2	1.49×10^{14}	3.72×10^{14}	9.44×10^{13}	6.85×10^{13}
HNO_2	1.81×10^{14}	1.47×10^{14}	3.10×10^{14}	7.99×10^{13}
HNO_3	2.37×10^{13}	2.44×10^{13}	3.91×10^{13}	1.57×10^{13}
HO_2	1.12×10^{13}	1.67×10^{13}	5.73×10^{12}	5.90×10^{12}
N	4.13×10^{13}	2.58×10^{13}	2.82×10^{13}	1.54×10^{13}
N_2O_5	1.44×10^{12}	4.10×10^{11}	4.92×10^{12}	9.36×10^{11}
NO	1.33×10^{14}	1.24×10^{14}	1.26×10^{14}	1.24×10^{14}
NO_2	2.93×10^{13}	2.79×10^{13}	3.22×10^{13}	2.63×10^{13}
O	8.70×10^{14}	4.25×10^{14}	5.11×10^{14}	6.58×10^{14}
O_3	2.23×10^{15}	7.93×10^{14}	2.24×10^{15}	3.55×10^{15}
OH	2.66×10^{13}	2.68×10^{13}	1.50×10^{13}	1.90×10^{13}

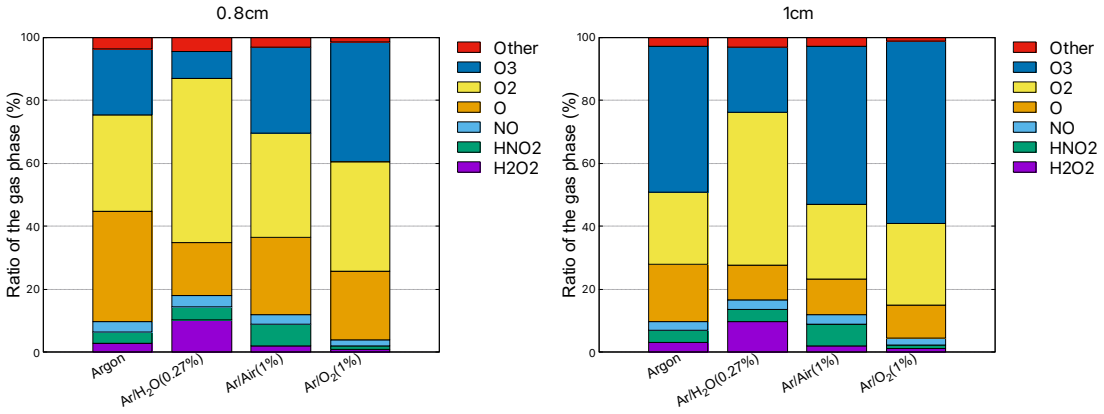

(a) (b)

Figure 3.1: The composition ratios of chemical species in the gas phase given in Tables 3.1, and 3.2 at distances of (a) 0.8 cm, and (b) 1 cm from the nozzle exit of the plasma source discussed in Ref. [240].

Chemical species in the aqueous solution

The experiments of Ref. [240] were performed with PBS. To simulate this liquid, we used a model aqueous solution of NaCl with a constant pH of 7, under the assumption that the phosphate buffer does not react with other species in the solution but contributes only to maintaining the concentrations of H^+ and OH^- at 10^{-7} mol l^{-1}. We call this model solution a "PBS-like solution" in this study. In this solution, NaCl was almost fully ionized and its initial concentration was 0.137 mol l^{-1}, i.e., $[Na^+] = [Cl^-] = 0.137$ mol l^{-1} with [A] representing the concentrations of species A in the solution. The gas-phase density of species A will be denoted with $[A]_{(g)}$. To emphasize a liquid-phase density of species A, we sometime denote it as $[A]_{(aq)}$ $(= [A])$.

The liquid-phase chemical reactions assumed in our study are the same as those given by Ikuse *et al.* in Ref. [98] as well as 3 reactions given in Table 3.3, where the sequential reaction numbers are consistent with those of the reaction table of Ref. [98]. For the convenience of the reader, the complete table for chemical reactions is given as Table S 1 in the supplementary material. In this study, we considered 60 liquid-phase chemical species (solutes), including solvated electrons, and 318 chemical reactions, including 77 ROS and water reactions, 77 reactive ni-

trogen species (RNS) reactions, 54 chlorine reactions, and 2 other reactions related to Na.

Table 3.3: The list of new chemical reactions introduced in this study. Other reactions used in this study are found in Ref. [98] or Table S1 of the supplementary material of this article. The units of the rate constant is L/mol/s.

No	Chemical Reactions	Rate cons. (l mol^{-1} s^{-1})	Ref
$R_{Cl}060$	$ClO + H_2O_2 \longrightarrow HOCl + HO_2$	3.0×10^8	[139]
$R_{Cl}061$	$ClO + HO_2 \longrightarrow HOCl + O_2$	4.2×10^9	[139]
$R_{Cl}062$	$HOCl + OH \longrightarrow ClO + H_2O$	1.4×10^8	[190]

3.3 Outline of numerical simulation

We now model experiments where APPs are exposed to a 3 mL PBS-like NaCl solution (discussed in the preceding subsection) placed in a container with a surface area of 10 cm^2 (such as a petri dish with a diameter of 3.6 cm). We consider a narrow plasma-jet like plasma source and the area of the solution surface exposed to the plasma and its gas-phase species is assumed to be limited to 0.1 cm^2 (such as a plasma generated in a cylindrical glass tube with a diameter of 3.6 mm.) Prior to the plasma exposure, the solution is in thermal equilibrium with ambient air (80% N_2 and 20% O_2) at 1 atm (i.e., 101,325 Pa) and room temperature (298.15 K), such that the the initial concentrations of N_2 and O_2 in the solution are $[N_2] = 4.76 \times 10^4$ mol l^{-1} and $[O_2] = 2.72 \times 10^4$ mol l^{-1}. Initially NaCl is assumed to be fully ionized with a concentration of 0.137 mol l^{-1}, i.e., $[Na^+] = [Cl^-] = 0.137$ mol l^{-1}. Its pH is maintained at 7 throughout the experiment, even after it is exposed to a plasma.

For the sake of simplicity, we only consider charge-neutral species (i.e., no ions or electrons) generate by the plasma as incident gas-phase species entering the solution surface. In typical APPs, the concentrations of charge-neutral species are far larger than those of charged species. Discussion on the effects of incident ions and electrons is deferred to future studies. All gas-phase charge-neutral species are assumed to be in thermal equilibrium at room temperature (298.15 K) in this study. As our interest is the experimental conditions of Ref. [240], we consider

the cases when the PBS-like solution is exposed to the plasma-generated charge-neutral species given in Tables 3.1, and 3.2. In addition to the gas-phase species listed in these Tables, the solution is also exposed to ambient air of 80% N_2 and 20% O_2 at 1 atm during the plasma exposure. The concentrations of the gas-phase species and ambient temperature are assumed to be constant in time. The outward fluxes of reactive species from the solution to the gas phase follow Henry's law.

Furthermore, we assume that the solution in the dish is well stirred, such that the solution mixes very fast and the liquid-phase concentrations of all chemical species entering from the gas phase to the solution surface become immediately uniform in the volume. This is called a global or zero dimensional (0D) model. It is certainly not realistic even if the volume is small, especially for highly reactive species. Such species may react rapidly with other species at the moment they enter the solution, before being transported by advection or diffusion even for a few micrometers. However, in this study, we only consider the global model for the sake of simplicity as it allows us to calculate the evolution of chemical reactions over dozens of minutes.

In the global model, the concentration n_i of chemical species i in the solution is determined from the governing equation [80, 97, 98];

$$\frac{\partial n_i}{\partial t} = \hat{\Re}_i + \frac{1}{V} \cdot v_{\mathrm{th}} \left(S_{\mathrm{in}} \cdot n_i^{\mathrm{gas}} - S_{\mathrm{out}} \cdot \frac{n_i}{K_i^{\mathrm{H}} \cdot R \cdot T_{\mathrm{g}}} \right)$$

with thermal velocity

$$v_{\mathrm{th}} = \frac{1}{2} \sqrt{\frac{2 k_{\mathrm{B}} T_{\mathrm{g}}}{\pi m_i}}.$$

Here $n_i(t)$ is the concentration of the i-th chemical species in the solution at time t, V denotes the volume of the liquid, S_{in} is the area of plasma exposure on the solution surface ($S_{\mathrm{in}} = 0.1$ cm^2 in this study as discussed above), S_{out} is the area of the water surface ($S_{\mathrm{out}} = 10$ cm^2 in this study), K_i^{H} is Henry's constant for the species i in units of mol l^{-1}/atm with atm being the standard atmosphere (1 atm = 101,325 Pa), R is the gas constant, T_{g} is the gas temperature ($T_{\mathrm{g}} = 298.15$ K in this study), k_{B} is the Boltzmann constant (i.e., $R = N_{\mathrm{A}} k_{\mathrm{B}}$ with N_{A} being the Avogadro's constant), and m_i is the mass of the species i. The thermal velocity v_{th} is defined in such a way that $\Gamma_i = v_{\mathrm{th}} n_i^{\mathrm{gas}}$ represents the flux of the gas-phase species i entering the water surface under the assumption that the gas-phase species

i forms a Maxwellian distribution with temperature T_g. Henry's constants for all species considered in this study are given in Table B.5

Table 3.4: Henry's constant

No	Species	Henry's constant (mol L^{-1} atm $^{-1}$)	Ref.	No	Species	Henry's constant (mol L^{-1} atm $^{-1}$)	Ref.
1	H	$2.63x10^{-4}$	[202]	21	HNO_2	$5.0x10^{1}$	[19]
2	H_2	$7.8x10^{-4}$	[140]	22	HNO_3	$2.1x10^{5}$	[137]
3	O	$1.3x10^{-2}$	[142]	23	ONOOH	$1.26x10^{4}$	[197]
4	O_2	$1.3x10^{-3}$	[140]	24	HO_2NO_2	$4.0x10^{1}$	[138]
5	O_3	$1.1x10^{-2}$	[123]	25	HN_2O_2	∞*	-
6	OH	$3.0x10^{1}$	[81]	26	HN_2O_3	∞*	-
7	HO_2	$5.7x10^{3}$	[192]	27	Cl	$2.33x10^{1}$	[202]
8	H_2O_2	$8.3x10^{4}$	[178]	28	Cl_2	$9.32x10^{-2}$	[202]
9	HO_3	∞*	-	29	ClO	$7.09x10^{-1}$	[202]
10	N	$6.5x10^{-4}$	[142]	30	ClO_2	1.01	[202]
11	N_2	$6.1x10^{-4}$	[108]	31	Cl_2O	$1.72x10^{1}$	[202]
12	NH	$5.97x10^{1}$	[142]	32	HOCl	$6.59x10^{2}$	[202]
13	NO	$1.9x10^{-3}$	[140]	33	HOClH	$6.59x10^{2}$*	-
14	NO_2	$1.2x10^{-2}$	[38]	34	CO	$9.5x10^{-4}$	[202]
15	NO_3	1.8	[223]	35	CO_2	$3.4x10^{-2}$	[202]
16	N_2O	$2.5x10^{-2}$	[140]	36	HCO_3	∞*	-
17	N_2O_3	$2.6x10^{1}$	[55]	37	H_2CO_3	∞*	-
18	N_2O_4	1.6	[55]				
19	N_2O_5	1.97	[202]				
20	HNO	$4.67x10^{1}$	[202]				

The production/loss rate $\hat{\Re}_i$ of species i by the liquid-phase chemical reactions is given by

$$\hat{\Re}_i = -\sum_{i\in \mathrm{A,B,C,\cdots}} k^{\mathrm{PQR\cdots}}_{\mathrm{ABC\cdots}} [\mathrm{A}]^a [\mathrm{B}]^b [\mathrm{C}]^c \cdots + \sum_{i\in \mathrm{P,Q,R,\cdots}} k^{\mathrm{PQR\cdots}}_{\mathrm{ABC\cdots}} [\mathrm{A}]^a [\mathrm{B}]^b [\mathrm{C}]^c \cdots$$

for the chemical reaction

$$a\mathrm{A} + b\mathrm{B} + c\mathrm{C} + \cdots \xrightarrow{k^{\mathrm{PQR\cdots}}_{\mathrm{ABC\cdots}}} p\mathrm{P} + q\mathrm{Q} + r\mathrm{R} + \cdots$$

where the reaction among chemical species A, B, C, ... generate chemical species P, Q, R, ... with rate constant $k^{\mathrm{PQR\cdots}}_{\mathrm{ABC\cdots}}$. The summation $\sum_{i\in \mathrm{A,B,C,\cdots}}$ is taken over all such reactions with one of A, B, C, ... species being the i-th species. Similarly,

the summation $\sum_{i\in \mathrm{P,Q,R,\cdots}}$ is taken over all such reactions with one of P, Q, R, ... species being the i-th species. As mentioned in the previous section, we considered 60 liquid-phase chemical species (solutes), including solvated electrons, and 318 chemical reactions, which are the same as those given by Ikuse *et al.* in Ref. [98] as well as those in Table 3.3. To ensure that we maintain constant pH at 7 throughout the simulation, we employ the ideal buffer condition, i.e., set $[\mathrm{H^+}] = [\mathrm{OH^-}] = 10^{-7}$ mol l^{-1} at every time step in this study.

3.4 Results and Discussion

Concentrations of chemical species in PBS-like solution

Figure 3.2 shows the time evolution of the concentrations of all chemical species in the solution when a 3 mL PBS-like solution with a NaCl concentration of 0.137 mol l^{-1} is exposed to various types of plasmas described in Table3.1 for 100 s. The plasma feed gases are (a) Ar, (b) Ar/$\mathrm{H_2O}$, (c) Ar/Air, and (d) Ar/$\mathrm{O_2}$, and the distance between the plasma tip and the solution surface was 0.8 cm. The plasma-generated charge-neutral species shown in Tables3.1 are assumed to be the only gaseous species exposed to the solution surface with the densities given in the Table. No influx of ions or electrons from the gas phase is considered in the simulation for the sake of simplicity.

The time is measured from the moment of plasma exposure ($t = 0$). Prior to the plasma exposure ($t < 0$), the solution is in thermal equilibrium with ambient air at room temperature (i.e., 298.15 K) and 1 atm. During the plasma exposure ($t > 0$), the concentrations of gas-phase species are assumed to be constant in time. Although some chemical species are desorbed from the solution surface, they are assumed to dissipate immediately and therefore the gaseous species exposed to the solution surface remain as those given in Table3.1.

To show the most dominant species, Fig. 3.2 plots all chemical species in the solution whose concentrations are above 9×10^{-8} mol l^{-1}. More detailed simulation results showing all chemical species whose concentrations are above 10^{-14} mol l^{-1} for plasma irradiation up to 1,000 s are given in the supplementary material.

It is seen in Fig. 3.2 that the dominant chemical species generated under these

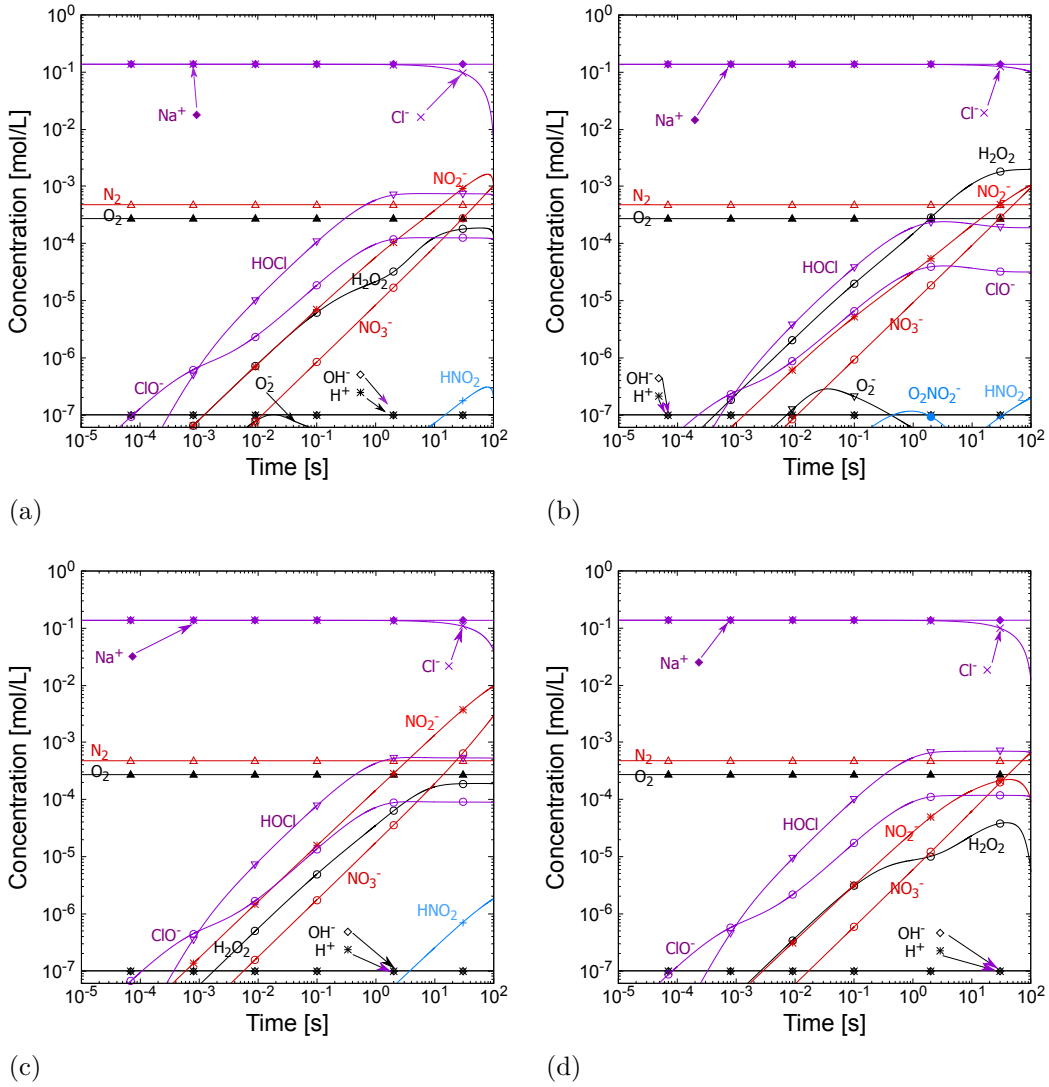

Figure 3.2: Time evolution of all chemical species present in the PBS-like solutions exposed to the plasmas discussed in this study, obtained from the numerical simulations. The system is at room temperature. The distance between the plasma tip and the solution surface was assumed to be 0.8 cm and the plasma feed gases were (a) Ar, (b) Ar/H2O, (c) Ar/Air, and (d) Ar/O_2. The concentrations of corresponding plasma-generated charge-neutral species are given in Tables 3.1. No influx of ions or electrons from the gas phase is considered in the simulation for the sake of simplicity. The vertical axis represents the concentrations in mol l^{-1}, and the horizontal axis indicates the plasma exposure time t in seconds. Both axes are on the log scale.

conditions are hypochlorous acid HOCl and its conjugate base, i.e., hypochlorite ClO^-, hydrogen peroxide(H_2O_2, nitrite $NO_2{}^-$ and nitrate $NO_3{}^-$. As will be demonstrated in Subsec. 3.4, the production of ClO^- is initiated with the reaction

$$Cl^- + O \longrightarrow ClO^-, \tag{3.1}$$

so the presence of O atoms in the gas phase contributed to the production of ClO^-. Hydrogen peroxide H_2O_2 is also directly dissolved into the solution from the gas phase.

The concentration of Cl^-, i.e., $[Cl^-]$, linearly decreases in time essentially with a constant rate because of Reaction (3.1). Such a linear decrease appears as a steep drop in the log-log plot, as seen in Fig. 3.2. Atomic oxygen O is constantly supplied from the gas phase to the solution and mainly lost with this reaction, so its concentration [O] is low and nearly constant (as seen in Figs. S1 – S4 of the supplementary material) until Cl^- in the solution runs out. Although we do not discuss details of the reaction pathways for Cl loss from the solution, it mainly desorb to the gas phase as HOCl. In the following subsections, we shall discuss how HOCl, ClO^- and H_2O_2 interact in the solution.

Production and loss of hydrogen peroxide H_2O_2

Hydrogen peroxide (H_2O_2) is a stable chemical species and known to have various biological effects. [216, 102, 82, 103] In this subsection, we examine the generation and loss mechanisms of H_2O_2 when the solution is exposed to the plasmas considered in this study.

Figure 3.3 shows the (a) production and (b) loss rates of H_2O_2 in the PBS-like solution exposed to the plasma with the Ar/O_2 feed gas given in Table 3.1. The corresponding evolution of liquid-phase species is given in Fig. 3.2(d). The dominant chemical reactions to produce and consume H_2O_2 are essentially the same also for other plasma conditions given in Tables 3.1 and 3.2.

On the production side, as seen in (a), two dominant sources of H_2O_2 are the chemical reaction

$$HO_2{}^- + H_2O \longrightarrow H_2O_2 + OH^- \tag{3.2}$$

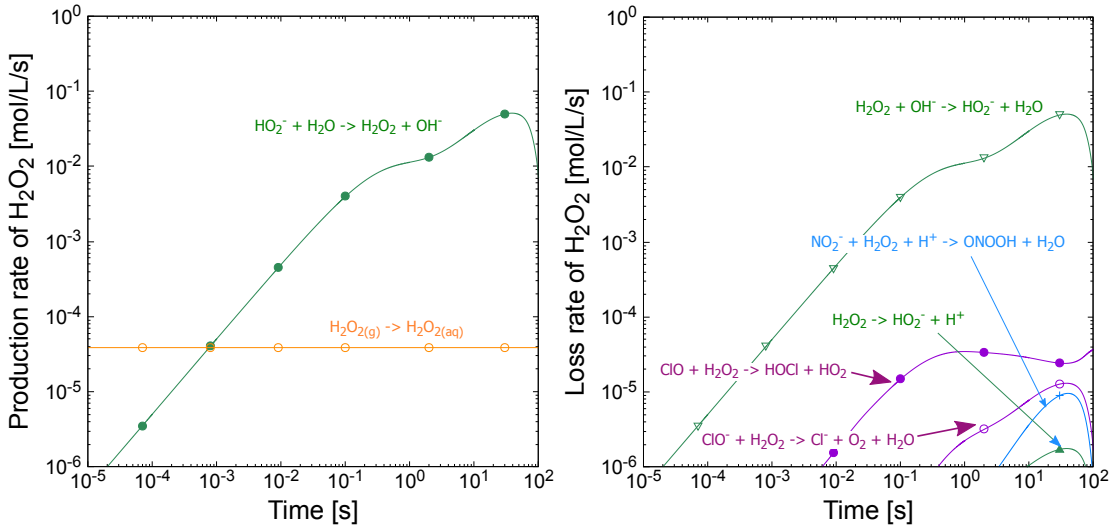

(a) (b)

Figure 3.3: Time evolution of the (a) production and (b) loss rates of H_2O_2 in the PBS-like solution under the conditions of Fig. 3.2(d). The vertical axis represents the absolute value of $d[H_2O_2]/dt$ of any chemical reaction that produces or consumes H_2O_2 considered in this study with a rate higher than 10^{-6} mol l^{-1} s^{-1}.

and the influx from the gas phase to the solution

$$H_2O_{2(g)} \longrightarrow H_2O_{2(aq)}\,. \tag{3.3}$$

Here the subscripts (g) and (aq) indicate the species is in the gas and liquid phases.

Reaction (3.2) is the loss of HO_2^-, i.e., the conjugate base of H_2O_2, which is essentially in equilibrium of the reverse reaction

$$H_2O_2 + OH^- \longrightarrow HO_2^- + H_2O\,. \tag{3.4}$$

Reactions (3.2) and (3.4) do not contribute to the production or loss of H_2O_2 in steady state. Therefore, the main source of H_2O_2 in the solution is the influx of gas-phase H_2O_2 given by Reaction (3.3).

Figure 3.3(b) shows that the net loss of H_2O_2 is mainly due to the following chemical reactions. The dominant chemical reactions to consume H_2O_2 are $R_{Cl}060$ of Table 3.3 and $R_{Cl}038$ of Ref. [98], i.e.,

$$ClO + H_2O_2 \longrightarrow HOCl + HO_2\,, \tag{3.5}$$

$$ClO^- + H_2O_2 \longrightarrow Cl^- + O_2 + H_2O\,, \tag{3.6}$$

and R_N024 of Ref. [98]

$$NO_2^- + H_2O_2 + H^+ \longrightarrow ONOOH + H_2O\,. \tag{3.7}$$

It should be noted that O_2 of Reaction (3.6) is singlet oxygen but we assume singlet oxygen immediately decays to the triplet ground state of O_2.

The rate constant of Reaction (3.5) is 3.0×10^8 L/mol/s, which is 5 orders of magnitude larger than the rate constant of Reaction (3.6), i.e., 2.8×10^3 L/mol/s. Therefore, even if the density of ClO is a few orders of magnitude smaller than that of ClO^-, Reaction (3.5) is the dominant loss reaction of H_2O_2. Indeed the density of ClO is shown to be far smaller than that of ClO^- in Fig. 3.2(d) or Fig. S4 of the supplementary material.

As will be discussed in the following subsection, the chlorine monoxide radical ClO is generated from hypochlorite ClO^- in the presence of hydroxyl radical OH and immediately consumed by the H_2O_2 decomposition reaction (3.5) to generate HOCl. Therefore ClO may be considered as an intermediate in the H_2O_2 decomposition reactions initiated by ClO^-.

Production and loss of hypochlorite ClO^-

As we saw in Fig. 3.2, ClO^- and HOCl are dominant species produced from Cl^- dissolved in the PBS-like solution exposed to the plasmas. Both species have strong bactericidal effects in liquid.[117, 57, 104]. In this subsection, we examine how these species are generated in the liquid phase. Figure 3.4 shows the (a) production and (b) loss rates of ClO^- in the PBS-like solution exposed to the plasma under the conditions of Fig. 3.2(d). The dominant chemical reactions to produce and consume ClO^- are essentially the same for other plasma conditions of Fig. 3.2 or Tables 3.1 and 3.2.

As seen in Fig. 3.4(a), the dominant chemical reactions to produce ClO^- are Reaction (3.1) and

$$HOCl + OH^- \longrightarrow ClO^- + H_2O\,. \tag{3.8}$$

Reaction (3.8) is the generation of the conjugate base ClO^- of HClO, which is in equilibrium with the reverse reaction at large time, i.e.,

$$ClO^- + H_2O \longrightarrow HOCl + OH^-\,. \tag{3.9}$$

In other words, Reactions (3.8) and its reverse reaction (3.9) do not contribute to the production and loss of ClO^- at large time t when they are in equilibrium. Therefore the main reaction to produce ClO^- is Reaction (3.1), caused by the influx of O atoms from the gas phase.

Figure 3.4(b) shows that the main loss mechanisms of ClO^- are the generation of the charge-neutral chlorine monoxide radical ClO, i.e.,

$$ClO^- + OH \longrightarrow ClO + OH^- \tag{3.10}$$

and the decomposition of H_2O_2 by Reaction (3.6).

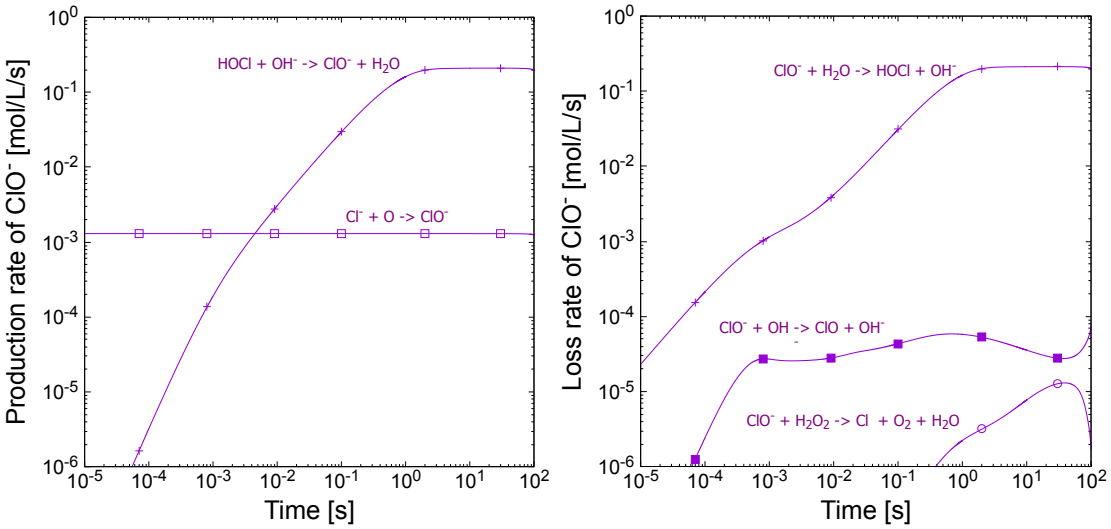

(a) (b)

Figure 3.4: Time evolution of the (a) production and (b) loss rates of ClO^- in the PBS-like solution under the conditions of Fig. 3.2(d). The vertical axis represents the absolute value of $d[ClO^-]/dt$ of any chemical reaction that produces or consumes ClO^- considered in this study with a rate higher than 10^{-6} mol l^{-1} s^{-1}.

Production and loss of chlorine monoxide ClO

Figure 3.5 shows the (a) production and (b) loss rates of ClO in the PBS-like solution exposed to the plasma under the conditions of Fig. 3.2(d). It is seen that the dominant source of ClO is Reaction (3.10) and its dominant loss mechanism is

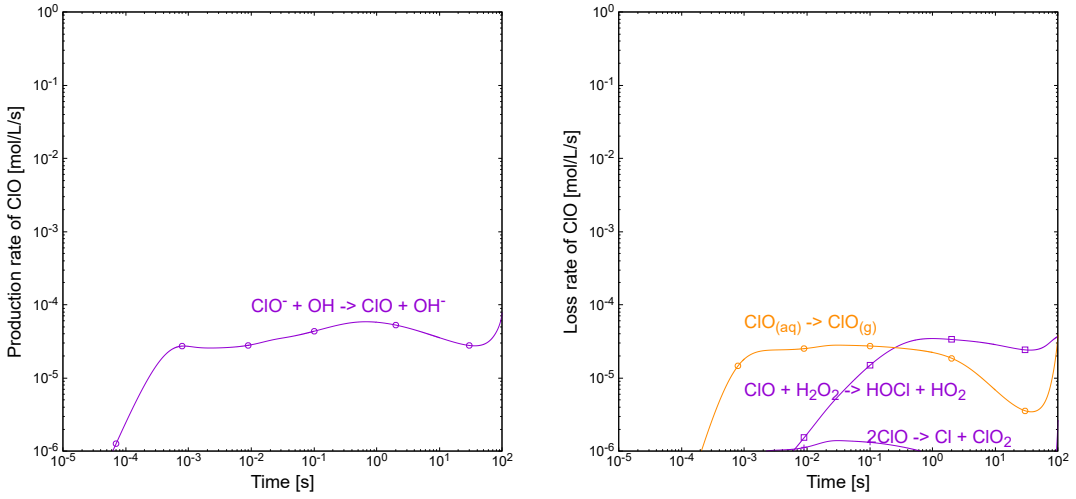

(a) (b)

Figure 3.5: Time evolution of the (a) production and (b) loss rates of ClO in the PBS-like solution under the conditions of Fig. 3.2(d). The vertical axis represents the absolute value of $d[\mathrm{ClO}]/dt$ of any chemical reaction that produces or consumes ClO considered in this study with a rate higher than 10^{-6} mol l^{-1} s^{-1}.

Reaction (3.5) at large time. For Reaction (3.10) to become the dominant reaction, a large amount of hydroxyl radical OH needs to be supplied. If it comes from the plasma, the location where this reaction occurs is limited to a thin reaction boundary layer of the medium at the gas-liquid interface. However, as we shall see momentarily, a required amount of OH radical is generated in the solution bulk. Therefore, Reaction (3.10) occurs in the solution bulk and, indeed, no OH radical needs to be supplied from the plasma directly for Reaction (3.10) to take place.

Figure 3.6 shows the (a) production and (b) loss rates of OH in the PBS-like solution exposed to the plasma under the conditions of Fig. 3.2(d). It is seen that the reaction

$$\mathrm{HOCl}^- \longrightarrow \mathrm{Cl}^- + \mathrm{OH}$$

and its reverse reaction

$$\mathrm{Cl}^- + \mathrm{OH} \longrightarrow \mathrm{HOCl}^-$$

are balanced and therefore do not contribute to the net production and loss of OH. The dominant reactions for the generation of OH radicals in the solution are the

reaction $R_{Cl}054$ of Ref [98], i. e.,

$$HOCl + O_2^- \longrightarrow Cl^- + O_2 + OH \tag{3.11}$$

and the influx of OH from the gas phase, i.e.,

$$OH_{(g)} \longrightarrow OH_{(aq)} .$$

As to Reaction (3.11), we already know that there is sufficient HOCl in the solution because it is a conjugate acid of ClO^- or generated from Reaction (3.9). Then where does the superoxide anion radical O_2^- come from?

The superoxide anion radical O_2^- is a conjugate base of the hydroperoxyl radical HO_2. If the reaction to decompose H_2O_2 by ClO, i.e., Reaction (3.5), occurs, HO_2 is generated, which can be converted to O_2^-. More specifically, we can look into the generation and loss of O_2^-. Figure 3.7 shows the (a) production and (b) loss rates of O_2^- in the PBS-like solution exposed to the plasma under the conditions of Fig. 3.2(d). It is seen that the reaction

$$HO_2 \longrightarrow O_2^- + H^+ \tag{3.12}$$

and its reverse reaction

$$O_2^- + H^+ \longrightarrow HO_2$$

are balanced at a relatively early stage, indicating HO_2 and O_2^- are a conjugate acid–base pair. So O_2^- coexists with HO_2. The loss of O_2^- is indeed mostly due to Reaction (3.11) at large time, which generates OH radical. On the other hand, Fig. 3.7(a) shows that initially O_2^- is mostly generated from HO_2.

So what is the dominant reaction that produces HO_2? Figure 3.8 shows the (a) production and (b) loss rates of HO_2 in the PBS-like solution exposed to the plasma under the conditions of Fig. 3.2(d). It is seen that initially HO_2 mostly comes from the gas phase. At large time, the dominant reaction to produce HO_2 is indeed Reaction 3.5), i.e., reaction to decompose H_2O_2 by ClO. The loss of HO_2 is to generate O_2^- via Reaction (3.12), as discussed earlier.

Loss mechanisms of H_2O_2 in the presence of Cl^-

To summarise the discussion above, we now know the major reaction pathways to decompose H_2O_2 in the PBS-like solution, i.e., in the presence of Cl^-, when the so-

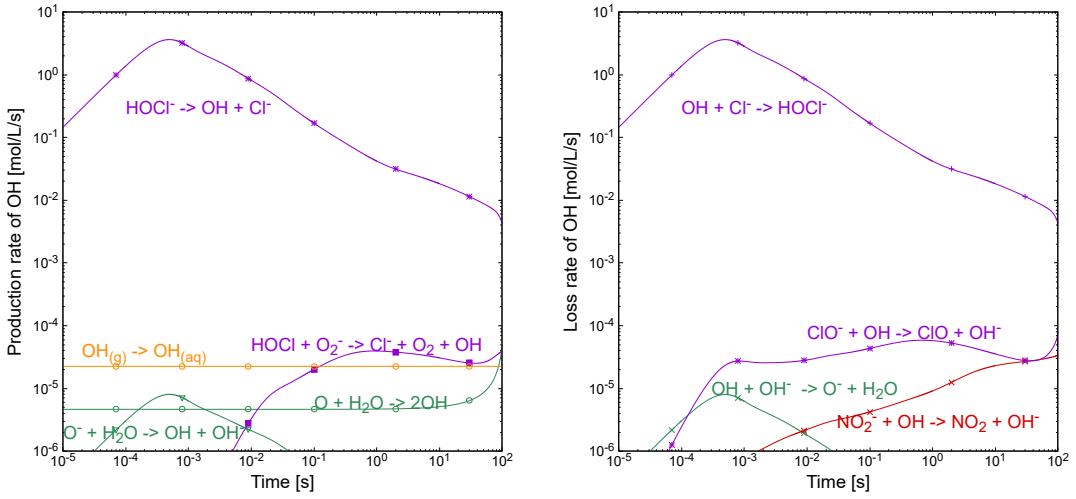

(a) (b)

Figure 3.6: Time evolution of the (a) production and (b) loss rates of OH in the PBS-like solution under the conditions of Fig. 3.2(d). The vertical axis represents the absolute value of $d[\mathrm{OH}]/dt$ of any chemical reaction that produces or consumes OH considered in this study with a rate higher than 10^{-6} mol l^{-1} s^{-1}.

lution is exposed to a plasma. The most important free radical species transported from the plasma to the liquid surface is the oxygen radical O. Through Reaction (3.1), ClO^- is generated in the solution. One reaction pathway to decompose $\mathrm{H_2O_2}$ is Reaction (3.6). However, this was not the dominant reaction pathway to decompose $\mathrm{H_2O_2}$ in the cases we examined in this study. The dominant reaction pathway is the following series of reactions that involves the generation of ClO. With a small amount of the hydroxyl radical OH, Reaction (3.10) generates the chlorine monoxide radical ClO. Then Reaction (3.5) decomposes $\mathrm{H_2O_2}$ and generates $\mathrm{HO_2}$. Because $\mathrm{HO_2}$ and $\mathrm{O_2}^-$ are a conjugate acid and base pair, the presence of $\mathrm{HO_2}$ means the presence of $\mathrm{O_2}^-$. Through Reaction (3.11), OH radicals needed for Reaction (3.10) are generated. In this way, a cycle of reactions (3.10), (3.5), and (3.11) continues as long as O radicals are provided from the plasma and $\mathrm{H_2O_2}$ and Cl^- exist in the PBS-like solution. Another mechanism to decompose $\mathrm{H_2O_2}$ by $\mathrm{NO_2}^-$ via Reaction (3.7) is not dominant in the cases examined in this study.

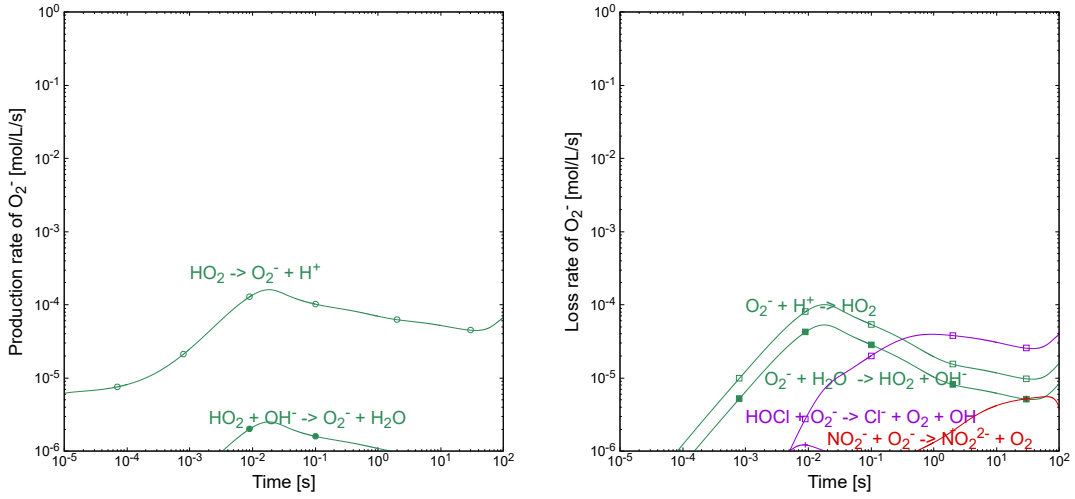

(a) (b)

Figure 3.7: Time evolution of the (a) production and (b) loss rates of O_2^- in the PBS-like solution under the conditions of Fig. 3.2(d). The vertical axis represents the absolute value of $d[O_2^-]/dt$ of any chemical reaction that produces or consumes O_2^- considered in this study with a rate higher than 10^{-6} mol l^{-1} s^{-1}.

Comparison with experiments

Figure 3.9 compares the H_2O_2 concentrations obtained from the experiments by Wende *et al.* [240] with those obtained from the numerical simulation of this study. The experimental and simulation conditions are the same as those given in Fig. 3.2, i.e., 3 mL PBS solutions with a NaCl concentration of 0.137 mol l^{-1} exposed to plasmas with feed gases of Ar, Ar/H_2O, Ar/Air, and Ar/O_2 at room temperature. The distance between the nozzle and the solution surface was set at 0.8 cm. The white bars represent the experimental values quoted from Ref. [240] and the hatched bars represent the values obtained from the simulations shown in Fig. 3.2. The H_2O_2 concentration data for Ar and Ar/H_2O were obtained at t = 60 s and those for Ar/Air and Ar/O_2 were obtained at t = 360 s, as in the experimental conditions. It is seen that, in the case of the Ar-feed-gas plasma, the agreement between the experiment and simulation is excellent. In the cases of the Ar/Air and Ar/O_2 feed gases, no H_2O_2 was observed in experiments while the simulations also showed low H_2O_2 concentrations. In the case of the Ar/H_2O-feed-

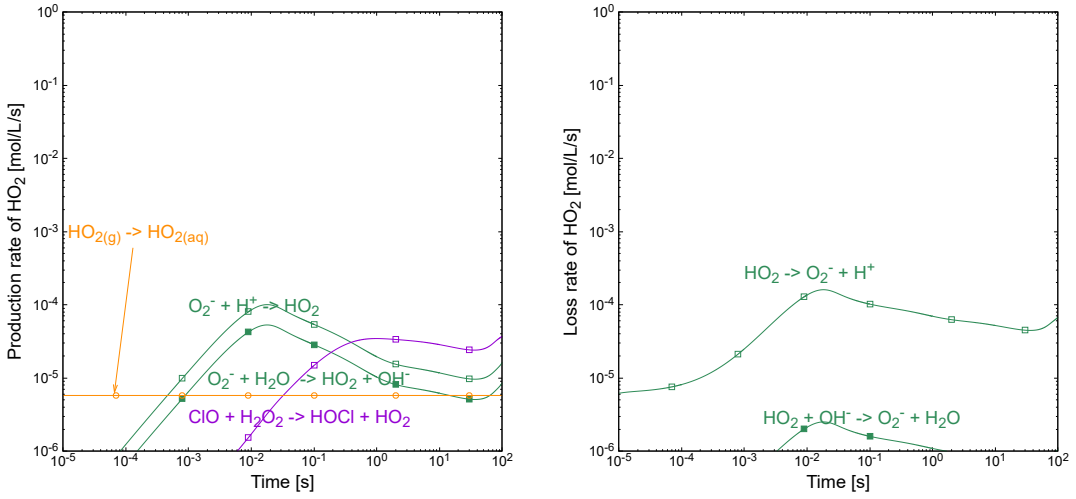

(a) (b)

Figure 3.8: Time evolution of the (a) production and (b) loss rates of HO_2 in the PBS-like solution under the conditions of Fig. 3.2(d). The vertical axis represents the absolute value of $d[HO_2]/dt$ of any chemical reaction that produces or consumes HO_2 considered in this study with a rate higher than 10^{-6} mol l^{-1} s^{-1}.

gas plasma, both experiment and simulation show relatively large concentrations of H_2O_2. This is because, in the case of the Ar/H_2O feed gas, the gas-phase densities of H_2O_2 were larger while that of O was smaller than those in the other cases and, therefore, H_2O_2 in the solution was not much decomposed by ClO^-.

Figure 3.9 suggests that, for a given influx of H_2O_2 to a plasma-irradiated PBS solution, the H_2O_2 concentration in the solution, i.e., $[H_2O_2]_{(aq)}$, decreases with an increasing influx of O radicals. Figure 3.10 plots the H_2O_2 concentrations in plasma-irradiated PBS solutions under the the same conditions as those in Ref. 3.2 with gas phase species given in Tables 3.1 and 3.2 obtained from numerical simulations as functions of the gas-phase density ratio of O to H_2O_2, i.e., $[O]_{(g)}/[H_2O_2]_{(g)}$. The values of $[H_2O_2]_{(aq)}$ were evaluated at $t = 60$ s. The experimental data shown in Fig. 3.9 are also plotted. A clear trend is seen that the H_2O_2 concentration decreases with the increasing gas-phase-density ratio of O to H_2O_2.

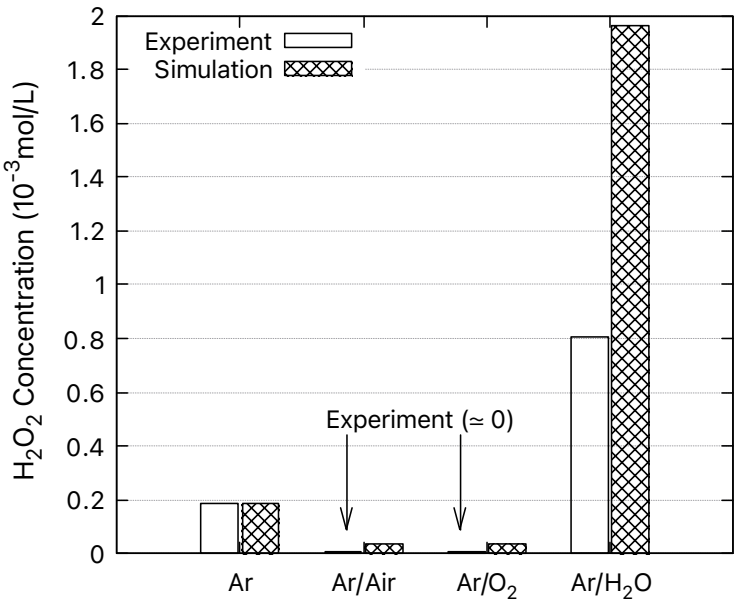

Figure 3.9: The concentration of H_2O_2 from the experiments by Wende *et al.* [240] (white bars) and the corresponding simulations of this study (hatched bars). The horizontal axis indicates the plasma conditions summarized in Tables 3.1 and 3.2. The data for Ar and Ar/H_2O plasmas were obtained at $t = 60$ s whereas the data for Ar/Air and Ar/O_2 plasmas were obtained at $t = 360$ s.

Simulation of O and H_2O_2 irradiation

The study so far indicates that the only plasma-generated species needed to decompose H_2O_2 in the PBS-like solution is O radicals. To confirm this, we now simulate the case where the surface of the PBS-like solution is irradiated only by H_2O_2 and O radicals. Figure 3.11 shows the time evolution of the concentrations of all chemical species in the PBS-like solution exposed to the influx of H_2O_2 only (a) and the influxes of H_2O_2 and O radicals (b) at room temperature for 100 s, obtained from the numerical simulations. The PBS-like solution prior to the irradiation of H_2O_2 and O is the same as those used in the simulations presented in Fig. 3.2, i.e., a 3 mL solution with a NaCl concentration of 0.137 mol l^{-1} in thermal equilibrium with ambient air at room temperature (i.e., 298.15 K) and 1 atm. As before, the PBS-like solution is assumed to be placed in a container with a surface area of 10 cm^2 and the area of the solution surface exposed to H_2O_2 and

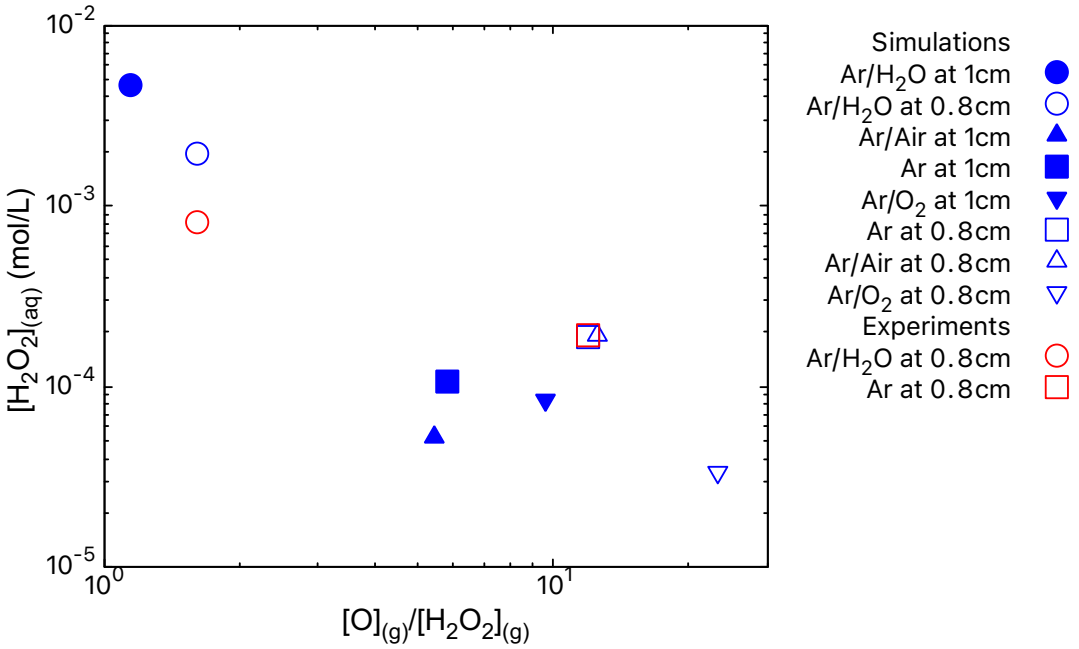

Figure 3.10: The concentration of H_2O_2 in the PBS-like solution, i.e., $[H_2O_2]_{(aq)}$, evaluated from the numerical simulations at $t = 60$ s as a function of the gas-phase density ratio of O to H_2O_2, i.e., $[O]_{(g)}/\ [H_2O_2]_{(g)}$. The plasma conditions are those described in Tables 3.1 and 3.2. The corresponding experimental data [240] shown in Fig. 3.9 are also plotted. The legends indicate the types of feed gases and the distance between the nozzle of the plasma system and the solution surface.

O influxes is assumed to be limited to 0.1 cm^2. During the H_2O_2 and O exposure ($t > 0$), the concentrations of gas-phase species are assumed to be constant in time, as before. We also assume that the gas-phase concentration of H_2O_2 at the gas-liquid interface is $[H_2O_2]_{(g)} = 1.49\times10^{14}$ cm^{-3} (as in the case of the Ar plasma in Table 3.2) and the gas-phase density ratio of O to H_2O_2 for (b) is $[O]_{(g)}/\ [H_2O_2]_{(g)} = 10$ at the gas-liquid interface.

It is seen in (a) that the concentration of H_2O_2 linearly increases in time due to the constant influx of H_2O_2. Here, no ClO^- is produced because there is no $O_{(g)}$ supplied to the solution. On the other hand, in (b), where O is also supplied to the solution, the generation of HOCl and ClO^- is observed and the net generation of H_2O_2 is suppressed after around $t = 1$ sec.

Figure 3.12 shows the concentrations of ClO^- and H_2O_2 in the PBS-like solution

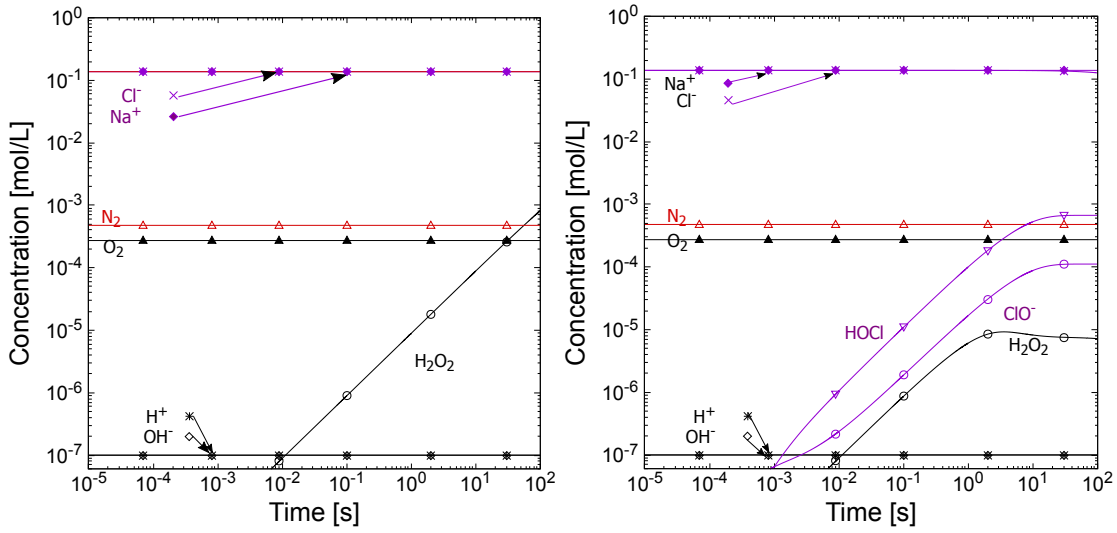

(a) (b)

Figure 3.11: Time evolution of all chemical species present in the PBS-like solutions exposed to the influx of H_2O_2 only (a) and the influxes of H_2O_2 and O radicals (b) at room temperature, obtained from the numerical simulations. The gas-phase concentration of H_2O_2 at the gas-liquid interface is $[H_2O_2]_{(g)} = 1.49\times10^{14}$ cm^{-3} and the gas-phase density ratio of O to H_2O_2 for (b) is $[O]_{(g)}/ = 10$. The vertical axis represents the concentrations in mol l^{-1}, and the horizontal axis indicates the plasma exposure time t in seconds. Both axes are on the log scale.

at $t = 50$ s as functions of the gas-density ratio of $[O]_{(g)}/\ [H_2O_2]_{(g)}$. It should be noted that $[ClO^-] = 0$ when $[O]_{(g)} = 0$. It is clearly seen that the increase of the O radical supply to the PBS-like solution increases the production of ClO^- and reduces the concentration of H_2O_2.

Figure 3.13 shows the (a) production and (b) loss rates of H_2O_2 in the PBS-like solution exposed to the influxes of H_2O_2 and O with a gas-phase density ratio of $[O]_{(g)}/\ [H_2O_2]_{(g)} = 10$ at the gas-liquid interface. The corresponding evolution of liquid-phase species is given in Fig. 3.11(b). As in Fig. 3.3, beside the equilibrium relation between Reaction (3.2) and its reverse reaction (3.4), the main source of H_2O_2 in the solution is the influx of gas-phase H_2O_2 and the main loss of H_2O_2 is due to Reactions (3.5) and (3.6). Therefore, we conclude that the same sequences of reactions discussed above are in charge of the decomposition of H_2O_2 in the case of Fig. 3.11(b).

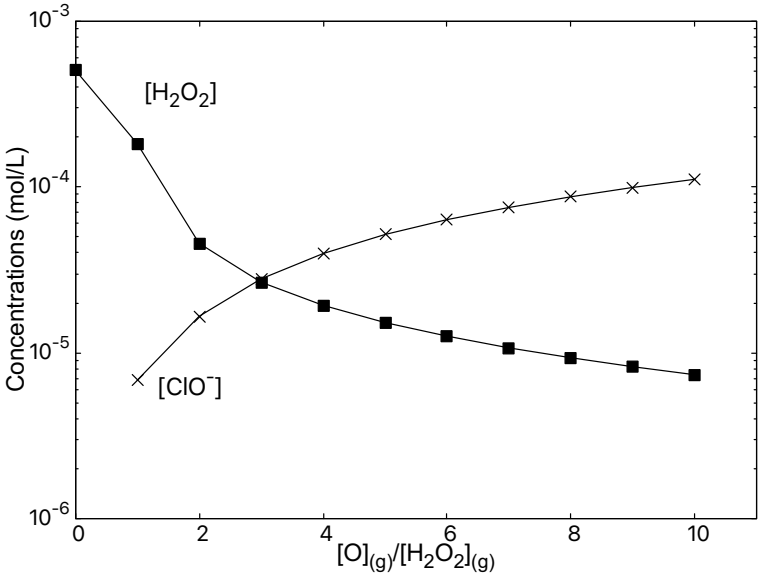

Figure 3.12: The concentrations of ClO^- and H_2O_2 in the PBS-like solution evaluated from the numerical simulations at $t = 60$ s as a function of the gas-phase density ratio of O to H_2O_2, i.e., $[O]_{(g)}/\ [H_2O_2]_{(g)}$. Other conditions are the same as those in Fig. 3.11. It should be noted that $[ClO^-] = 0$ when $[O]_{(g)} = 0$. It is seen that, as $[O]_{(g)}$ increases, $[ClO^-]$ increases while $[H_2O_2]$ decreases.

Figure 3.14 summarizes the finding of this study. Although H_2O_2 was supplied from the plasma in this study, H_2O_2 coming from any sources can be decomposed by incident O atoms in a chlorinated solution. The most important ingredients for H_2O_2 decomposition are Cl^- ions in the solution and O atoms supplied from the plasma, which form ClO^-. There are two major pathways to decompose H_2O_2 in the presence of ClO^-. One is the reaction denoted by ① in Fig. 3.14, which is Reaction (3.6) and directly decomposes H_2O_2 to generate water H_2O and oxygen O_2. The other pathway is denoted by ②, which forms a cycle of reactions consisting of Reactions (3.10), (3.5), and (3.11). Here we call the reaction cycle a "chlorine monoxide cycle" as it involves the chlorine monoxide radical ClO as an intermediate. The chlorine monoxide cycle consumes both ClO^- and H_2O_2 and generates water H_2O and oxygen O_2, as in Reaction (3.6). Therefore it may not be easily distinguished from Reaction (3.6) experimentally. The chlorine monoxide cycle requires an OH radical to convert ClO^- to ClO but also generates an

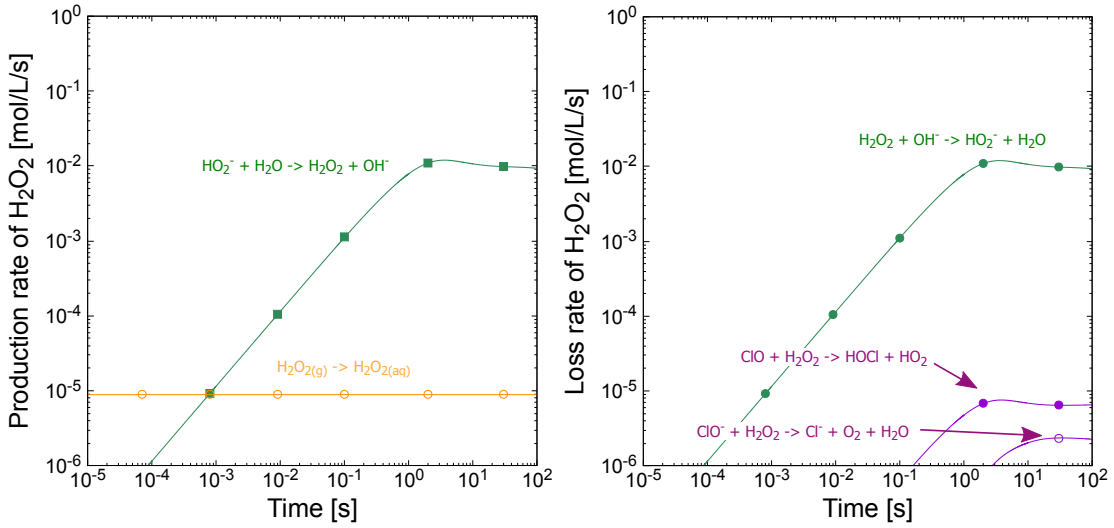

(a) (b)

Figure 3.13: Time evolution of the (a) production and (b) loss rates of H_2O_2 in the PBS-like solution under the conditions of Fig. 3.11(b). The vertical axis represents the absolute value of $d[H_2O_2]/dt$ of any chemical reaction that produces or consumes H_2O_2 considered in this study with a rate higher than 10^{-6} mol l^{-1} s^{-1}.

OH radical as one of its byproducts. Therefore, once the cycle is triggered by a small amount of OH in the solution, (which is supplied from the gas phase in this study, as seen in Fig. 3.6(a)) the cycle continues until O or H_2O_2 runs out. In the presence of Cl^- ions in the solution, the net total reaction by either Reaction (3.6) or the chlorine monoxide cycle may be summarized as

$$O + H_2O_2 \longrightarrow H_2O + O_2$$

if no intermediate reaction is taken into account explicitly.

3.5 Conclusions

In this study, global (zero-dimensional) simulations have been performed to identify the dominant chemical reactions in a PBS-like solution exposed to APPs. Especially the interest lies in identifying the chemical reaction pathways for the

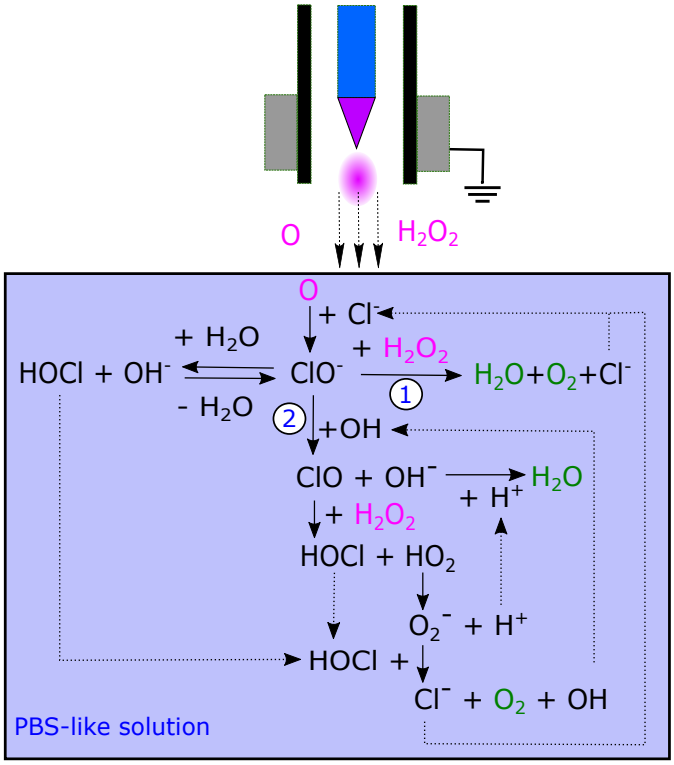

Figure 3.14: Major reaction pathways for the decomposition of H_2O_2 in the presence of Cl^- in the solution. O and H_2O_2 are assumed to be provided from the plasma source. There are two reaction pathways; ①, i.e., Reaction (3.6), which is the direct decomposition of H_2O_2 and ②, i.e., a series of reactions (3.10), (3.5), and (3.11) that also consumes H_2O_2 and generates H_2O and O_2 as net products (chlorine monoxide cycle).

decomposition of H_2O_2 in the presence of Cl^- ions in the solution exposed to plasmas. In the simulations, we assumed that the gas-phase chemical species identified in the earlier study by Wende *et al.* [240] were supplied to the surface of a PBS-like solution and compared the simulation results with the experimental observations of Ref. [240]. They were found to be in good qualitative agreement, indicating that O radicals supplied from the plasma to the PBS solution cause the decomposition of H_2O_2 in the solution. Thus our study corroborates the reaction mechanisms of H_2O_2 decomposition in plasma-exposed PBS solutions proposed by Wende *et al.* [240]: the formation of ClO^- via Reaction (3.1), which then decomposes H_2O_2 and generates water H_2O and oxygen O_2.

Wende *et al.* listed Reaction (3.6) as a possible mechanism of the H_2O_2 decomposition by ClO^-. However, our study has found the chlorine monoxide cycle is another reaction pathway that decomposes H_2O_2. Indeed, both reaction pathways consume ClO^- and H_2O_2 and generate water H_2O and oxygen O_2, so they may not be easily distinguished experimentally. The major difference between Reaction (3.6) and the chlorine monoxide cycle is that, while Reaction (3.6) requires only ClO^- and H_2O_2 to proceed, the chlorine monoxide cycle requires OH radicals to initiate the cycle and also involves the reaction with some intermediates such as OH, HO_2 and $O_2{}^-$. If some of these intermediates are scavenged by other reactions, the chlorine monoxide cycle may be interrupted.

In this study, the chlorine monoxide cycle is found to be the dominant mechanism to decompose H_2O_2 because there is a sufficient amount of OH supplied from the gas phase that initiates this reaction pathway. In reality, the chlorine monoxide cycle is likely to be the dominant consumption mechanism of H_2O_2 only near the gas-water interface region, where the OH density is relatively high. In the bulk of the solution, H_2O_2 may be directly decomposed by ClO^-, i.e., Reaction (3.6).

Neither Reaction (3.6) nor the chlorine monoxide cycle requires the presence of any other nitrogen-containing species. A recent study by Jiráek and Lukeš [104] pointed out that, in the presence of nitrites $NO_2{}^-$, the concentration of HOCl can be reduced due to the oxidation of $NO_2{}^-$ by HOCl. The oxidation of $NO_2{}^-$ by HOCl is known to be triggered by the formation of chlorine nitrite $ClNO_2$ and a set of reactions that leads to the formation of nitrates $NO_3{}^-$ [128] is rather complex. Therefore, these reactions are not taken into account in our simulation model. Nevertheless, we believe that, under the conditions that we examined in this study, HOCl is not depleted significantly by oxidation in reality because it is also known that the formation of $NO_3{}^-$ from $ClNO_2$ is a rather slow process. Indeed our simulation results without $NO_2{}^-$ oxidation by HOCl are consistent with the experimental observations by Wende *et al.*, so our current model is likely to be sufficient. A more detailed study including $NO_2{}^-$ oxidation by HOCl is deferred to future work.

In the presence of $NO_2{}^-$, Reaction (3.7) can decompose H_2O_2. Under the conditions examined in this study, however, this reaction was found to be less important for H_2O_2 decomposition than Reaction (3.6) or the chlorine monoxide

cycle.

Chapter 4

One-dimensional Reaction Transport Simulation to find position of the reactions

4.1 Introduction

Atmospheric pressure plasma (APPs) have found widespread application in various fields,[105, 249, 235, 130, 206, 87, 41, 30, 4, 239, 3] encompassing material surface treatment,[111, 110, 234, 221, 171, 199, 12, 13, 193, 210, 165, 228, 63, 129] nanoparticle synthesis, [68, 195, 67, 227, 122, 120] gas and liquid treatment,[118, 150, 218, 164, 20, 109, 211, 37, 250] sterilization, wound healing, and other medical applications.[131, 213, 96, 248, 219, 149, 56, 65, 134, 77, 160, 18, 162, 161, 225, 17, 93] Given the breadth of its applications, deciphering the intricacies of plasma-liquid interactions is of paramount importance in elucidating the underlying mechanisms and identifying the relevant reactive species.[113, 14, 215, 216, 177, 217, 31]

Numerical simulations of gas- and liquid-phase chemical reactions have been widely employed to investigate the reaction mechanisms in solutions exposed to plasmas. These simulations incorporate varying levels of chemical reaction complexity, spatial dimensions, and temporal and spatial resolutions, which are tailored to the specific research objectives.[80, 224, 148, 142, 147, 97, 155, 98, 11, 10] Chemical species found in a solution exposed to a plasma are closely linked to

the influxes of chemical species generated in the plasma. Gas-phase chemistry can also be extremely complex, and the gas-phase reactions and transport can proceed on time scales different from those in the liquid phase. Therefore, solving of both gas- and liquid-phase process models simultaneously with the full scale of chemical-reaction complexity remains a challenge for computation studies of low-temperature plasmas. [126, 200, 144, 119, 167, 169]

APPs are typically generated with pulsed discharges to avoid excessive heating of the surrounding gas. The ionization rates of APPs are generally low, but frequent collisions among electrons and gas molecules lead to the generation of a large amount of highly reactive species. An APP generated in humid air is an efficient source of reactive oxygen species (ROS) and reactive nitrogen species (RNS). Hydrogen peroxide (H_2O_2) is a relatively stable species generated under such conditions. When a water solution is exposed to an APP, the gas above the solution surface has a high concentration of gaseous water (H_2O) molecules, where H_2O_2, ROS and RNS are generated and dissolve in the solution through the gas-water interface, i.e., solution surface. [151, 205]

It is known that, if a saline solution is exposed to an APP, hypochlorous acid (HOCl) is generated in the solution. Bactericidal effects of HOCl are well documented. [6, 66] In water, HOCl is in chemical equilibrium with hypochlorite anion ClO^-. At pH = 7, the ratio of HOCl to the total amount of HOCl and ClO^- is 76 %. A recent study by Wende *et al.*[240] found that, when a phosphate-buffered saline (PBS) solution was exposed to APPs, the amount of H_2O_2 observed in the solution could be reduced, especially when the amount of admixed oxygen gas O_2 was high for plasma generation. Based on the experimental observations, they concluded that ClO^- formed in the plasma-exposed solution decomposed H_2O_2.

In our previous study,[11] the mechanism of H_2O_2 decomposition in a chlorine-containing solution was elucidated. The decomposition of H_2O_2 was predominantly driven by ClO^- and ClO through the chlorine monoxide cycle. The study employed a global model, assuming that the solution is well-mixed, resulting in uniform species concentration and distribution regardless of depth.

The goal of this study is to investigate the mechanism of H_2O_2 decomposition and determine the reaction location. We utilize a one-dimensional reaction-transport simulation, an extension of the global model that incorporates depth-

dependent calculations. The same model has been previously applied to investigate plasma irradiation of pure water and plasma irradiation of NaCl- containing water.[98]

Numerical simulations of chemical reactions in solutions have been extensively employed to investigate the reaction mechanisms within the solution. These simulations incorporate varying levels of chemical reaction complexity, spatial dimensions, temporal and spatial resolutions, which are tailored to the specific research objectives.[80, 224, 148, 142, 146, 97, 155] In plasma-liquid interaction modeling, the chemical species in the liquid are intricately linked to the gas-phase chemical species present in the plasma. The gas phase typically involves a significantly larger variety of chemical species compared to the liquid phase. Consequently, rigorous and detailed numerical simulations of both gas-phase and liquid-phase chemical reactions remain a challenging research area.[126, 200, 144, 119, 166, 168] This is because numerical simulations can provide insights into phenomena that are often difficult or impossible to observe experimentally.

4.2 Outline of numerical simulation

Governing equations and boundary conditions

The motivation of this study is to understand the transport process of chemical species and find out the primary reactions leading to the decomposition of H_2O_2 in a PBS solution. We consider a system where a PBS solution is exposed to plasma jets, which is schematically illustrated in Fig. 4.1. Plasma jets produce various chemical species in the gas phase, [240] which may dissolve in the PBS solution and cause various chemical reactions there.

In this study, we employ a 1D reaction-transport model to simulate numerically the dynamics of the concentration depth profiles of chemical species in a PBS solution. We assume that the PBS solution is in equilibrium with air at a pressure of 1 atm and at room temperature (298.15 K). It is assumed that, during the plasma jet exposure, the PBS solution continues to be in equilibrium with air under the same conditions, so that the concentrations of oxygen (O_2) and nitrogen (N_2) molecules dissolved in the solution remain uniform and constant. The initial

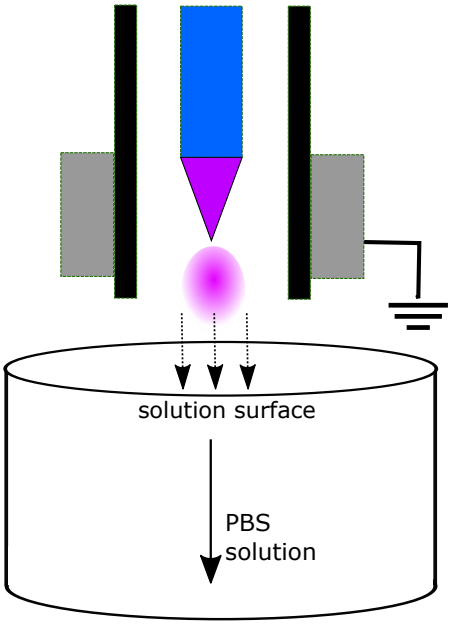

Figure 4.1: Schematic picture of a PBS solution irradiated by an atmospheric pressure plasma (APP) jet. The vertical cross-section of a plasma jet system is illustrated, where a plasma jet, depicted as a spherical object in the center, is generated near the tip of the central metal electrode. The electrode is surrounded by a cylindrical wall made of a dielectric material (depicted in black). A metal grounded electrode is attached to the outside of the dielectric cylinder. Gas-phase chemical species generated in the plasma jet are transported (depicted by the dotted arrows) to the solution surface and dissolve in the solution. Chemical species generated in the solution are transported toward the solution bulk (depicted by the solid arrow).

concentrations of Na^+ and Cl^- in the solution are assumed to be 0.137 mol/l with a constant pH of 7. We also assume that the solution is an ideal buffer solution, such that the pH value of the solution is instantly restored to 7. Therefore, the concentrations of H^+ and OH^- are assumed to be exactly 1.0×10^7 mol/l at every instance of time. In the simulations presented in this work, 60 liquid-phase species (solutes), including solvated electrons, and 318 chemical reactions, including 77 ROS and water reactions, 77 RNS reactions, 54 chlorine reactions, and 2 other reactions related to Na were considered, as in the earlier study of [11]

The governing equations for transport and chemical reactions are given by

$$\frac{\partial n_i}{\partial t} = \hat{\Re}_i - \mathbf{v}_\mathrm{c} \cdot \nabla n_i - \mu_i \nabla \cdot (n_i \boldsymbol{E}) + D_i \Delta n_i \,, \tag{4.1}$$

Where t denotes time, n_i is the concentration of the i-th species in the liquid phase (i.e., solution), $\mathbf{v}_\mathrm{c}$ represents the convective flow velocity in the solution. Since there is no convection flow of the PBS solution in the container under the experimental conditions that we are interested in (i.e., experimental conditions of [240]), we assume $\mathbf{v}_\mathrm{c} = 0$ in this study. The notation $\hat{\Re}_i$ denotes the calculated change in concentration for species i (n_i, see Tab. B.12 and Tab. B.11), determined from its production and loss rates. The electric field $\boldsymbol{E}$ is obtained from Poisson's equation. Parameters μ_i and D_i are the mobility and diffusion coefficient of the i-th species, the values of which are listed in Tab. B.12[97, 98]. In the 1D model, the spatial coordinate x is taken in the direction of the depth with $x = 0$ being the position of the solution surface, and therefore $\nabla = \mathbf{e}_\mathrm{x}\, \partial/\partial x$ with $\mathbf{e}_\mathrm{x}$ is the unit vector in the direction of the depth.

The boundary conditions at the solution surface are governed by the relation

$$v_i^\mathrm{th} \left(n_i^\mathrm{g} - \frac{n_i}{k_i^\mathrm{H} R T_\mathrm{g}} \right) = -D_i \frac{\partial}{\partial x} n_i \,,$$

where v_i^th, n_i^g, and k_i^H represent thermal velocity, the gas-phase density, and Henry's constant of the i-th species. The values of Henry's constants are found in [97, 98]. Here, R and T_g represent the gas constant and the gas temperature, respectively. The gas temperature is assumed to be the same as the solution temperature (T), i.e., $T_\mathrm{g} = T$ (=298.15 K). The thermal velocity is defined as

$$v_i^\mathrm{th} = \frac{1}{2} \sqrt{\frac{2 k_\mathrm{B} T_\mathrm{g}}{\pi m_i}} \,,$$

where m_i is the atomic/molecular mass of the i-th species, under the assumption that the i-th gas-phase species forms a Maxwellian distribution with gas temperature T_g. With this thermal velocity, the component of the flux of the i-th gas-phase species normal to the solution surface is given by $\Gamma_i = v_i^\mathrm{th}\, n_i^\mathrm{g}$. The boundary condition above essentially states that the difference between the incoming flux from the gas phase and the outgoing flux from the liquid due to Henry's law is the flux

that diffuses into the solution. A more comprehensive explanation of the governing equations may be found in Ref. [97]

Table 4.1: Densities of gas-phase species generated under the conditions denoted by Ar, Ar/H_2O, Ar/Air, and Ar/O_2 at 0.8 cm from the nozzle exit, extracted from the numerical simulation data given in Ref. [240]. The discharge conditions are described in the main text.

Species	Gas-phase densities (cm^{-3})			
	Ar cm^{-3}	Ar/H_2O cm^{-3}	Ar/Air cm^{-3}	Ar/O_2 cm^{-3}
H	2.71×10^{11}	1.45×10^{11}	1.01×10^{12}	1.28×10^{11}
H_2O_2	1.36×10^{14}	3.83×10^{14}	9.34×10^{13}	6.48×10^{13}
HNO_2	1.63×10^{14}	1.48×10^{14}	3.34×10^{14}	7.09×10^{13}
HNO_3	1.86×10^{13}	2.08×10^{13}	3.69×10^{13}	1.30×10^{13}
HO_2	1.67×10^{13}	2.54×10^{13}	9.44×10^{12}	9.54×10^{12}
N	6.65×10^{13}	4.82×10^{13}	5.03×10^{13}	2.98×10^{13}
N_2O_5	8.00×10^{12}	2.74×10^{11}	4.09×10^{12}	6.23×10^{11}
NO	1.47×10^{14}	1.40×10^{14}	1.53×10^{14}	1.41×10^{14}
NO_2	2.81×10^{13}	2.94×10^{13}	3.31×10^{13}	2.49×10^{13}
O	1.63×10^{15}	6.17×10^{14}	1.17×10^{15}	1.50×10^{15}
O_3	9.67×10^{14}	3.13×10^{14}	1.31×10^{15}	2.63×10^{15}
OH	3.74×10^{13}	4.09×10^{13}	2.26×10^{13}	2.67×10^{13}

The densities in the gas phase species generated by an APP are taken from the simulation result by Wende et al.[240] The list of species and densities is shown in table 4.1. The calculation in the boundary condition of the gas phase and liquid phase for charge-neutral species is given by the Eq. 4.1.

Gas injection is assumed in continuous and constant. In the liquid phase (n_i^{liq}) the concentration will increase and reach the solubility limit. The solubility limit is the maximum concentration of each species soluble in the solution when the solution is in thermal equilibrium with the gas at its partial pressure. The solubility limit of species i given by

$$n_i^{liq} = k_i^H R T_g n_i^{gas}$$

Here the n_i^{sol} represents the concentration as a solubility limit of species i. Here we can see that the solubility limit depends on Henry's constant. If Henry's constant is low, the solubility limit of the species is also low. The calculated value of the solubility limit of each chemical species is shown in table 4.2.

Table 4.2: Solubility limit of each species inside PBS-like solution from four different gas feeds

No	Species	Incident flux Ar ($mol\ L^{-1}$)	Ar/H2O ($mol\ L^{-1}$)	Ar/Air ($mol\ L^{-1}$)	Ar/O2 ($mol\ L^{-1}$)
1	H	2.93×10^{-15}	1.57×10^{-15}	1.09×10^{-15}	1.39×10^{-16}
2	H_2O_2	4.65×10^{-4}	1.31×10^{-3}	3.19×10^{-5}	2.21×10^{-5}
3	HNO_2	3.36×10^{-7}	3.05×10^{-7}	6.87×10^{-8}	1.46×10^{-8}
4	HNO_3	1.61×10^{-4}	1.80×10^{-4}	3.19×10^{-5}	1.12×10^{-5}
5	HO_2	3.92×10^{-6}	5.96×10^{-6}	2.21×10^{-7}	2.24×10^{-7}
6	N	1.78×10^{-12}	1.29×10^{-12}	1.35×10^{-13}	7.97×10^{-14}
7	N_2O_5	6.49×10^{-10}	2.22×10^{-11}	3.32×10^{-11}	5.05×10^{-12}
8	NO	1.15×10^{-11}	1.09×10^{-11}	1.20×10^{-9}	1.10×10^{-12}
9	NO_2	1.39×10^{-11}	1.45×10^{-11}	1.63×10^{-12}	1.23×10^{-12}
10	O	2.72×10^{-11}	1.03×10^{-9}	1.96×10^{-10}	2.51×10^{-10}
11	O_2	2.72×10^{-4}	2.72×10^{-4}	2.72×10^{-4}	2.72×10^{-4}
12	O_3	4.38×10^{-9}	1.42×10^{-10}	5.93×10^{-11}	1.19×10^{-10}
13	OH	4.62×10^{-8}	5.05×10^{-8}	2.79×10^{-9}	3.30×10^{-9}

In the gas phase, we find the charge-neutral species and charged species. We assume that no charge species desorb from the surface thermally. For the charged species, we specify their incident fluxes by their electric currents. The mathematical formula for the boundary condition for charged species is described by

$$\frac{\boldsymbol{j}_i \cdot \boldsymbol{n}}{q_i} = \left(-D_i \nabla n_i^{liq} + \mu_i n_i^{liq} \boldsymbol{E}\right) \cdot \boldsymbol{n}$$

Where $\boldsymbol{j}_i$, q_i, $\boldsymbol{E}$ represent the current density carried by charged species i, the electrical charge of species i, and the electric field. The letter μ_i denotes as the mobility of species inside the solution.

4.3 Result and discussion

The one-dimensional (1D) fluid model is used to delve into diffusion and chemical reactions of each chemical species in solution. The chemical species from the gas phase produced by APP Jet penetrated the PBS solution[240]. The 1D model was previously used for studying kinetic in an aqueous phase[97, 98]. Here, we assume

the solution is a NaCl with a constant pH of seven as a PBS-like solution. and supply some chemical species to study the reaction-transport mechanism of plasma irradiated PBS-like solution. Given the assumption of a uniform temperature distribution between the PBS solution and the surrounding gas, convective flow is considered negligible. Furthermore, the absence of charged species entering the solution implies a zero current density ($\boldsymbol{j}_i = 0$).

The first investigation simulated the reaction and transport of plasma-irradiated PBS with Ar, Ar/H_2O_2, Ar/Air, and Ar/O_2 gas feed, which we did with a zero-dimensional (global model) in previous studies [11]. During the last study, we did not consider the phenomenon of diffusion in liquids, so we assumed that the liquid conditions were homogeneous. Here we want to eliminate the assumption that the liquid state is homogeneous because the liquid is not homogeneous in reality. Understanding each chemical species reaction and transport mechanism inside the solution irradiated by plasma is very important. In research involving plasma for medical and biological purposes, it is necessary to know the reaction mechanism of each species inside the solution because each species has contacted the cell and has a biological effect.[240, 117, 230, 180]

Ar, Ar/H_2O, Ar/Air, and Ar/O_2 gas feed calculations into solution are shown in Fig. 4.2 with a 0.8 cm separation between the plasma jet tip and the solution (data from table 4.1). The figure displays the concentration profile for each species as a function of solution depth. More than 18 species are present at concentrations more than 5×10^{-8} mol/L; 6 of these are derived from the initial solution (Na^+, Cl^-, N_2, O_2, H^+, OH^-), 5 are directly injected from the gas (H_2O_2, O_2, NO, NO_2, HNO_2), and others are created by a chemical reaction occurring within the solution.

Our concern then focuses on the chemical species from the gas and the product of the chemical reaction inside the solution. H_2O_2 is the dominant species in Ar and Ar/H_2O gas feeds. However, NO_2^- and HOCl are the dominant species in Ar/Air and Ar/O_2. The difference in condition inside solution is caused by the gas phase species densities injected into the PBS-like solution. Table 3.1 shows the details of the gas phase densities injected into the solution from every gas feed. We can see that the densities of species, i.e., H_2O_2, are different. The highest to lowest densities come from Ar/H_2O. Ar, Ar/Air, and Ar/O_2. The amount of

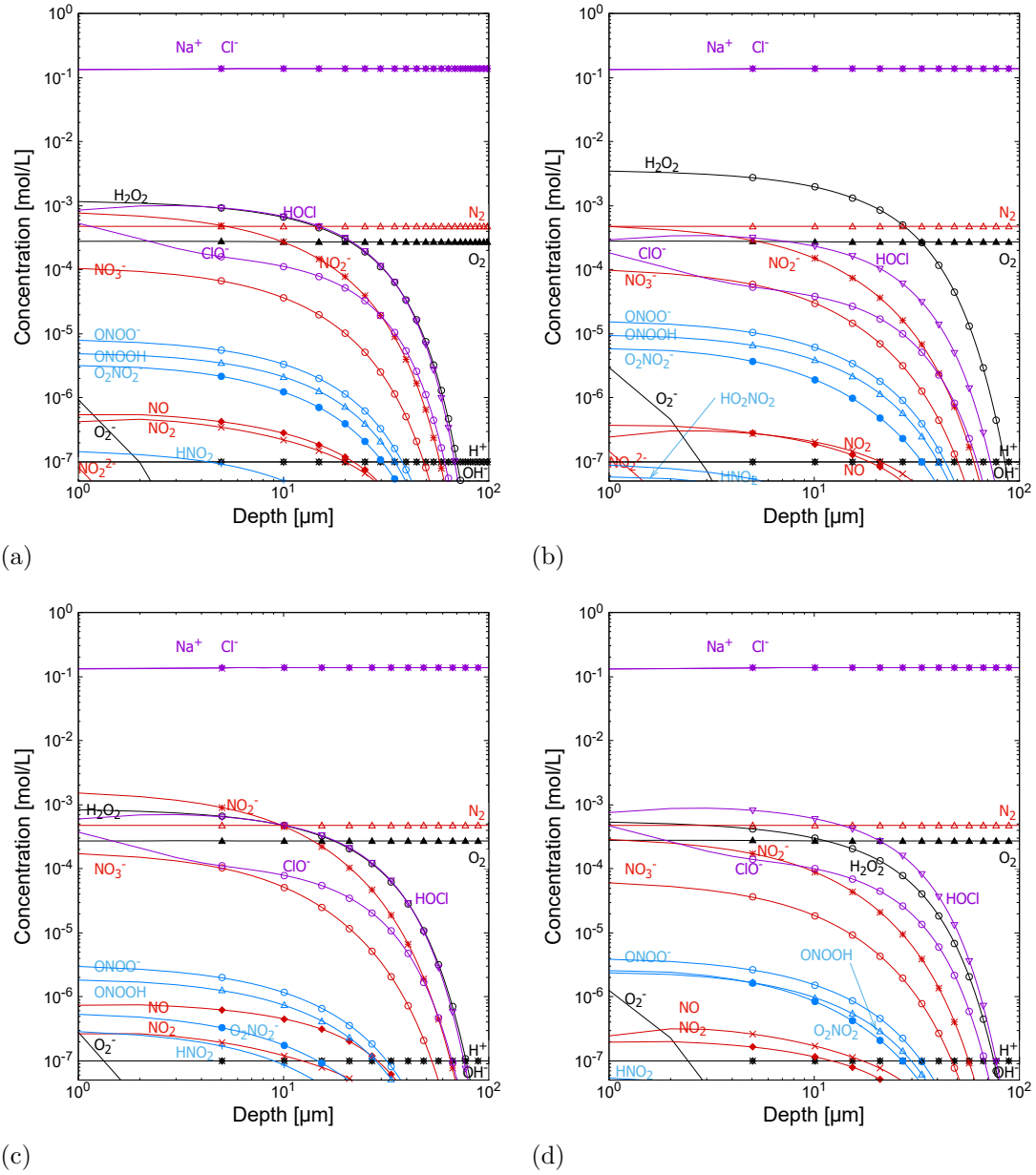

Figure 4.2: The concentration profiles of all chemical species are found in the PBS-like solution at plasma irradiation time equal to 0.1s. The distance from the plasma tip to the liquid is 0.8 cm. The vertical axis is the concentration in mol/L, and the horizontal axis is the depth of solution in μm. Both axes are on the log scale. The Figure from four different gas feed (a) Ar, (b) Ar/H_2O, (c) Ar/Air, and (d) Ar/O_2. Gas species correspond to table 4.1. For the sake of simplicity, there is no influx of ions or electrons from the gas phase is considered in the simulation.

gas is proportional to the concentration in the solution (Fig. 4.2). However, the concentration in the solution depends on the composition of the gas injected into the solution. Due to the many variables inside the solution, the system is nonlinear. So, it is difficult to predict the condition without calculating it carefully.

Figure 4.2 also provides details on the depths to which various species can penetrate. The five dominant species that can penetrate deeper layers of a solution are H_2O_2, HOCl, NO_2^-, ClO^-, and NO_3^-. From the five dominant species, H_2O_2 and HOCl can reach the deepest solution. It means that H_2O_2 and HOCl are stable species (less-reactive). The existence of H_2O_2 and another species in the solution is due to the diffusion and reaction of each species from the gas with the species in the solution. We will discuss the chemical reaction that produces or consumes the species in the next section.

Reactive species are indicated by their appearance on the surface only; their concentration immediately decreases drastically with the depth of the solution. O_2^- and NO_2^- are examples of reactive species. Both only appear near the surface of the solution. The area where various species appear (including reactive species) is called the reaction boundary layer (RBL). By the definition of RBL, we can consider an area of 10 μm as an RBL.

Production and loss of Hydrogen Peroxide

Once we identified the reactivity and location of each species, we focused on the production and consumption reactions of each species. Another important thing is to find the location of the reaction. Normally, the chemical reaction occurs in the near-surface layer, where gas species meet solution species.

In medicine, hydrogen peroxide (H_2O_2) has numerous therapeutic uses, including wound care, acne, and cancer skin therapy [170]. H2O2 is also potentially used for therapeutic purposes for vascular disorders, tissue regeneration, and treating brain ischemia. [175, 135]. Regarding the usefulness of H_2O_2, it is very essential to understand the reaction of H_2O_2 in PBS solution. [39].

H_2O_2 is the most dominant species in calculation of Ar and ArH_2O (figs. 4.2a and 4.2b) injection. The existence of high H_2O_2 concentrations comes from H_2O_2 gas and also from reactions from other species. Fig. 4.3 shows the production

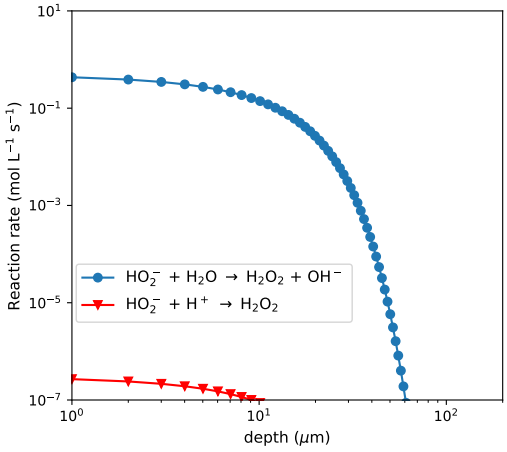

(a)

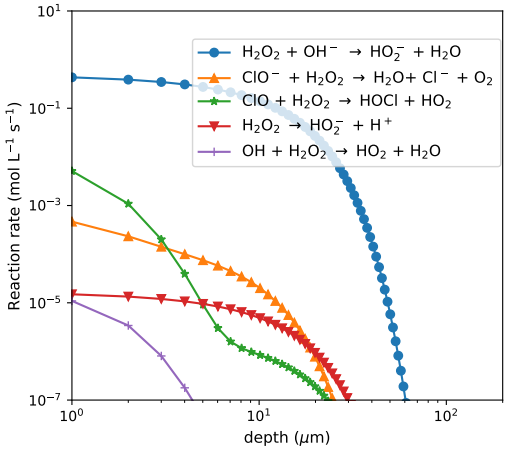

(b)

Figure 4.3: Production and loss rate of H_2O_2 inside PBS-like solution at time 0.1 s. The distance from the plasma tip to the solution is 0.8 cm. The vertical axis is the reaction rate in mol/L/s of H_2O_2, plotted on the log scale. The horizontal axis is the depth of the solution in a micrometer. Figure (a) is the production rate of H_2O_2 and (b) is the loss rate of H_2O_2. The data taken taken from Argon/O_2 1% (table 4.1).

(4.3a) and consumption (4.3b) of H_2O_2 by other species. The production of H_2O_2 comes from two chemical reactions:

$$HO_2^- + H_2O \longrightarrow H_2O_2 + OH^- \tag{4.2}$$

and

$$HO_2^- + H^+ \longrightarrow H_2O_2. \tag{4.3}$$

On the other hand, H_2O_2 consumption comes from five reactions:

$$H_2O_2 + OH^- \longrightarrow HO_2^- + H_2O \quad , \tag{4.4}$$

$$ClO^- + H_2O_2 \longrightarrow H_2O + Cl^- + O_2 \quad , \tag{4.5}$$

$$ClO + H_2O_2 \longrightarrow HOCl + HO_2 \quad , \tag{4.6}$$

$$H_2O_2 \longrightarrow HO_2^- + H^+ \quad , \tag{4.7}$$

$$OH + H_2O_2 \longrightarrow HO_2 + H_2O$$

Chemical reactions 4.2 and 4.4 are reverse reactions; both have the same reaction rate. So, we can ignore reactions 4.2 and 4.4. The production of H_2O_2 also comes from reaction number 4.3. However, there are four chemical reactions that result in H_2O_2 loss. If we compare the production and loss reactions of H_2O_2, we realize that the loss reaction is more dominant compared to the production reaction. However, the amount of H_2O_2 in the solution is high. We can understand that H_2O_2 in the solution mostly comes from the gas injection and then diffuses into the solution's bulk. Diffusion coefficient of H_2O_2 is 2.3×10^{-9} m^2s^{-1}.[59]

We do not show the gas injection in Fig. 4.3, because Fig. 4.3 only shows the chemical concentration inside the solution.

Production and lost of hypochlorite ClO^-

Hypochlorite anion (ClO^-) is one of the species with the 5^{th} highest concentration in a PBS-like solution. In the medicine, the hypochlorite anion (ClO^-) is an interesting chemical found in the human body. It is an essential component of our immune system, working as a powerful weapon against invading pathogens such as bacteria and viruses.[117, 57, 104] However, like a double-edged sword, unrestrained activity can cause damage to our own tissues. Understanding this

delicate equilibrium is essential for grasping the intricate relationship between hypochlorite and human health.[115, 244]

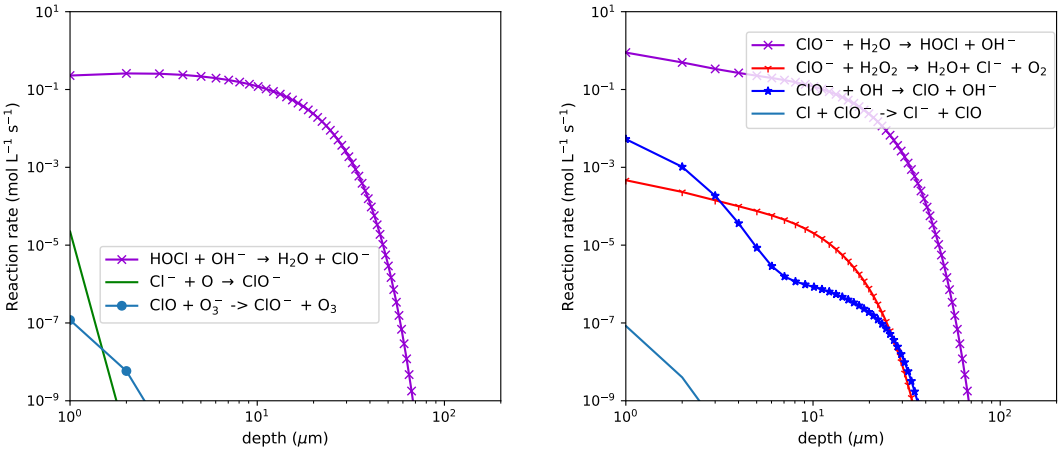

(a) (b)

Figure 4.4: Production and loss rate of ClO^- inside PBS-like solution at time 0.1 s. The distance from the plasma tip to the solution is 0.8 cm. The vertical axis is the reaction rate in mol $l^{-1}s^{-1}$ of ClO^-, plotted on the log scale. The horizontal axis is the depth of the solution in a micrometer. Figure (a) is the production rate of ClO^- and (b) is the loss rate of ClO^-. The gas-phase data taken from Argon/O_2 1% (table 4.1).

Investigating ClO^- in the solution, starting from tracing the chemical reaction to produce and lost of ClO^-. Figure 4.4 shows the reaction to produce ClO^- (4.4a) and the lost reaction of ClO^- (4.4b). The reaction producing ClO^- is the reaction of HOCl and OH^- by reaction

$$HOCl + OH^- \longrightarrow H_2O + ClO^- \quad . \tag{4.8}$$

This reaction is a reverse reaction with

$$ClO^- + H_2O \longrightarrow HOCl + OH^- \quad . \tag{4.9}$$

as shown in figure 4.4b. Another reaction to form ClO^- is the reaction of Cl^- and O via reaction

$$Cl^- + O \longrightarrow ClO^- \quad . \tag{4.10}$$

ClO and O_3^- are also species that produce ClO^- via reaction

$$ClO + O_3^- \longrightarrow ClO^- + O_3 \quad . \tag{4.11}$$

Reactions 4.10 and 4.11 are located in the reaction boundary layer (RBL), the area near the surface ($< 10\mu$m). The slope of reactions 4.10 and 4.11 is sharp, which means the reaction only occurs near the surface. Cl^- comes from the solution, and O comes from the plasma gas injection. Even though the ClO^- formation reaction is mostly in the RBL, in figure 4.2, it can be seen that the concentration of ClO^- in the bulk is quite large. This is suspected to be the presence of the diffusion of ClO^-, which is formed in the RBL and then diffuses into the solution.

The loss of ClO^- mainly because of reaction of ClO^- with H_2O_2 via reaction 4.5. Also reaction of ClO^- with OH via reaction

$$ClO^- + OH \longrightarrow ClO + OH^- \quad . \tag{4.12}$$

In the boundary, the rate of reaction 4.12 is higher compared to reaction 4.5. It happens because the concentration of OH is high. However, OH is highly reactive, so at the boundary, OH mostly reacts with other species to form new species. This is the reason the slope in reaction 4.12 is sharper compared to reaction 4.5.

H_2O_2 (in figure 4.2) is less reactive compared to OH, so that reaction 4.5(fig. 4.4b) has a gentle slope. Reaction 4.5 is the dominant reaction, consuming ClO^-; it will produce H_2O, Cl^-, and O_2. In our previous study, we referred to this process as the "chlorine monoxide cycle".[11].

Production and lost of chlorine monoxide ClO

ClO has various functions, including ozone depletion in atmospheric chemistry, oxidizing and inactivating pathogens, potential application in wastewater treatment, etc. [42, 243, 136].

Figure 4.5 shows the (a) production and (b) loss rates of ClO in the PBS-like solution exposed to the plasma under the conditions of figure 4.2d. It is seen that the dominant source of ClO is reaction 4.12 and its dominant loss mechanism is reaction 4.6.

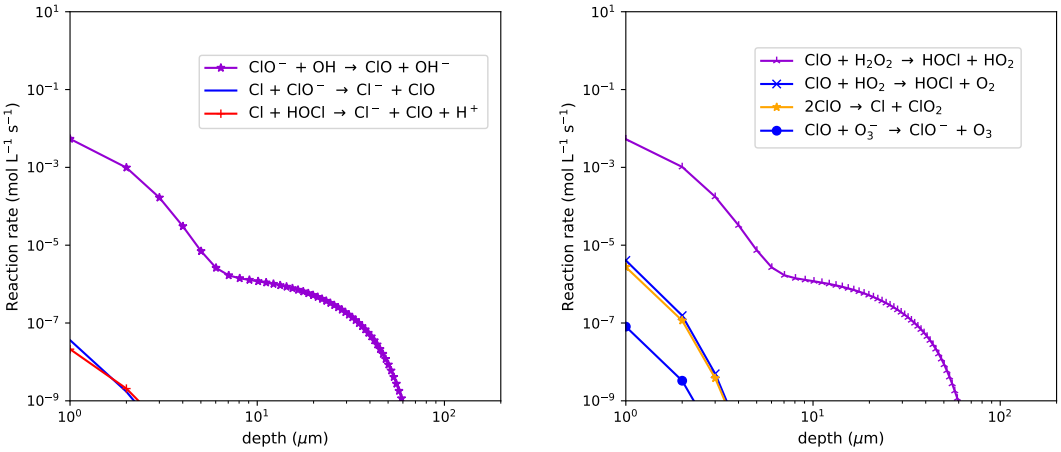

(a) (b)

Figure 4.5: Production and loss rate of ClO inside PBS-like solution at time 0.1 s. The distance from the plasma tip to the solution is 0.8 cm. The vertical axis is the reaction rate in mol $l^{-1}s^{-1}$ of ClO, plotted on the log scale. The horizontal axis is the depth of the solution in a micrometer. Figure (a) is the production rate of ClO and (b) is the loss rate of ClO. The gas-phase data taken taken from Argon/O_2 1% (table 4.1).

Reaction 4.12 is the most dominant production reaction of ClO, originating from ClO^- and OH. From Table 3.1, we know that OH comes from the gas formed by the plasma, while ClO^- is a species inside the liquid formed by reaction 4.10. OH is a highly reactive species, so it can only be found on a liquid surface. This causes the reaction of ClO^- with OH to only occur at the surface (RBL) (see Figure 4.5a).

Figure 4.5b shows that the magnitude of the loss rate is equal to the magnitude of the ClO formation rate. Therefore, after being formed, ClO immediately reacts with H_2O_2 to form HOCl and HO_2 via reaction 4.6. This is why ClO is not detected in Figure 4.2.

Another chemical reaction that forms ClO is $Cl + ClO^- \longrightarrow Cl^- + ClO$. This reaction only exchanges electrons from ClO^- to Cl. Therefore, ClO^- releases electrons and becomes ClO. And Cl captures electrons and becomes Cl^-. The rate of this reaction is small compared to reaction number 4.12. Therefore, the

impact of ClO production from this reaction is not significant. Several ClO forming reactions shown in Figure 4.5a are also very small. However, what we can observe from the four reactions is the steep slope. This indicates that the reaction location occurs in the RBL area.

Loss mechanisms and places of H_2O_2 in the presence of Cl^-

Based on the above discussion, we can now summarize the consumption of H_2O_2 due to the presence of Cl^- in the solution and the location of the reactions that occur. Initially, Cl^- reacts with oxygen radicals (O) from the plasma that penetrate the solution, generating ClO^- via reaction 4.10. ClO^- then reacts with H_2O_2 via reaction 4.5 to form Cl^-, water, and O_2. This reaction becomes a cycle while the Cl^- formed, it will react again with O from the gas.

ClO^- also reacts with OH from the plasma gas via reaction 4.12. The reaction of ClO^- with OH forms ClO, which immediately reacts with H_2O_2. OH is highly reactive, so the reaction of OH with ClO^- only occurs at the RBL. This is why the reaction of ClO with H_2O_2 also mostly occurs at the RBL.

Figure 4.6 shows the production (a) and loss (b) reactions of OH. Both production and loss reactions occur at the RBL. The most dominant production reaction is reaction

$$HOCl^- \rightleftharpoons OH + Cl^- \quad , \tag{4.13}$$

which is a reverse reaction, so it can be ignored. Therefore, the most dominant formation reaction is the reaction of HOCl and ${O_2}^-$ via reaction

$$HOCl + {O_2}^- \longrightarrow Cl^- + O_2 + OH \quad . \tag{4.14}$$

Reaction 4.14 produces Cl^-, O_2, and OH. This reaction is a component of the second cycle. The OH that is produced will react with ClO^- to form ClO via reaction 4.12.

The reaction of ClO with H_2O_2 via reaction 4.6 produces HOCl and HO_2. Since HO_2 and ${O_2}^-$ are conjugate acid and base pairs, the presence of HO_2 also leads to the appearance of ${O_2}^-$ in the solution.

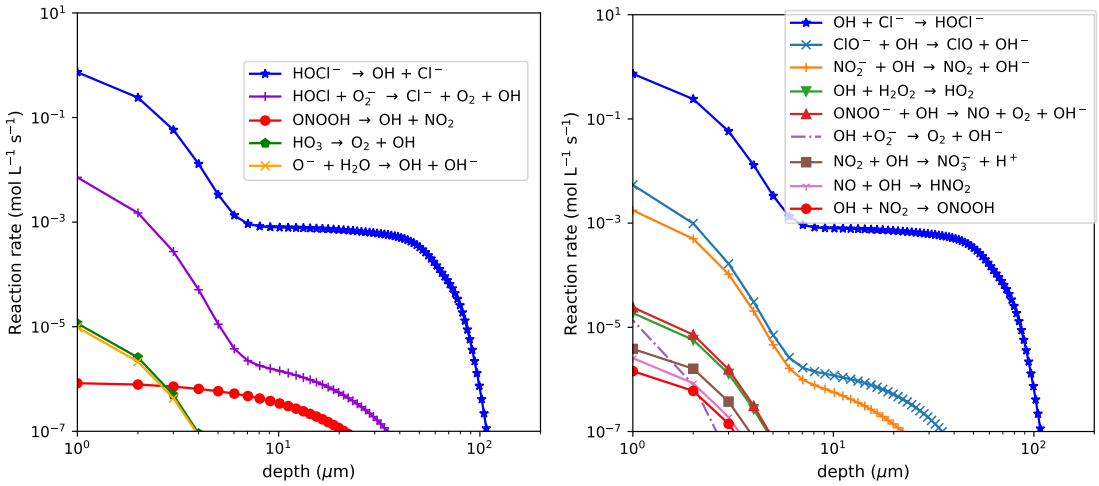

(a) (b)

Figure 4.6: Production and loss rate of OH inside PBS-like solution at time 0.1 s. The distance from the plasma tip to the solution is 0.8 cm. The vertical axis is the reaction rate in mol $l^{-1}s^{-1}$ of OH, plotted on the log scale. The horizontal axis is the depth of the solution in a micrometer. Figure (a) is the production rate of OH and (b) is the loss rate of OH. The data taken taken from Argon/O_2 1% (table 4.1).

Figure 4.7 shows the production (a) and loss (b) reactions of O_2^-. O_2^- production is mainly derived from HO_2 via reactions

$$HO_2 \longrightarrow O_2^- + H^+ \quad , \tag{4.15}$$

and $HO_2 + OH^- \longrightarrow O_2^- + H_2O$. These reactions demonstrate that O_2^- is the conjugate acid of HO_2. This is because HO_2 requires OH^- or produces H^+ along with the production of O_2^-.

Once O_2^- is produced, it reacts with HOCl via reaction 4.14. Other chemical reactions that consume O_2^- are NOx via reactions $O_2^- + NO \longrightarrow$ ONOO and $O_2^- + NO_2 \longrightarrow O_2NO_2^-$. If O_2^- encounters H^+, it will react and produce HO_2 via reaction

$$O_2^- + H^+ \longrightarrow HO_2 \quad . \tag{4.16}$$

This means that reactions 4.15 and 4.16 are reverse reactions. However, in terms of the magnitude of the reaction rate, reaction 4.15 is larger. This means that

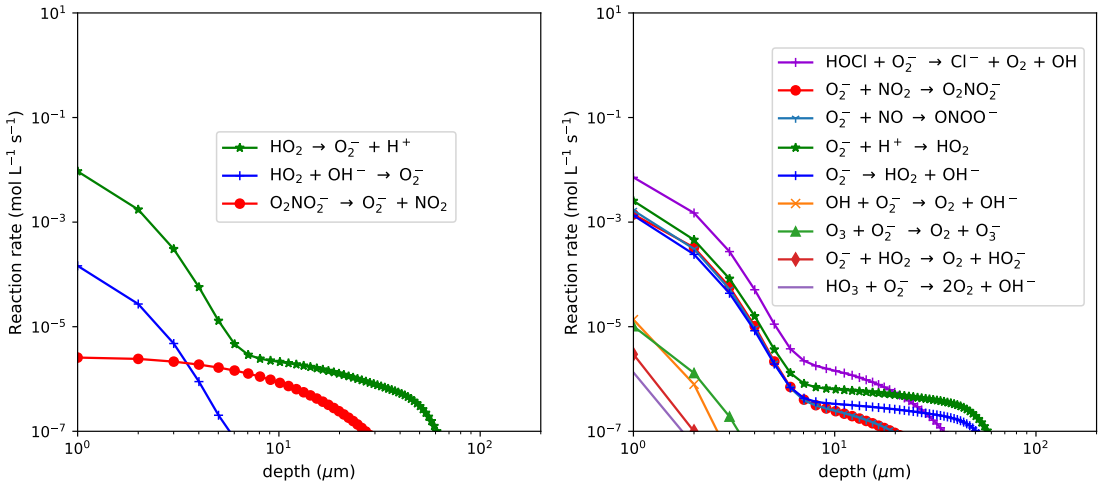

(a) (b)

Figure 4.7: Production and loss rate of O_2^- inside PBS-like solution at time 0.1 s. The distance from the plasma tip to the solution is 0.8 cm. The vertical axis is the reaction rate in mol $l^{-1}s^{-1}$ of O_2^-, plotted on the log scale. The horizontal axis is the depth of the solution in a micrometer. Figure (a) is the production rate of O_2^- and (b) is the loss rate of O_2^-. The gas-phase data taken from Argon/O_2 1% (table 3.1).

reaction 4.15 is more likely to occur.

Comparison with the Global model

Previous studies have shown that the calculation results are in good agreement with experimental data.[11] However, a direct comparison of the calculation results in this study with experimental data is not possible due to the significant difference in time scale. In this study, we can only calculate up to a time interval of 0.1 s, while in the experiments, the measurements were performed for 60 and 360 seconds.[240] Therefore, all we can do is compare the global model (0D) calculation results with the 1-dimensional (1D) calculation results at the same time, which is 0.1 s.

Figure 4.8 shows the results of the 0D (a) and 1D (b) calculations showing the five dominant species present in the PBS solution. Curve (a) is taken from previous research [11] and is only taken up to 0.1 s to match the results of the 1D calculation.

To quantify the overall decrease and increase in each species concentration in the model PBS solution, the volume-averaged concentration of the i-th species is evaluated as

$$\bar{n}_i(t) = \frac{S_{\text{in}}}{V} \int_0^L n_i(x,t)\, \mathrm{d}x\,, \tag{4.17}$$

where $n_i(x,t)$ represents the concentration profile of the i species at time t obtained from Eq. (4.1). , Here S_{in}, V and L denote the surface area where the solution is exposed to the plasma, the volume of the solution, and the depth of the solution in the container, respectively. As discussed in [11], we assume the plasma jet cross section S_{in} is much smaller than the solution surface area S_{out}, which is defined as $L = V/S_{\text{out}}$. To be consistent with the assumption of the global model in [11], we set $S_{\text{in}} = 0.1$ cm^2, $V = 3$ ml, $L = 0.3$ cm, and $S_{\text{out}} = 10$ cm^2.

This results in a curve that is comparable to the 0D calculation results.

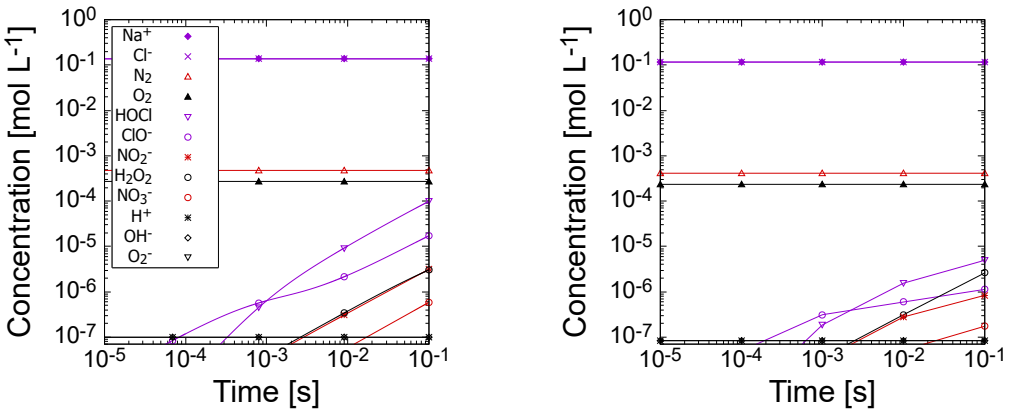

(a) (b)

Figure 4.8: Concentration profiles of the five dominant species in a PBS-like solution. Figure (a) from the 0D calculation and figure (b) from the 1D calculation. The data are taken up to a time of 0.1 s. The data are presented on a logarithmic scale. The vertical axis is the concentration (mol L^{-1}) and the horizontal axis is the time (s). The data taken from Ar/O2 (table 4.1).

Figure 4.8 is derived from the gas species in column Ar/O_2 listed in table 4.1. It was then calculated using 0D to produce the concentration of each species in the PBS solution, as shown in Figure 4.8a. The same data was calculated using 1D and produced the concentration of species as a function of depth, as shown in

Figure 4.2d. The 1D results in Figure 4.2d were then integrated using Equation 4.17 and produced the concentration of species at a time of 10^{-1} s in Figure 4.8b. To obtain data at times of 10^{-2}, 10^{-3}, and so on, the 1D calculation data was taken at those times. The integration results were then plotted (Figure 4.8b) to produce a graph of concentration as a function of time. This allowed fig 4.8b to be compared to fig 4.8a.

Figures 4.8a and 4.8b are used to confirm the results of the 1D calculation with the results of the 0D calculation for 0.1 s. Both figures show the five dominant species: HOCl, ClO^-, H_2O_2, $NO_2{}^-$, and $NO_3{}^-$. From both figures, it can be seen that at a time of 10^{-4} s, ClO^- is formed and becomes the dominant species. Thereafter, HOCl, which is the conjugate acid of ClO^-, is formed and becomes the most dominant species. The concentrations of the two species are not exactly the same in figures 4.8a and 4.8b, but the trend shown is the same.

H_2O_2 in both figures has almost the same concentration and the same trend. H_2O_2 starts to form in the solution at a time of 2×10^{-3} with a concentration of 10^{-7} mol/L, which is consistent between the two figures. At a time of 10^-2, the concentration of H_2O_2 increases to 2×10^{-7} mol/L. Then, the concentration of H_2O_2 increases again to 2×10^{-6} mol/L at a time of 0.1 s. The results of the H_2O_2 calculation from 0D and 1D have high consistency. Therefore, we compared the results of the H_2O_2 calculation for four different gases at a time of 0.1 s.

Figure 4.9 presents a comparison of H_2O_2 concentration between 0D and 1D calculations after integration at 0.1 s. The H_2O_2 in the PBS solution originates from four different plasma gas sources: Ar, Ar/Air, Ar/O_2, and Ar/H_2O. The graph shows that the 0D-calculated H_2O_2 consistently exhibits a higher concentration than the 1D counterpart. This discrepancy arises because the 0D calculation assumes a homogeneous solution, facilitating faster reaction rates. In contrast, the 1D approach incorporates diffusion within the solution, allowing species to be mobilized into the solution's depth alongside reacting.

Calculation of O and H_2O_2

The preceding discussion (sub sec. 4.3) established that the consumption of H_2O_2 is primarily driven by ClO^-, both directly and following its conversion to ClO. ClO^-

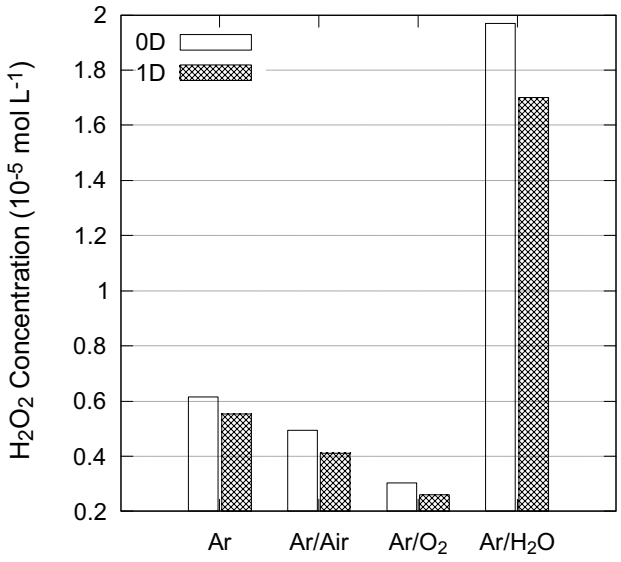

Figure 4.9: H_2O_2 concentration inside the PBS-like solution from four different gas feeds (Ar, Ar/Air, Ar/O_2 and Ar/H_2O) 0.1 s after plasma irradiation. The vertical axis represents H_2O_2 concentrations in mol L^{-1}, and the horizontal axis represents gas feeds.The white bar curve represents the data from the 0D calculation, while the black striped bar curve represents the data from the 1D calculation.

is known to originate from Cl^- and O via reaction 4.10, where Cl^- is present in the PBS solution and O stems from the plasma gas entering the solution. Leveraging this knowledge, we devised a simplified calculation involving only O and H_2O_2, hereinafter referred to as O–H_2O_2 Calc.

The O–H_2O_2 Calc. employs three different ratios of O and H_2O_2 concentrations: 0:1, 1:1, and 10:1. The H_2O_2 concentration is held constant at a density of 1.36×10^{14} cm^{-3}, while the O density is varied across 0, 1.36×10^{14}, and 1.36×10^{15} cm^{-3}. The initial solution conditions and calculation parameters remain identical to those of the previous calculation. The sole distinction lies in the simplification of the gas species entering the solution, reducing them from 13 to 2.

Figure 4.10 presents the depth profiles of chemical species at $t = 0.1$ s, i.e., after 0.1 s exposure of the solution surface to gas-phase H_2O_2 molecules and O radicals with $[H_2O_2(g)] = 1.36 \times 10^{14}$ cm^{-3} and various O(g) densities at room temperature. In (a), where the solution was exposed only to H_2O_2(g), only H_2O_2

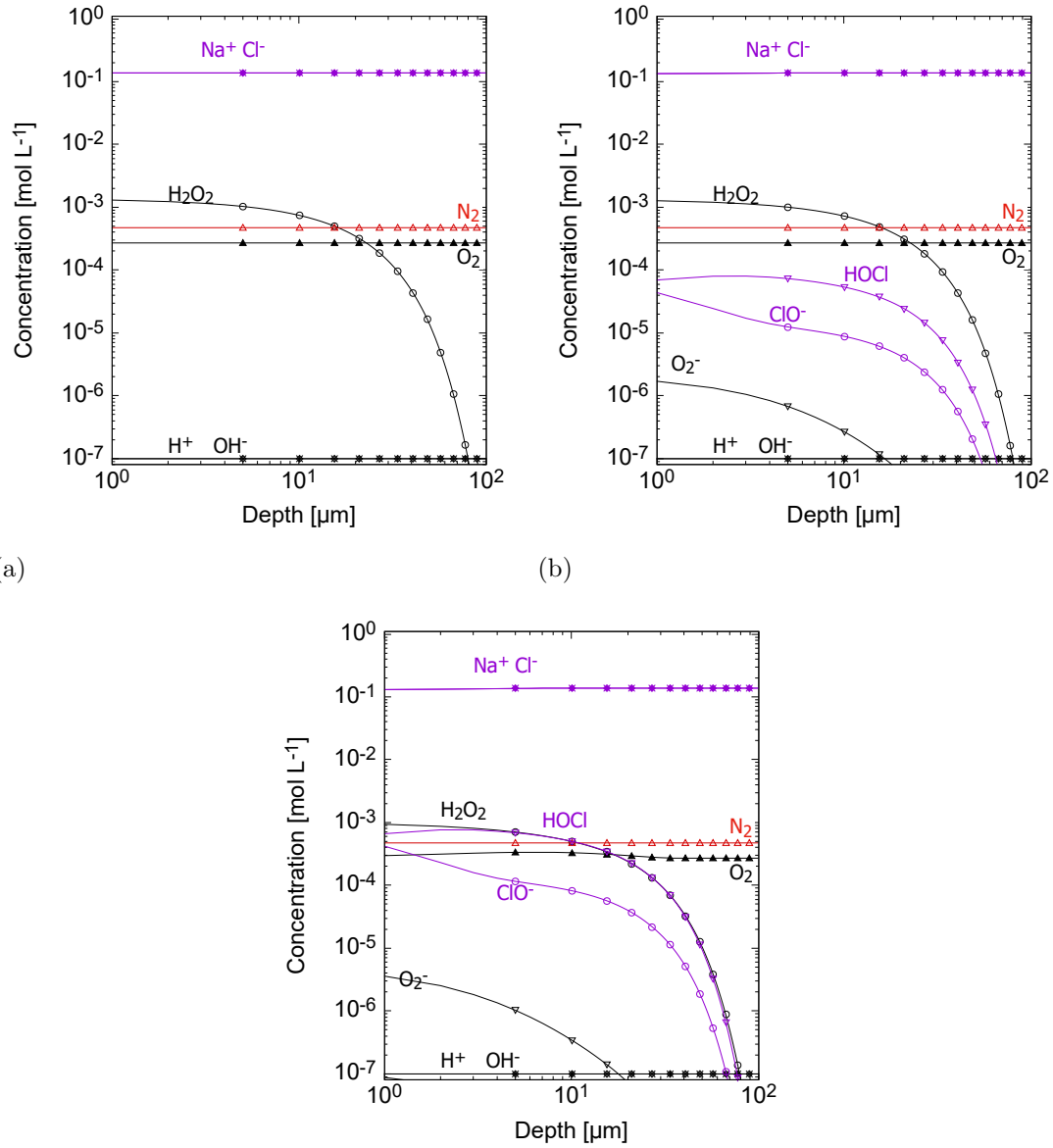

Figure 4.10: Concentration profiles of chemical species in the model PBS solution as functions of depth at $t = 0.1$ s, obtained from the numerical simulations. The origin of the depth is the location of the solution surface. The concentration ratios of the gas-phase species $[O_{(g)}]/[H_2O_{2(g)}] = 0$ (a), 1 (b), and 10 (c). The $H_2O_{2(g)}$ density is held constant at 1.36×10^{14} cm^{-3} in all cases here.

is detected in the solution. The H_2O_2 concentration at the solution surface is approximately 1.1×10^{-3} mol l^{-1}. The concentration decreases with depth as H_2O_2 diffuses into the solution bulk.

In the presence of O radicals in the gas phase, it is seen that ClO^- and HOCl are generated in the PBS solution. It is seen in Fig. 4.10(b), where the gas-phase densities of both $O_{(g)}$ and $H_2O_{2(g)}$ are the same, the concentration of HOCl is still much lower than that of H_2O_2 at $t = 0.1$ s. As seen in Fig. 4.10(c), when the gas-phase density of $O_{(g)}$ is 10 times larger than that of $H_2O_{2(g)}$, the concentration of HOCl is close to that of H_2O_2 at $t = 0.1$ s. It is also seen that the concentration of H_2O_2 in (c) is slightly lower than that in (b), indicating the decomposition of H_2O_2 in the presence of HOCl and ClO^-.

Because of the high computational cost, the 1D simulations in this study were performed only up to $t = 0.1$s, as opposed to $t = 60$ s of the global model in Ref. [11]. Nevertheless, the 1D simulation showed the diffusion of stable chemical species into the bulk of the solution far beyond the RBL.

Comparison between 1D and global simulations

Figure 4.11 shows the concentrations of H_2O_2 and ClO^- averaged over the volume V at $t = 0.1$ s obtained from the 1D simulations of this study (a) and the global simulations of [11] (b) under the same conditions as those of Fig. 4.10. The main difference between the 1D and global models arises from the difference in the local concentrations of incident species. The liquid-phase diffusion is slow, so, at $t = 0.1$ s, the incident species and the newly generated chemical species in the solution were still confined in a thin layer with a thickness of a couple of μm below the solution surface in the 1D case, as seen in Fig. 4.10. In the global simulations, the incident species are placed over the entire volume V with a uniform distribution. Therefore, at $t = 0.1$ s, the concentrations of chemical species in the region where they exist are much higher in the 1D simulation than those in the corresponding global simulation.

As seen in Fig. 4.11, the initial volume-averaged concentrations of H_2O_2 in the absence of incident O radicals (i.e., $[O(g)] = 0$) are nearly the same for the 1D and global simulations. Although H_2O_2 is stable, it can also decompose slowly even in

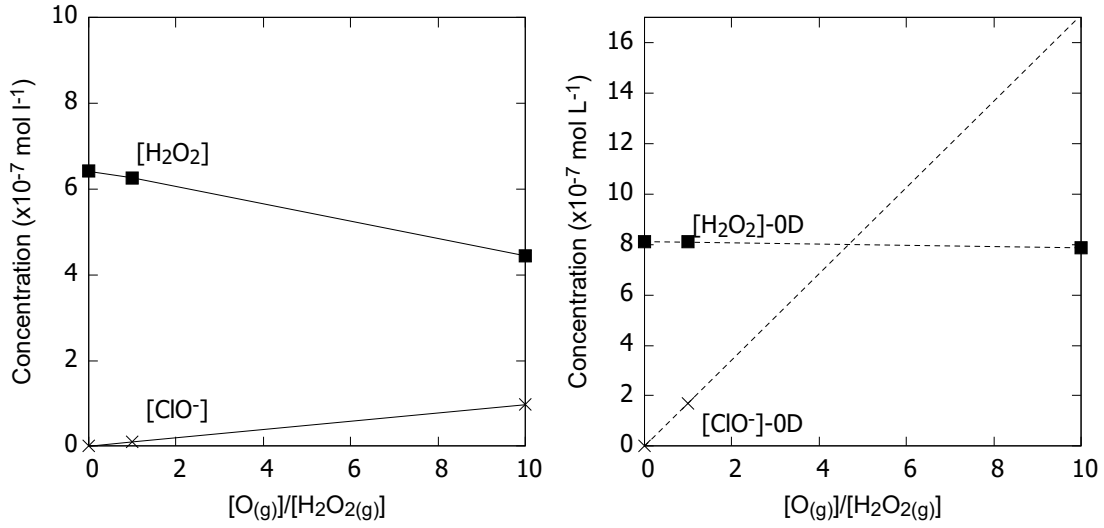

(a) (b)

Figure 4.11: Volume-averaged concentrations of H_2O_2 and ClO^- at $t = 0.1$ s as functions of the density ratio of $O_{(g)}$ to $H_2O_{2(g)}$ in the gas phase obtained from the 1D simulations of this study (a) and the global simulations of [11] (b) under the same conditions as those of Fig. 4.10. Because the diffusion is slow, the local concentrations of chemical species (i.e., concentrations where they exist) are still high at $t = 0.1$ s, and, therefore, the decomposition rates of H_2O_2 are much higher than those in the global simulations, in which the incident species are distributed over the entire solution volume instantly.

the absence of ClO^-, the high local concentration of H_2O_2 accounts for the slightly lower value of $[H_2O_2]$ in the 1D simulations at $[O(g)] = 0$.

The high local concentrations also increase other reaction rates, including the rates of decomposition of H_2O_2 by Cl-containing reactive species generated by incident O radicals, as seen in Figure 4.11(a). Accordingly, the consumption of ClO^- is also fast, so the volume-averaged concentration of ClO is lower in the 1D simulation than that in the global simulation at $t = 0.1$ s. As demonstrated in [11], it takes about 60 s for the global simulation to exhibit a significant reduction of the concentration of H_2O_2 under the same reactive gas-exposure conditions.

Reaction pathways

We now aim to identify the key reactions leading to the decomposition of H_2O_2. Figure 4.12 shows the production and loss reaction rates of H_2O_2 as functions of the depth at $t = 0.1$ s, i.e., after 0.1 s exposure to O (g) and H_2O_2(g), corresponding to the case of Fig. 4.10(b), where the gas-phase densities of O (g) and H_2O_2(g) are both 1.36×10^{14} cm^{-3}. The reaction that has the highest rate for the production of H_2O_2 in the entire domain of the solution is R_O057 of [98], i.e.,

$$HO_2^- + H_2O \longrightarrow H_2O_2 + OH^- \ ,$$

which is, however, balanced by its reverse reaction (R_O057 of [98]), i.e.,

$$H_2O_2 + OH^- \longrightarrow HO_2^- + H_2O \ ,$$

so they do not contribute to the net production or loss of H_2O_2. Figure 4.12(a) shows that the H_2O_2 production reaction that has the second highest rate has, however, very low reaction rates and, moreover, its reverse reaction has much higher rates throughout the depth where the diffusion occurs, indicating that H_2O_2 is not generated by this reaction. Therefore, H_2O_2 exists in the solution simply because it is transported from the gas phase and dissolves in the solution.

Figure 4.12(b) shows that the reaction causing the dominant net loss of H_2O_2, i.e., the reaction not balanced with its own reverse reaction, is Reaction (4.6), despite the fact that no ClO is observed in Fig. 4.10(b). In other words, ClO exists only as a chemical intermediate, but it is the dominant cause of H_2O_2 decomposition. As observed in Fig. 4(b), the loss rate by ClO, i.e., Reaction (4.6), is higher than that by ClO^-, i.e., Reaction (4.5), throughout the depth. In a deeper region, the self-decomposition of H_2O_2 is seen to dominate. However, the net loss of H_2O_2 by the self-decomposition throughout the volume or depth is much smaller than that by Reaction (4.6).

The next investigation aims to identify the key reactions governing the O$-H_2O_2$ calculation. These reactions are then compared with the important reactions in the calculation presented in Fig. 4.2. The first reaction of interest is the production and consumption of H_2O_2. Figure 4.12a shows that there are two H_2O_2 production reactions in the solution, namely reactions 4.2 and 4.3. Both reactions

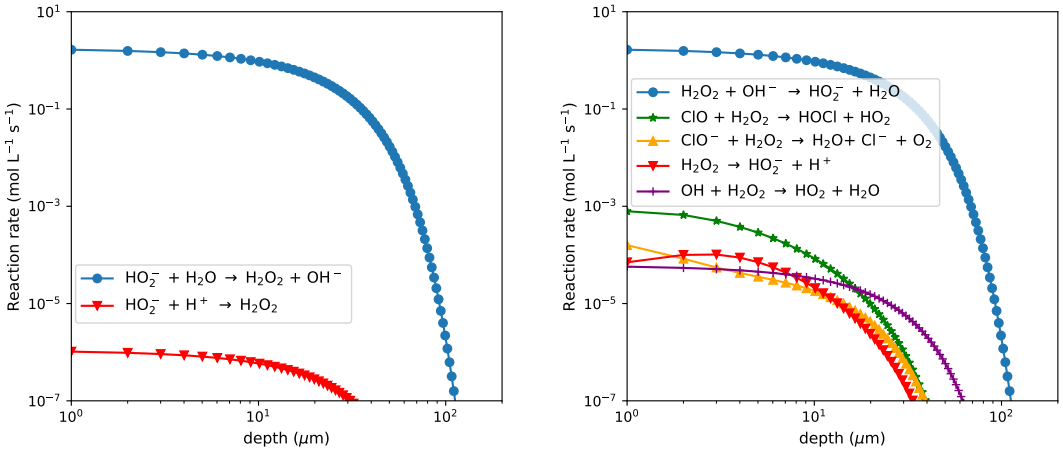

(a) (b)

Figure 4.12: Production (a) and loss (b) rate profiles of H_2O_2 in the model PBS solution at $t = 0.1$ s, corresponding to the case of Fig. 4.10(b), where the gas-phase densities of O (g) and H_2O_2(g) are both 1.36×10^{14} cm^{-3}.

are reversible, with reverse reactions 4.4 and 4.7 depicted in Fig 4.12b. Figure 4.12b depicts the H_2O_2 consumption reactions, with the most dominant reaction being that of H_2O_2 with OH^- via reaction 4.4. However, reaction 4.4 is reversible and hence is neglected. Two reactions involving chlorine are identified, namely reactions 4.5 and 4.6. These reactions are the most dominant in consuming H_2O_2.

The next question is how ClO^- and ClO are generated in the PBS solution. Figure 4.13 shows the production and loss rates of ClO^- and ClO. It is seen in Fig. 4.13(a) that Reaction (4.10) produces ClO^- only in the RBL. Then the generated ClO^- diffuses into the bulk of the solution, forming chemical equilibrium between the following reactions ($R_{Cl}031$ of [98]);

$$HOCl + OH^- \longrightarrow ClO^- + H_2O \ , \tag{4.18}$$

$$ClO^- + H_2O \longrightarrow HOCl + OH^- \ . \tag{4.19}$$

Near the surface, these two reactions are not balanced and the loss rate of ClO^- by Reaction (4.9) is higher than the production rate by Reaction (4.8) to balance with the production of ClO^- by Reaction (4.10). It is also seen that a small percentage of ClO^- is consumed to produce ClO through Reaction (4.12).

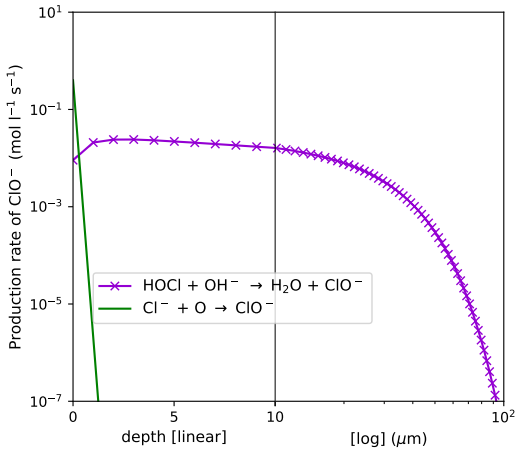

(a)

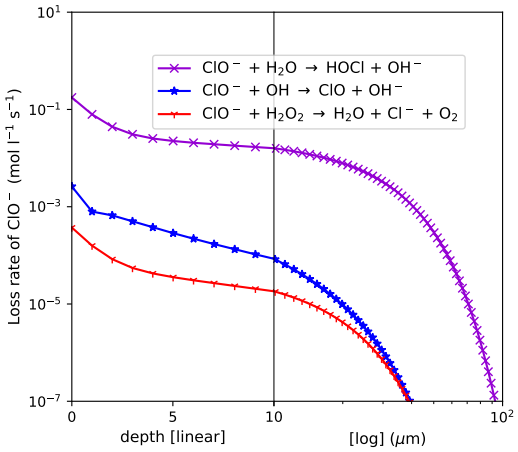

(b)

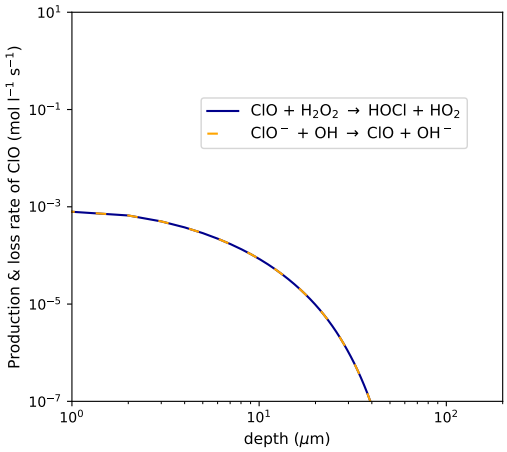

(c)

Figure 4.13: Production (a) and loss (b) rate profiles of ClO^- and those of ClO (c) in the model PBS solution at $t = 0.1$ s, corresponding to the case of Fig. 4.10(b), where the gas-phase densities of O(g) and H_2O_2(g) are both 1.36×10^{14} cm^{-3}. It should be noted that the horizontal axes of (a) and (b) are on a linear scale for depth $0 - 10\mu m$ and on a logarithmic scale for depth larger than $10\mu m$.

Figure 4.13(c) shows the production rate of ClO by Reaction (4.12) is completely balanced with its loss rate by Reaction (4.6), which is the loss rate of H_2O_2 by the reaction of ClO. This exact balance explains the absence of ClO in Fig. 4.10.

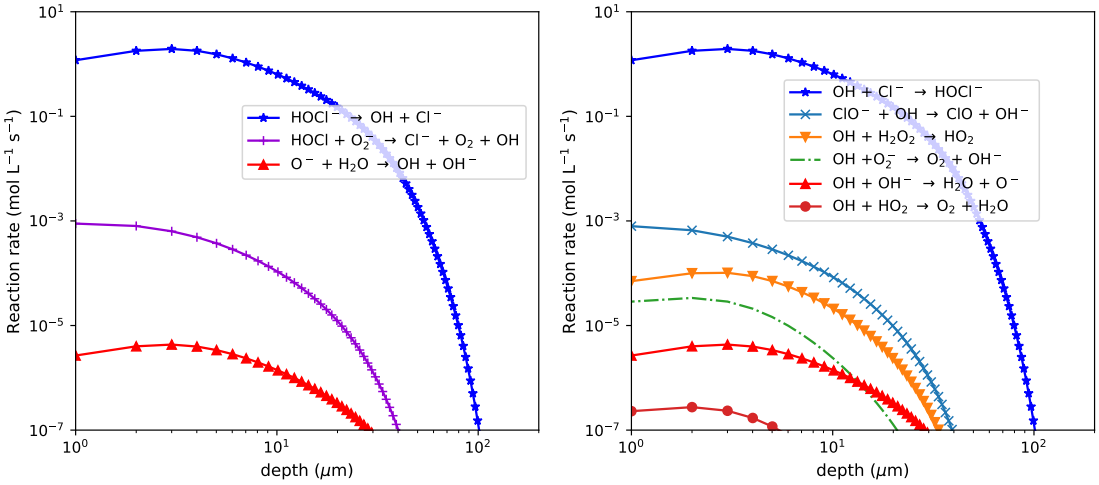

(a) (b)

Figure 4.14: Production (a) and loss (b) rate profiles of OH in the model PBS solution at $t = 0.1$ s, corresponding to the case of Fig. 4.10(b), where the gas-phase densities of O(g) and H_2O_2(g) are both 1.36×10^{14} cm^{-3}.

Now that the production of ClO requires the presence of OH, we examine the production and loss rates of OH, which are given in Fig. 4.14. It is shown that the dominant production and loss of OH occurs through the following reactions ($R_{Cl}058$) in chemical equilibrium ;

$$\mathrm{HOCl^-} \rightleftharpoons \mathrm{OH + Cl^-} \ . \tag{4.20}$$

Because these two reactions are well balanced throughout the depth where HOCl and ClO^- diffuse, OH does not appear in Fig. 4.10. However, a small percentage of OH produced in this reactions can initiate Reaction (4.12) even in the bulk of the solution as HOCl and ClO^- diffuse.

Figure 4.14(a) shows that, therefore, the net production reaction of OH that has the highest rate is Reaction (4.14), which has the same rate profile as Reaction (4.12). It means that OH radicals produced by Reaction (4.14) are all consumed

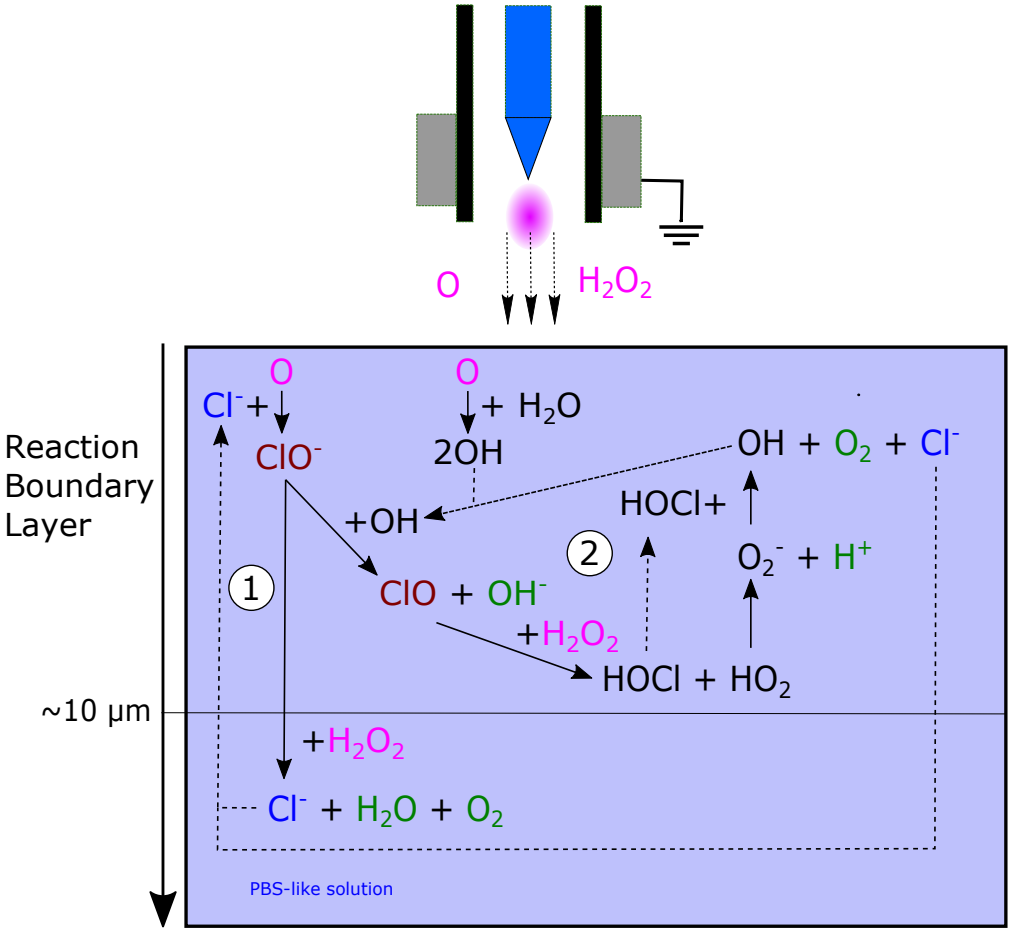

Figure 4.15: The dominant reaction pathways decomposition of H_2O_2 and depth profile chemical species inside PBS-like solution. The reactive species such as O, ClO and OH only occur in the reactive boundary layer (RBL). Only stable chemical species can going to the deeper of the solution (bulk solution). O have an important role in the

to produce ClO. In this way, a new ClO cycle to decompose H_2O_2 starts from Reaction (4.12) after Reaction (4.14) occurs. It should be noted that the presence of hydroperoxyl radicals (HO_2) generated by Reaction (4.6) indicate the presence of superoxide anion radicals O_2^- via Reaction (4.15).

Figure 4.15 summarizes the main reaction pathways for H_2O_2 and O injected into a PBS-like solution. When H_2O_2 and O gas enter the solution, H_2O_2, being a non-reactive chemical species, can diffuse deeply into the solution. As shown,

H_2O_2 (in purple) can penetrate beyond 10 μm. On the other hand, the highly reactive O remains in the RBL and immediately reacts with species present in the solution, generating other species.

Similar to our previous study[11], this research also identified two important reactions that consume H_2O_2: the reaction of H_2O_2 with ClO^- via reaction 4.5 and the reaction of H_2O_2 with ClO via reaction 4.6. The first reaction, referred to as cycle ①, involves the reaction of H_2O_2 with ClO^-. ClO^- originates from the reaction of Cl^- from within the solution with O supplied by the plasma via reaction 4.10. The reaction of ClO^- with H_2O_2 produces Cl^-, H_2O, and O_2. Cl^- enters a cycle where it reacts again with O.

Cycle ② begins with the reaction of ClO^- with OH via reaction 4.12, which generates ClO and OH^-. Subsequently, the formed ClO immediately reacts with H_2O_2 via reaction 4.6, producing HOCl and HO_2. HO_2 decomposes into $O_2{}^-$ and H^+. $O_2{}^-$ reacts with HOCl via reaction 4.14 to form OH, O_2, and Cl^-. The formed OH reacts again with ClO^- to form ClO. This reaction cycle continues until either H_2O_2 or OH is depleted. The presence of OH in this cycle initially from the surface, where the reaction of O supplied from the plasma with H_2O water via reaction $O + H_2O \longrightarrow 2\,OH$ generates 2 OH. However, this reaction only occurs at the surface since O is highly reactive.

We refer to the two reaction cycles that consume H_2O_2 as the 'chlorine monoxide cycle', where ClO acts as an intermediate species that facilitates H_2O_2 consumption by ClO^-. The chlorine monoxide cycle, through either cycle ① or ②, produces water and O_2. In cycle ①, water and O_2 are formed directly via reaction 4.5. In cycle ②, O_2 is formed via reaction 4.14, and H_2O is formed from OH^- generated by reaction 4.12 and H^+ generated by reaction 4.15.

However, these cycles are not easily discernible experimentally due to the rapid reaction times and the presence of numerous species that appear and disappear during the reactions. This is the case with ClO, which exists solely as an intermediate in ClO-mediated H_2O_2 consumption. Its presence also depends on the availability of OH in the solution, which is a highly reactive species that readily reacts to form other species.

The results of this study are more accurate than those of previous research[11]. This study allows us to determine the depth at which important reactions take

place. In contrast, previous studies assumed that the liquid was homogeneous due to its rapid mixing, and therefore considered reactions to occur in all layers. However, this study reveals that cycle ① occurs throughout the solution layer, while cycle ② is limited to the RBL.

Comparative analysis reveals that 0D calculations provide satisfactory outcomes for predominant chemical species like H_2O_2. The computational efficiency of 0D models makes them well-suited for preliminary investigations involving extended irradiation periods.[11] Nevertheless, for applications demanding high precision, 1D calculations offer a more suitable approach.

4.4 Conclusions

A one-dimensional reaction transport simulation was employed in this study to identify the dominant chemical reactions in a PBS-like solution irradiated by APPs. Specifically, we are interested in the reaction pathways of H_2O_2 consumption by Cl^--containing liquid irradiated by plasma. In this simulation, we assumed that the gas species formed by plasma irradiation, taken from previous work by Wende et al.,[240] are supplied into the surface of the PBS-like solution, and the results of this calculation are compared with our previous study[11]. The results of this calculation are in good agreement with previous calculations[11] in terms of species concentration and reaction pathways, especially the H_2O_2 consumption pathway in the PBS-like solution. This study reinforces previous findings that H_2O_2 consumption in the solution depends on the amount of O supplied by the plasma. O will react with Cl^- to form ClO^-. ClO^- will react directly with H_2O_2 and through its intermediate species, ClO. The final products of these reactions are water (H_2O) and oxygen (O_2).

In Wende's experiment[240], the possibility of H_2O_2 decomposition by ClO^- was suggested as reaction 4.5. In our previous study[11], we found that H_2O_2 decomposition could also occur through the chlorine monoxide cycle. In this study, we reinforce that H_2O_2 decomposition can occur through either the reaction of H_2O_2 with ClO^- or the reaction of H_2O_2 with ClO. ClO is an intermediate species of ClO^-, and its presence is highly dependent on the presence of OH in the solution. Without OH, ClO is not formed, and hence the H_2O_2 decomposition reaction only

occurs with ClO^-. This study also proves that if there is a supply of OH gas by plasma, OH will accumulate at the surface of the solution, so that at the surface, ClO^- will react with OH to form ClO. The ClO formed then immediately decomposes H_2O_2, making H_2O_2 decomposition by ClO dominant. However, when the presence of OH decreases, the dominance of H_2O_2 decomposition by ClO also decreases because the concentration of ClO is not high enough, so ClO^- dominates the H_2O_2 decomposition.

In a simple calculation ($O-H_2O_2$ Calc.) in subsection 4.3, it can be seen that H_2O_2 decomposition by ClO is dominant at the surface. The further into the solution, the dominance decreases, and at one point, the decomposition rates between ClO and ClO^- are equal. The initial formation of OH comes from the reaction of O and water (H_2O) to form 2 OH. Once OH is present as an initiator, the chlorine monoxide cycle can finally take place. This formation of OH initially only occurs at the surface of the solution, because O is highly reactive and is not found inside the solution even though O is supplied by the plasma continuously. After the initial OH is formed, OH production is then dominated by the reaction of HOCl with O_2^- via reaction 4.14, which is part of the chlorine monoxide cycle.

In our previous study, there was a decomposition reaction of H_2O_2 by NO_2^- through the reaction

$$NO_2^- + H_2O_2 + H^+ \longrightarrow ONOOH + H_2O \quad . \tag{4.21}$$

The study conducted by Jirasek and Lukes[104] also paid special attention to this reaction considering the high concentration of NO_2^- found in PBS-like solutions (Fig. 4.2). In Fig. 4.3b, the H_2O_2 decomposition reaction with NO_2^- is not visible, because we limited the plot range to rates greater than 10^{-7} mol L^{-1} s^{-1}. Meanwhile, the rate of the reaction at 0.1s is 10^{-11} mol L^{-1} s^{-1} (Supplementary). This result is consistent with our previous study which showed that reaction 4.21 appears at a time range of around 1 s.

Chapter 5

Solvated charged species and pulsed effect analysis

5.1 Introduction

Recently, Atmospheric Pressure Plasma Jets (APPJs) have widely been used in the biological research area [105, 249, 235, 214, 176, 130, 206, 87, 41, 30, 77, 4, 239, 15, 28, 21, 27, 3], for, e.g., water treatment [118, 150, 218, 64, 20, 194, 37, 250], food processing [181, 159, 186, 182, 44, 121, 69], and plasma agriculture [189, 5, 53, 100, 189, 29, 16, 124, 191, 187]. In medical applications, such plasma sources are used for sterilization, wound healing, skin therapy, dental, and cancer treatment. The previous examples all rely on the interaction of the plasma and the liquid which is part of the biological system.

Experiments and simulations to study plasma-liquid interactions are widely found in the literature [80, 224, 148, 240, 142, 146, 97, 231, 155, 232, 145, 98, 9, 11]. In the gas phase, the Reactive Oxygen and Nitrogen Species (RONS) mainly occur before penetrating the biological solution. Following their penetration into the liquid, these react with another chemical species and creating new products. Usually, there are short-lifetime and long-lifetime species. The short-lifetime reaction has come from the reactive species, which acts as an intermediate species. The study about RONS with the solution can find in many reference papers. However, the study mainly discusses the interaction of neutral species rather than charged

species.

Previous studies [127, 198, 73, 9] have considered the effects of solvated electrons in water. Because Phosphate Buffered Saline (PBS) solution contains chemical species that are similar to the composition of the liquid in the human body. Therefore, the usage of PBS solution is relevant in biomedical and biological research, such as SARS-CoV-2 inactivation [247, 233, 48], bacterial inactivation [6, 66, 96, 32], and wound treatment [149, 172, 26, 158]. However, the reaction mechanisms of interaction between charged species and PBS still need to be understood fully.

In this study, we address the question how charge species, $e^-_{(g)}$, $He^+{}_{(g)}$, and $He_2{}^+{}_{(g)}$, originating from a discharge plasma interact with a PBS-like solution (NaCl with constant pH). We perform calculations based on the 1D reaction-transport equation to simulate the interaction of charged species after penetrating the PBS-like solution. The fluxes of charged species from the plasma, driving these mechanisms, are derived from a Particle in Cell / Monte Carlo Collisions simulation of the pulsed atmospheric pressure He plasma. These charged species penetrate the solution via the boundary of the gas and the solution's surface. The effect of pulse flux injection, the dominant chemical reaction pathway, and the final species product inside the solution are presented in this paper.

5.2 Methods and scenarios investigated

In this section, the computation models and system conditions examined in this study are discussed in detail.

Plasma simulation

The time-dependent fluxes of electrons and He ions needed for the liquid-phase transport-reaction model were derived from a plasma simulation based on the Particle-in-Cell/Monte Carlo Collision (PIC/MCC) method [51, 50]. The simulation describes a nanosecond discharge in He gas at atmospheric pressure, created by a high-voltage pulse having a negative polarity. The He gas temperature was set at 298.15 K. The pulse had an amplitude of 1500 V and a trapezoidal waveform

with rise time = plateau = fall time = 5 ns. In the code, the motion of electrons, He^+, and He_2^+ ions was followed within a plane-parallel electrode gap [51], so a spatially 1D PIC/MCC code was used. In such a discharge, He^+ ions are created by electron impact ionisation of He atoms in the plasma. Subsequently, these ions convert into He_2^+ via an efficient three-body ion conversion reaction of $He^+ + He + He \rightarrow He_2^+ + He$. Consequently, He_2^+ can be considered to be the final product of the gas-phase He reactions. The grounded electrode (anode) is assumed to be the surface of the PBS (electrically conductive) solution in this study.

At the beginning of the He plasma simulation, charged species were seeded with an initial density of 1.5×10^{11} cm^{-3} in the He gas phase. During the application of the high-voltage pulse, a significant flux of the electrons reached the (grounded) anode, as a result of the high ionisation rate in the high electric field, while in the afterglow phase - under the conditions of ambipolar diffusion - the flux of the positive ions at the grounded electrode became appreciable. For more details of the plasma simulation, the reader is referred to the works cited above. The electron and ion fluxes obtained from the PIC/MCC simulation are depicted as functions of time in Fig. 5.1(a), while panel (b) shows schematically the system examined in this study.

In the gas-phase simulations, all evaporated species were neglected, and therefore the gas was assumed to be 100 % He, as mentioned above. The 1D PIC/MCC simulation in this study, therefore, does not correspond to a realistic model of He-based plasma jets, where the mixture of He and ambient air and humidity can play an important role in the ionisation mechanism and can generate various RONS, as cautioned in Sec. 5.1. However, for the sake of simplicity, we used the He APP model mentioned above as the source of reactive species entering the surface of the model PBS solution. Accordingly, the only reactive species entering the solution surface were $e^-_{(g)}$, $He^+_{(g)}$, and ${He_2}^+_{(g)}$.

PBS solution

As in the earlier study of [11], the model of a PBS solution used in this study is an aqueous solution with Na^+ and Cl^- being dissolved initially with a concentration of 0.137 mol/l each. Furthermore, its pH is artificially maintained at 7 any time.

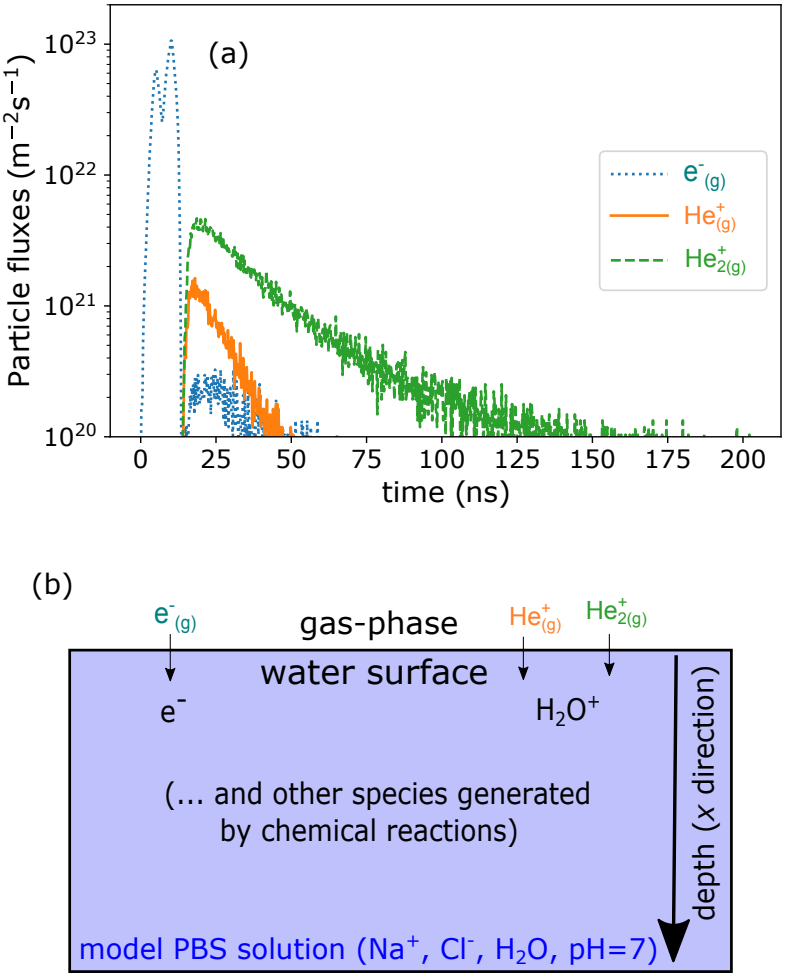

Figure 5.1: (a) Time dependence of the fluxes of gas-phase charged species reaching the grounded boundary (anode) in the PIC/MCC simulation as a consequence of applying a negative high-voltage pulse to the cathode. Here the anode corresponds to the solution surface. (b) The conceptual diagram of the simulation model: Gas-phase electrons $e^-_{(g)}$, helium monomer ions $He^+_{(g)}$, and helium dimer ions ${He_2}^+_{(g)}$ generated by the plasma enter the model PBS solution, which contains Na^+ and Cl^- as solutes. The solution is also assumed to contain an ideal buffer agent such that its pH is set to be constant at 7 at every instance of time to model the buffered condition. Various chemical species are produced via chemical reactions in the solution and diffuse along the depth of the solution.

In other words, the pH buffer effect is infinitely fast, and the concentrations of H^+ and OH^- are set to 10^{-7} mol/l at every instance of time, regardless of the generation or loss of H^+ or OH^- by chemical reactions in the liquid phase. The model PBS solution is also assumed to be in equilibrium with He gas at normal temperature and pressure (NTP), i.e., 298.15 K and 1 atm (=101,325 Pa) prior to the discharge. For this reason, it does not contain N_2 or O_2 dissolved in the solution. Because He is hardly soluble in water, we assume that no He is dissolved in the model PBS solution for the sake of simplicity.

Liquid reaction-transport simulation

The equation for the 1D reaction-transport model used in this study is

$$\frac{\partial n_i}{\partial t} = \hat{\Re}_i - \mathbf{v}_c \cdot \nabla n_i - \mu_i \nabla \cdot (n_i \mathbf{E}) + D_i \Delta n_i \tag{5.1}$$

with $i = 1,2,\cdots,N$, where t, n_i, $\mathbf{v}_c$, and $\hat{\Re}_i$ represent time, the concentration of species i in liquid, the convective flow velocity of water, and the reaction term for all chemical reactions producing or eliminating the species i, respectively, for 73 chemical species, as in [98]. Other symbols μ_i, $\mathbf{E}$, and D_i denote the mobility, electric field, and diffusion coefficient, respectively. (The mobility μ_i is assumed to take a negative value for a negatively-charged species.) The chemical reactions and their rate constants used in our simulations are the same as those in [11], so we also use the same reaction identification number as those of [98] and [11] in this study. The details of the reaction term $\hat{\Re}_i$ are also found in [98] and [11]. The complete sets of diffusion coefficients and mobilities used in this simulation are listed in [98]. We assume there is no convective flow in our system, i.e., $\mathbf{v}_c = \mathbf{0}$. As in the plasma simulation, we solve Eq. (5.1) in one dimension in the depth direction, i.e., the direction perpendicular to the gas-liquid interface (i.e., the solution surface).

The boundary conditions for the charged species are given by the current continuity equation

$$\mathbf{j}_i \cdot \frac{\hat{\mathbf{n}}}{q_i} = (-D_i \nabla n_i + \mu_i n_i \mathbf{E}) \cdot \hat{\mathbf{n}}, \tag{5.2}$$

where $\mathbf{j}_i$, $\hat{\mathbf{n}}$, and q_i denote the current density carried by charged species i, the unit vector normal to the solution surface, and electrical charge of species i, respectively.

More specifically, if the absolute value of the gas-phase electron flux to the solution surface is denoted by Γ_e, the boundary conditions for electrons are

$$\Gamma_e = -D_e \frac{\partial}{\partial x}[e^-] - |\mu_e|[e^-]E\,,$$

where $[e^-]$ is the concentration (i.e., density) of the solvated electrons in the solution, D_e and μ_e are the diffusion coefficients and mobility of the solvated electrons, E is the component of the electric field in the x-direction, e denotes the absolute value of the unit charge of the electron, and x denotes the depth measured from the solution surface. Here we have assumed that all gas-phase electrons arrived at the solution surface are immediately incorporated into the solution as solvated electrons.

For $\mathrm{He^+_{(g)}}$ and ${\mathrm{He_2}^+}_{\mathrm{(g)}}$ ions in the gas phase, we assume that, when an ion reaches the solution surface, its positive charge is transferred to a water molecule $\mathrm{H_2O}$ to form a water ion $\mathrm{H_2O^+}$. In other words, reactions

$$\mathrm{He^+_{(g)}} + \mathrm{H_2O} \longrightarrow \mathrm{H_2O^+} + \mathrm{He} \tag{5.3}$$

$${\mathrm{He_2}^+}_{\mathrm{(g)}} + \mathrm{H_2O} \longrightarrow \mathrm{H_2O^+} + 2\,\mathrm{He} \tag{5.4}$$

take place on the solution surface. As discussed earlier, no He is assumed to dissolve in water, so the boundary conditions for positive ions are given by

$$\Gamma_{\mathrm{He^+}} + \Gamma_{\mathrm{He_2^+}} = -D_{\mathrm{H_2O^+}} \frac{\partial}{\partial x}[\mathrm{H_2O^+}] + \mu_{\mathrm{H_2O^+}}[\mathrm{H_2O^+}]E\,,$$

where $\Gamma_{\mathrm{He^+}}$ and $\Gamma_{\mathrm{He_2^+}}$ are the ion fluxes of $\mathrm{He^+_{(g)}}$ and ${\mathrm{He_2}^+}_{\mathrm{(g)}}$ to the solution surface, $[\mathrm{H_2O^+}]$ is the concentration of $\mathrm{H_2O^+}$ in the solution, and $D_{\mathrm{H_2O^+}}$ and $\mu_{\mathrm{H_2O^+}}$ are the diffusion coefficient and mobility of $\mathrm{H_2O^+}$.

The densities n_i^{g} and n_i of charge-neutral species i in the gas and liquid phases are matched at the solution surface according to the equation:

$$v_i^{\mathrm{th}} \left(n_i^{\mathrm{g}} - \frac{n_i}{k_i^{\mathrm{H}} R T_{\mathrm{g}}} \right) = -D_i \frac{\partial}{\partial x} n_i \tag{5.5}$$

where v_i^{th} and k_i^{H} represent thermal velocity and Henry's constant of species i. Henry's constants used in this simulation are listed in [98]. The parameter R is the gas constant, and T_{g} is the gas temperature (298.15 K), which is assumed to be

the same as the liquid temperature T_l ($T_\mathrm{g} = T_\mathrm{l}$). The thermal velocity is defined as

$$v_i^\mathrm{th} = \frac{1}{2}\sqrt{\frac{2k_\mathrm{B}T_\mathrm{g}}{\pi m_i}}\,,$$

such that $\Gamma_i = v_i^\mathrm{th}\, n_i^\mathrm{g}$ represents the flux of the gas-phase species i entering the solution surface under the assumption that the gas-phase species i forms a Maxwellian distribution with temperature T_g. Here k_B is the Boltzmann constant (i.e., $R = N_\mathrm{A}k_\mathrm{B}$ with N_A being the Avogadro's constant), and m_i is the mass of the species i. Although no charge-neutral species is assumed to enter the solution boundary, charge-neutral species in the solution must satisfy the boundary conditions (5.5) under the assumption that their gas-phase density is null.

Space charge effects and pH buffering

1D reaction-transport equation (5.1) must be solved simultaneously with Poisson's equation

$$\Delta\varphi = -\frac{\rho}{\epsilon}\,, \tag{5.6}$$

where φ is the electrostatic potential defined by $\mathbf{E} = -\nabla\varphi$, ρ is the local charge density of liquid-phase species, and ϵ is the permittivity of pure water. The boundary conditions for Poission's equation (5.6) under 1D conditions are given by $\varphi = 0$ at $x = 0$ and $\partial\varphi/\partial x = 0$ at $x = \infty$.

In this study, we assume instantaneous and perfect pH buffering due to the presence of an ideal buffering agent with infinitely large diffusion coefficients. For example, we assume that a model salt AB, forming the positive ion A^+ of a base and the negative ion B^- of an acid in the solution, is present in the solution and works as an ideal buffer agent and removes excess H^+ or OH^- by forming charge-neutral species HB or AOH locally. Furthermore, for the sake of simplicity, the remaining A^+ or B^- ions are assumed to redistribute themselves instantly over the entire volume, maintaining the uniform distributions (profiles) of A^+ and B^-. Under such conditions, the total charge is always conserved, but the local charge difference between A^+ and B^- is negligible if the volume is sufficiently large. In this limit, the ideal buffering is equivalent to setting $[\mathrm{H}^+] = [\mathrm{OH}^-] = 10^{-7}$ mol/l at every instance of time in the numerical simulation. In evaluating the local charge

density ρ, therefore, we only sum up the charges of all simulated charged species in the solution, without taking into account the charges of the ideal buffering agent, which is not explicitly included as charged species in the simulation.

Global model

In contrast to the 1D reaction-transport model, the global model (i.e., zero-dimensional model) assumes the liquid is stirred very quickly so that the concentration of each species is homogeneous in the solution. The governing equation of the global model is given by

$$\frac{\partial n_i}{\partial t} = \hat{\Re}_i + \frac{1}{V} \cdot v_i^{\mathrm{th}} \left(S_{\mathrm{in}} \cdot n_i^{\mathrm{g}} - S_{\mathrm{out}} \cdot \frac{n_i}{k_i^{\mathrm{H}} \cdot R \cdot T_{\mathrm{g}}} \right) , \tag{5.7}$$

where V denotes the volume of the solution, S_{in} is the area of plasma exposure on the solution surface, S_{out} is the area of the solution surface. For further details, the reader is referred to Ref. [11]. The liquid-phase chemical reactions used in the global model are identical to those used in the 1D reaction-transport model. This ensures a relevant comparison between the 1D and global models.

As in [11], we consider the case where a 1 mL model PBS solution is placed in a Petri dish with an area of 10 cm^2 such that the depth of the solution is 0.1 cm. A part of the solution surface is exposed to a plasma jet with a cross section of 0.1 cm^2, which is placed perpendicular to the surface of the solution. Under these conditions, we set V =1 mL, S_{in} =0.1 cm^2, and S_{out} =10 cm^2.

Scenarios investigated

In this study, we investigate four different scenarios that differ in the time-dependence of the fluxes of plasma species penetrating the liquid:

- Case A: 'single pulse injection,' in which the ion and electron fluxes enter the liquid surface, following the time-dependent ion and electron fluxes shown in Fig. 5.1(a).

- Case B: 'short continuous injection,' in which the electron and ion fluxes shown in Fig. 5.1(a) are averaged over a time interval of 0.1 ms (i.e., 10^{-4} s),

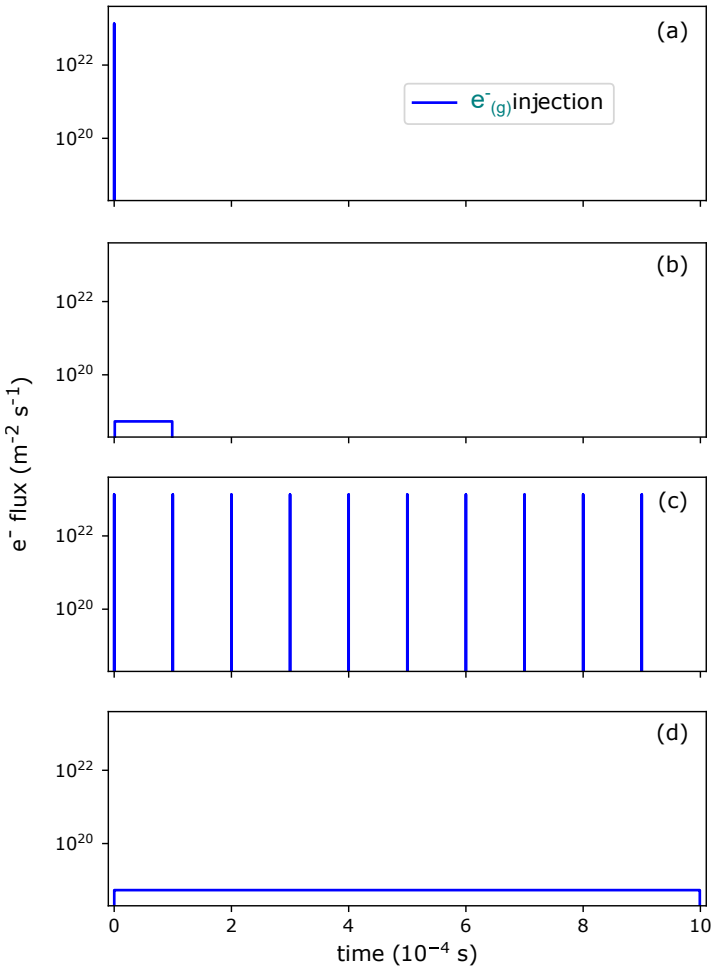

Figure 5.2: The time dependence of ion and electron fluxes was simulated with two different injection methods: a pulsed injection and a continuous injection over a period of 0.1 ms (i.e., 10^{-4} s). A single pulse injection shown in (a) consists of the time-dependent fluxes of ions and electrons represented in Fig 1(a). The total ion and electron fluences of the single pulse are the same as those of the short continuous injection of (b). In (c), the ions and electrons are injected into the liquid surface with multiple pulses with a constant time interval of 0.1 m s, with each pulse being the same as the single pulse of (a). (Multiple pulse injections). In (d), the ions and electrons are injected continuously, extending the continuous injection of (b) such that the total ion and electron fluences are the same as those of (c) (Long continuous injection).

with the total fluence of each species to the solution surface over the period being the same as that of Case A;

- Case C: 'multiple pulse injections,' in which the incoming fluxes considered in the single pulse case of A are repeated 10 times, with a repetition period of 10^{-4} s, i.e., at a frequency of 10 kHz;

- Case D: 'long continuous injection,' in which the fluxes used in Case C are time averaged over a time interval of 10^{-3} s.

To illustrate these cases, the time-dependence of the electron flux is plotted schematically in Fig. 5.2. Here the horzonal axis represents time t and the first pulse starts at $t = 0$, as in Fig. 5.1(a).

The total fluence of the electrons for Cases A and B is $5.35 \times 10^{23}\,\mathrm{m}^{-2}$, while it is a factor of 10 times higher in Cases C and D. The simulations cover a time interval of 10^{-4} s for Cases A and B, and 10^{-3} s for Cases C and D.

The first pair of Cases A and B probes the domain of injecting charged species during a relatively short time. The second pair of Cases C and D investigates the effects under conditions when the charged species injection lasts long enough to make the concentration profile of solvated electrons reach saturation. However, the longest time for which we were able to perform the 1D simulation for the above scenario was limited to 10^{-3} s. Therefore, using the global model, we extended the simulation up to 1 s. The pulse injection scenario in this simulation was similar to case C (multiple pulse injections) with extending the number of pulses to 10^4.

5.3 Results and discussion

Case A: single pulse injection

With the 1D simulation, we analysed the depth profiles of chemical species in the liquid due to the single pulse injection of plasma species (Case A), as shown in Fig. 5.3. The plasma irradiation starts at $t = 0$. The four panels correspond to four instances of time: $t = 0$ s, 10^{-7} s, 10^{-4} s, and 10^{-3} s, respectively. The model PBS solution prior to the plasma irradiation, given in Fig. 5.3(a), contains Na^+

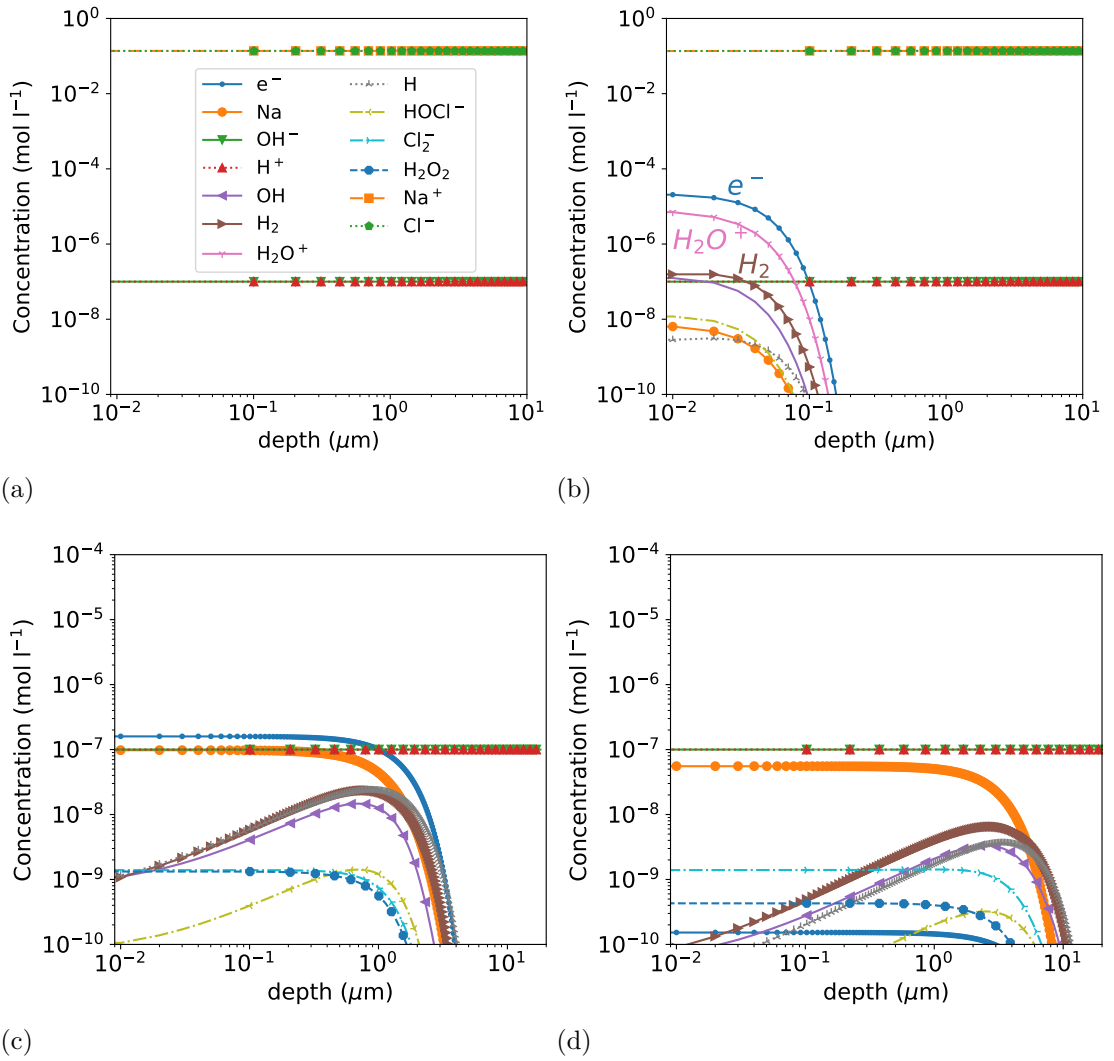

Figure 5.3: Concentration profiles of chemical species in the solution as functions of the depth, obtained from the 1D simulation for a single pulse injection of charged species (Case A) at (a) t = 0 s (i.e., prior to plasma exposure), (b) t = 10^{-7} s, (c) t = 10^{-4} s, and (d) t = 10^{-3} s. Here e^- denotes the solvated electrons. Prior to the plasma irradiation (a), the concentrations of Na^+ and Cl^- are 0.137 mol/l each. Owing to the pH buffer effect, the concentrations of H^+ and OH^- are kept at 10^{-7} mol/l each.

and Cl^- with a concentration of 0.137 mol/l each. Owing to the pH buffer effect, the concentrations of H^+ and OH^- are kept at 10^{-7} mol/l each, corresponding to a pH of 7.

At $t = 10^{-7}$ s (i.e., 100 ns), as shown in Fig. 5.3(b), the two dominant species were solvated electrons and H_2O^+. Recall that a high flux of electrons reached the liquid over a time window of about 10^{-8} s (see Fig. 5.1(a)). The irradiation of $He^+_{(g)}$ and ${He_2}^+{}_{(g)}$ ions was also nearly completed by $t = 10^{-7}$ s. At $t = 10^{-4}$ s and beyond, as seen in (c) and (d) of Fig. 5.3, the generation of additional species and their diffusion towards the bulk of the liquid were observed. By $t = 10^{-4}$ s, solvated electrons reached a depth of around 3 μm. After the plasma irradiation stopped, the concentration of solvated electrons at the gas-liquid boundary continued to decrease to compensate for diffusion. by 10^{-4} s.

Case B: short continuous injection

Figure 5.4 (a) shows the profiles of chemical species in the solution at $t = 10^{-7}$ s in the case of the short continuous injection of charged species over 10^{-4} s (Case B). In contrast to Case A, only small fluences of electrons and ions entered the solution surface by this time, the concentration of solvated electrons was much lower than that in Fig. 5.3(b).

By $t = 10^{-4}$ s, the fluences of electrons and ions injected into the solution surface in Case B were exactly the same as those in Case A. As seen in Fig. 5.3(c) and Fig. 5.4(b), despite the fact that the time dependences of the incident fluxes were significantly different between Cases A and B, the concentration profiles of each chemical species in the solutions were essentially the same in both cases. The detailed differences in concentration profiles between Case A and Case B at $t = 10^{-4}$ s are summarized in Table 5.1. At a later time of $t = 10^{-3}$ s, as seen in Figs. 5.3(d) and 5.4 (c), the concentration profile of each chemical species in the solution remained essentially the same as each other.

Case C: multiple pulse injections

Figure 5.5 shows the concentration profiles of chemical species in Case C, where the concentration profiles at the end of the 2nd and 10th pulse periods, i.e., $t = 2 \times 10^{-4}$ s and 10^{-3} s, are presented in (a) and (b). The concentration profiles of the solvated electrons and H_2O^+ hardly changed from the 2nd pulse, as seen in (a) and (b) of Fig. 5.5. Other species such as OH, H, and H_2 penetrated to a greater

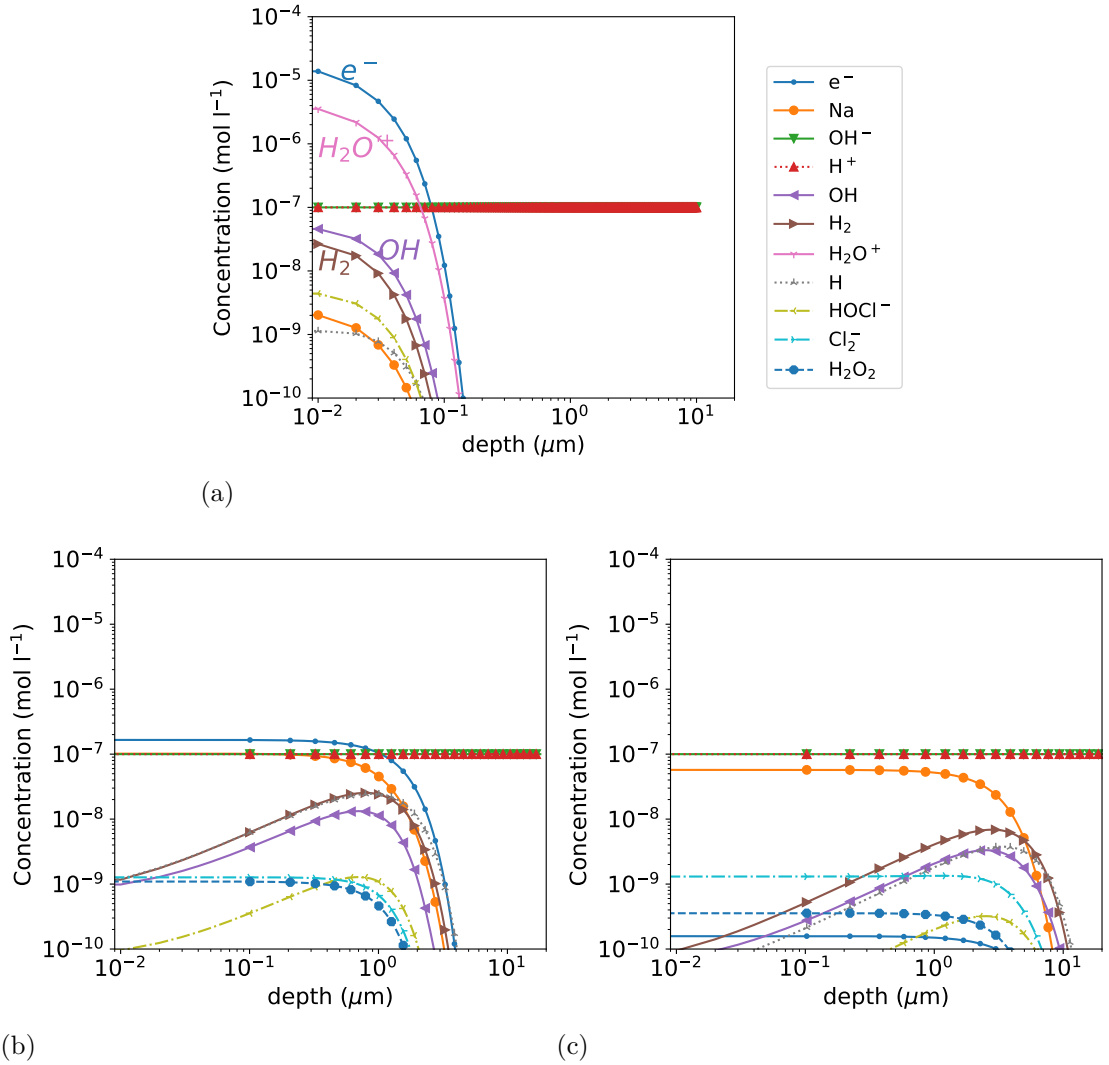

Figure 5.4: Concentration profiles of chemical species in the solution as functions of the depth, obtained from the 1D simulation for a short continuous injection of charged species (Case B) at (a) t = 10^{-7} s, (b) t = 10^{-4} s, and (c) t = 10^{-3} s.

depth of the solution as time proceeded. The behavior of solvated electrons and H_2O^+ is explained by their high reactivity, which prevents them from diffusing deep into the solution. These species were observed and took part in chemical reactions only in a thin liquid layer right below the gas-liquid interface, which we refer to as the reaction boundary layer (RBL). To observe the time evolution of solvated electrons' concentration profiles in the solution, we plot them in Fig. 5.6

Table 5.1: Comparison between 'single pulse' and 'short continuous' injections (Cases A and B) in terms of the concentrations and diffusion depths of various chemical species in the solution at $t = 10^{-4}$ s. The concentration values are measured on the solution surface. The depth value corresponds to the position where the species' concentration is 10^{-10} mol/l.

Species	Single pulse injection		Short continuous injection	
	Conc. (mol/l)	Depth (μm)	Conc. (mol/l)	Depth (μm)
e^-	1.63×10^{-7}	3.9	1.65×10^{-7}	3.91
Na	9.9×10^{-8}	3.10	1.02×10^{-7}	3.23
OH	1.4×10^{-9}	2.70	9.8×10^{-10}	2.68
H	1.3×10^{-9}	4.05	1.16×10^{-9}	4.07
$HOCl^-$	1.04×10^{-10}	2.05	–	2.04
Cl_2^-	1.4×10^{-9}	1.78	1.25×10^{-9}	1.74
H_2	1.0×10^{-9}	3.3	1.16×10^{-9}	3.48
H_2O_2	1.0×10^{-9}	1.65	1.08×10^{-9}	1.61

in (a) logarithmic and (b) linear scales. As seen in Fig. 5.6(b), their profiles after the 2nd pulse almost overlapped and were hardly distinguishable.

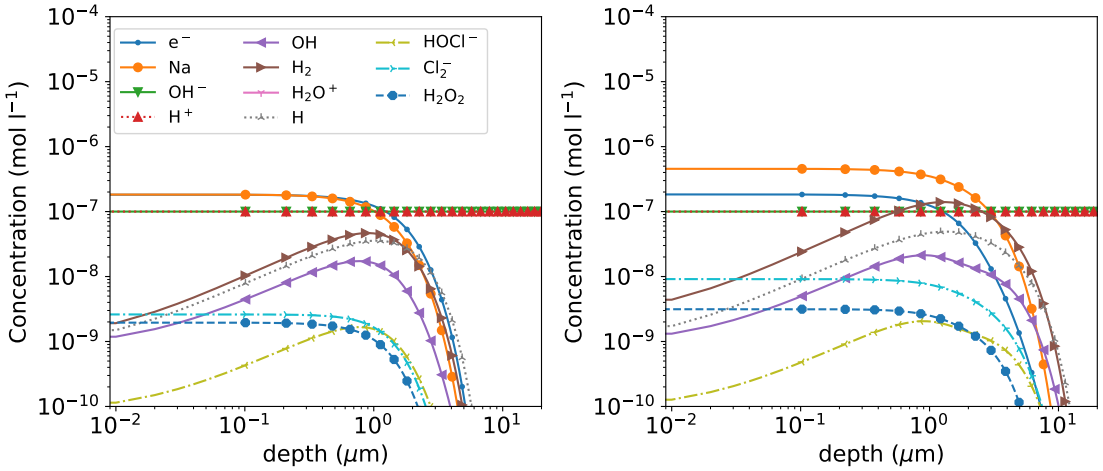

(a) (b)

Figure 5.5: Concentration profiles of chemical species in the solution as functions of the depth, obtained from the 1D simulation for multiple pulse injections of charged species (Case C) after the (a) 2nd pulse period ($t = 2 \times 10^{-4}$ s) and (b) 10th pulse period ($t = 10^{-3}$ s).

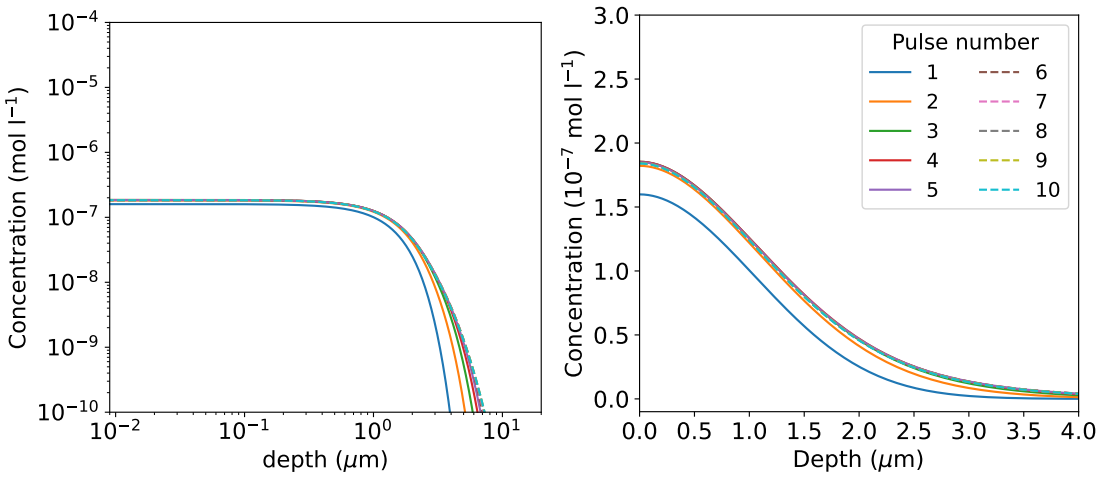

(a) (b)

Figure 5.6: Concentration profiles of solvated electrons in the solution as functions of the depth, obtained from the 1D simulation for multiple pulse injections of charged species (Case C) at the ends of different pulse periods in (a) logarithmic and (b) linear scales for the depth, i.e., at $t = n \times 10^{-4}$ s for pulse number $n = 1, \cdots, 10$.

Case D: long continuous injection

Figure 5.7 shows the concentration profiles of chemical species in the solution at $t = 10^{-3}$ s for Case D. The fluences of electrons and He ions were the same as those of Fig 5.5(b), i.e., the total fluences of 10 pulses. It is seen that the concentration profiles were essentially identical between Fig. 5.5(b) and Fig. 5.7. This is expected from our earlier observations of similarity in the final concentration profiles between Cases A and B.

Long-time simulation with the global model

The computationally intensive nature of the 1D reaction-transport model prevents simulations on long timescales. Therefore, we carried out additional calculations based on the global model to uncover the time evolution of the system for long plasma exposure time.

To verify the accuracy and consistency of the global-model simulations, the

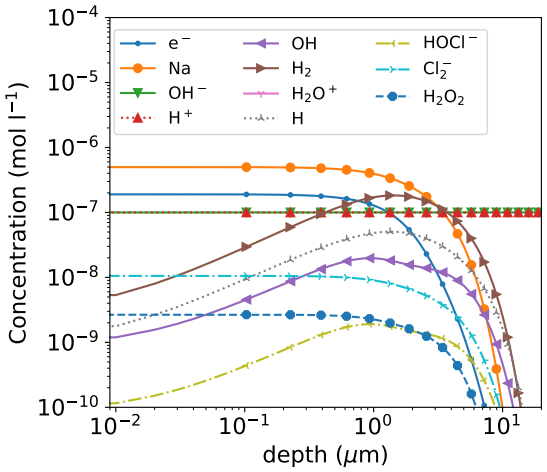

Figure 5.7: Concentration profiles of chemical species in the solution as functions of the depth, obtained from the 1D simulation at the end of a long continuous injection of charged species (Case D), i.e., $t = 10^{-3}$ s.

first set of simulations was run only for a short time duration of 10^{-3} s with 10 plasma pulses (Case C) to allow comparison with the results of the corresponding 1D reaction-transport model simulation. To relate the 1D simulation with the global simulation in a simple manner, we assumed that the liquid-phase chemical species were generated and confined only in the volume under the area S_{in} exposed to the plasma, but their spatial averages were taken over the entire solution volume V. The volume-averaged concentrations $\bar{n}_i$ of species i at time t was derived from the integration of the corresponding concentration profile $n_i(t, x)$ evaluated from the 1D reaction-transport equation (5.1) with respect to the depth x, i.e.,

$$\bar{n}_i(t) = \frac{S_{\text{in}}}{V} \int_0^L n_i(t, x)\, \mathrm{d}x\,, \tag{5.8}$$

where L is the depth of the solution defined by $L = V/S_{\text{out}}$. As discussed in Subsec. 5.2, the area of plasma irradiation on the solution surface was set at $S_{\text{in}} = 0.1$ cm, the entire solution surface where charge-neutral species can disorb was $S_{\text{out}} = 10$ cm^2, and the solution volume was $V = 1$ ml, such that $L = 0.1$ cm in this study. The volume-averaged concentration $\bar{n}_i$ above corresponds to the concentration of species i obtained from the global model equation (5.7).

Figure 5.8 shows the (volume-averaged) concentrations of the most dominant

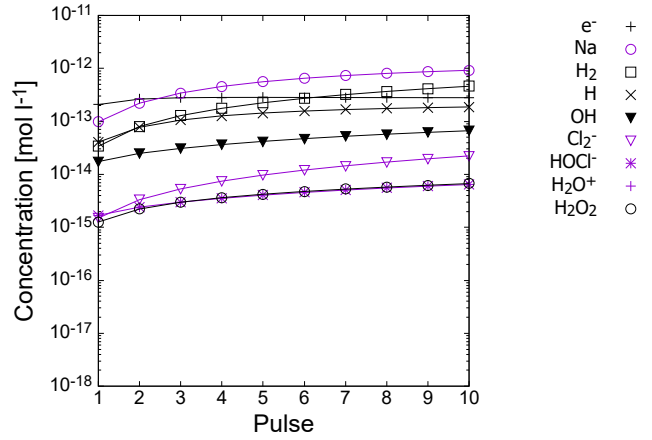

(a)

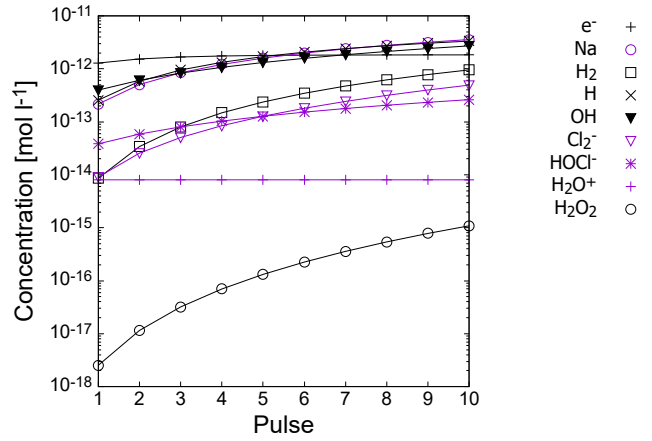

(b)

Figure 5.8: Time evolution of (a) the volume averaged concentrations of chemical species obtained from the 1D simulation and Eq. (5.8) and (b) the concentrations of chemical species obtained from the global-model simulation for multiple pulse injections of charged species (CaseC). The concentrations were evaluated at the end of each pulse period, i.e., $t = n \times 10^{-4}$ s with $n = 1, \cdots, 10$. The horizontal axis indicates the pulse number n. It should be noted that the concentrations of highly reactive reacting species such as solvated electrons vary significantly between two consecutive pulses, which is not shown in this figure.

species in the solution obtained from the 1D and global simulations under the discharge conditions of Case C. The concentrations were evaluated at the end of each pulse period, i.e., at $t = 1.0 \times 10^{-4}$ s for the first pulse, $t = 2.0 \times 10^{-4}$ s for

the second pulse, etc. up the 10th pulse. The number of pulses is displayed on the horizontal axis. Figure 5.8(a) gives the results of the 1D simulation and (b) the global simulation.

Because gas-phase electrons directly enter the solution and become solvated electrons, the obtained concentrations of solvated electrons are expected to be similar between the 1D and global models. However, as seen in Fig. 5.8, the concentration of solvated electrons obtained from the 1D simulation was significantly lower than that from the global model, by almost an order of magnitude. As will be discussed more in detail, this is due to the fact that the dominant loss mechanism of solvated electrons was the second-order recombination. In the 1D simulation, solvated electrons are initially formed in the RBL, where their concentration is high and the second-order recombination proceeds rapidly. In the global model, solvated electrons are distributed uniformly in the solution and their initial concentration is low, which results in slow recombination.

Another species of interest is H_2O^+, as it is this species that is formed by the positive He ions entering the solution surface. The H_2O^+ concentrations obtained from the 1D and global simulations were practically identical (around 8×10^{-15} mol/l) and also evolve in time nearly identically. Similar to the solvated electrons, H_2O^+ ions are also initially formed in the RBL in the 1D simulation whereas they are distributed uniformly in the solution in the global simulation. However, the dominant loss mechanism of H_2O^+ ions is the first-order decay to form H^+ ions and OH radicals and the decay rate is only proportional to the concentration of H_2O^+. This is why the total amounts of H_2O^+ in the same volume obtained from the 1D and global simulations remained essentially identical.

Some species such as Na, H_2, Cl_2^-, and $HOCl^-$ also exhibited good agreement between the 1D and global simulations. Other species, however, did not agree as well probably because they were the products of more complex combinations of secondary reactions. The definition of secondary reactions will be presented in Sec. 5.4.

Considering the fact that the global-model simulation can predict the concentrations of various species to a somewhat satisfactory degree up to 10 pulses ($t = 10^{-3}$ s), we extended the simulation up to 10^4 pulses ($t = 1$ s). The results are shown in Fig. 5.9. Seven species emerged in concentrations above 10^{-10} mol/l.

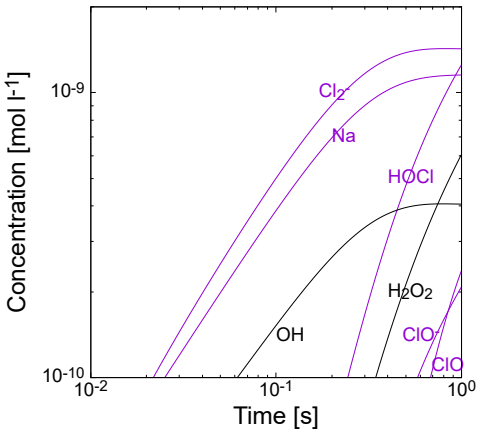

Figure 5.9: Time evolution of the concentrations of chemical species obtained from the global-model simulation for multiple pulse injections of charged species of case C extending to 10^4 pulses, i.e., up to $t = 1$ s. Note that both axes are in log scale.

The species with the highest concentrations in Fig. 5.9 are Cl_2^- and Na but they eventually reach saturation. On the other hand, the concentrations of HOCl and H_2O_2 continue to increase. Because both are stable species, their concentrations are expected to increase further until their desorption from the solution surface is balanced with their production. It should be noted that, in aqueous solution, hypochlorous acid HClO is partially dissociated to form hypochlorite anion ClO^-, but, at pH =7, HClO is known to be more dominant than ClO^-.

5.4 Reaction pathways

We now explore the dominant reaction pathways in the model PBS solution induced by the incident charged species generated in the He APP. Reaction profile data for Case C (multiple pulse injections) at 9.1×10^{-4} s (i.e., soon after 10 pulse injections) are employed for the analysis because Case C represents a realistic pulsed plasma injection system. We divide the reaction pathways into two sets: the primary reactions, which are the chemical reactions directly driven by the primary species (charged species from the gas), and the secondary reactions, which are the ones that follow the primary reactions.

Primary reactions

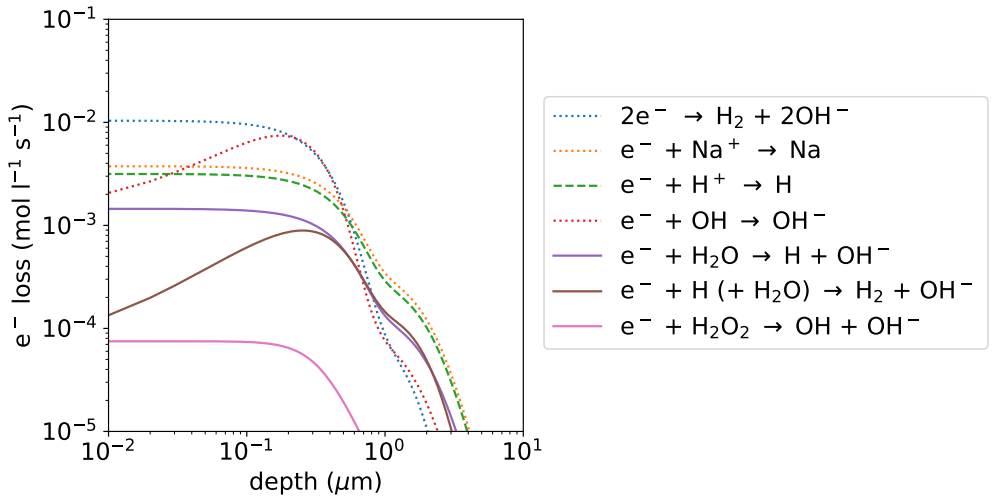

(a)

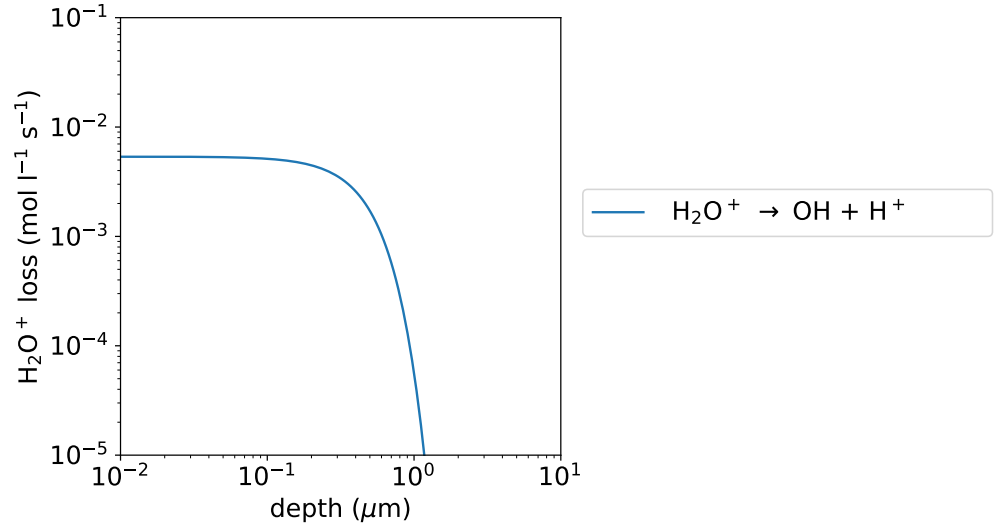

(b)

Figure 5.10: Loss rate profiles of (a) solvated electrons and (b)H_2O^+ due to chemical reactions in the solution as functions of the depth, obtained from the 1D simulation for multiple pulse injections of charged species (Case C) and evaluated at $t = 9.1 \times 10^{-4}$ s, i.e., soon after the 10th pulse.

The primary reactions driven by incident electrons are those involving sovlated

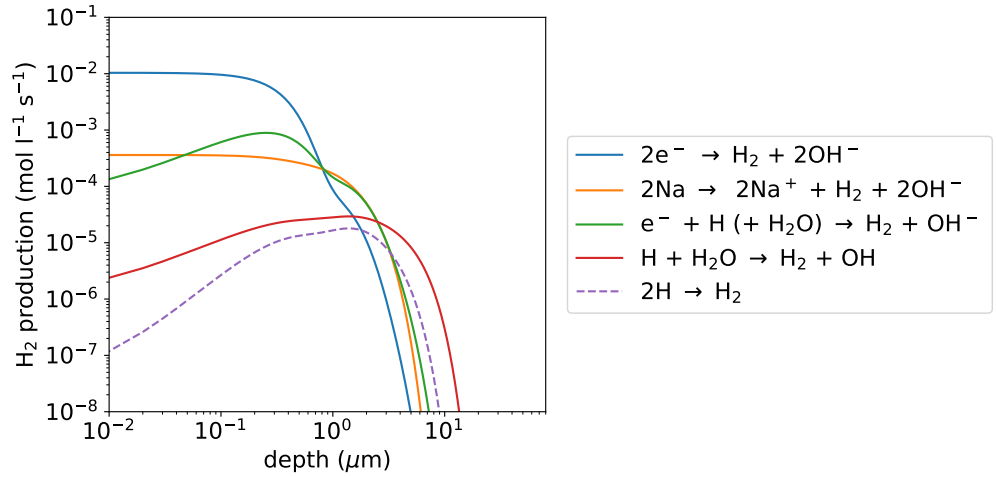

(a)

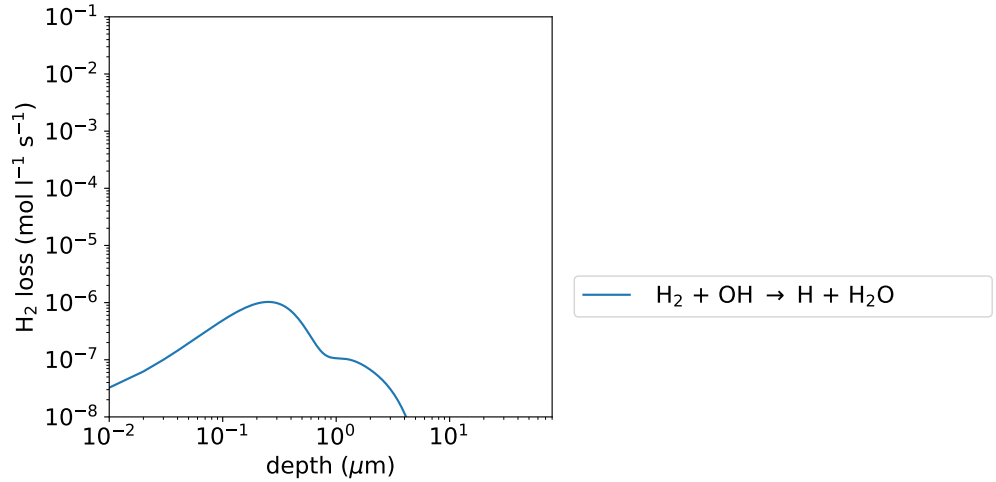

(b)

Figure 5.11: (a) Production and (b) loss rate profiles of H_2 molecules due to chemical reactions in the solution as functions of the depth, obtained from the 1D simulation for multiple pulse injections of charged species (Case C) and evaluated at $t = 9.1 \times 10^{-4}$ s, i.e., soon after the 10th pulse. The primary loss of H_2 is attributed to the desorption of H_2 molecules from the solution surface, which is not included in this figure.

electrons. Figure 5.10(a) shows the loss reaction channels of solvated electrons. The dominant loss reaction for solvated electrons is their second-order recombina-

tion (R_O005 of [98])[83, 198]

$$2\,e^- \longrightarrow H_2 + 2\,OH^-\,, \tag{5.9}$$

with a rate constant of 5.5×10^9 $(\mathrm{mol/l})^{-1}\mathrm{s}^{-1}$. This reaction takes place mostly in the RBL. In a deeper region, as the concentration of OH increases due to other reactions, solvated electrons are also lost via (R_O008)

$$e^- + OH \longrightarrow OH^-\,.$$

Solvated electrons also reduce sodium ions via Reaction R_x001 of [98], i.e.,

$$e^- + Na^+ \longrightarrow Na\,. \tag{5.10}$$

However, the subsequent reaction R_x002, i.e., second-order recombination of Na

$$2\,Na^+ \longrightarrow 2\,Na + {H_2}^+ + 2\,OH^-$$

with a rate constant of 1.5×10^9 $(\mathrm{mol/l})^{-1}\mathrm{s}^{-1}$ recovers Na^+. Therefore, Na does not accumulate in the PBS solution although the concentration of Na reaches a certain level while the production and loss of Na continue and balance.

The primary reactions driven by incident positive ions are those involving H_2O^+. As discussed earlier, positive ions originating from the plasma generate water ions H_2O^+ on the solution surface via reactions (5.3) and (5.4). A water ion readily decays to form an H^+ ion and an OH radical through Reaction R_O046 of [98]), i.e.,

$$H_2O^+ \longrightarrow H^+ + OH \tag{5.11}$$

with a rate constant of 3.3×10^5 s^{-1}. As seen in Fig. 5.10(b), this is the only loss mechanism of H_2O^+. In other words, nearly all incident positive charges eventually form H^+ in the solution. This is consistent with earlier observations[101, 184] that the only positive ions forming water clusters in a discharge with humid air are H^+ and NO^+. (In our simulation, no NO^+ is considered.[98]) It should be noted, therefore, that if we used Ar plasmas instead of He plasmas, the liquid phase reactions are essentially the same. It is seen in Fig. 5.10(b) that H_2O^+ decays only in the RBL with a thickness of about 1μm, where H^+ ions and OH radicals are produced.

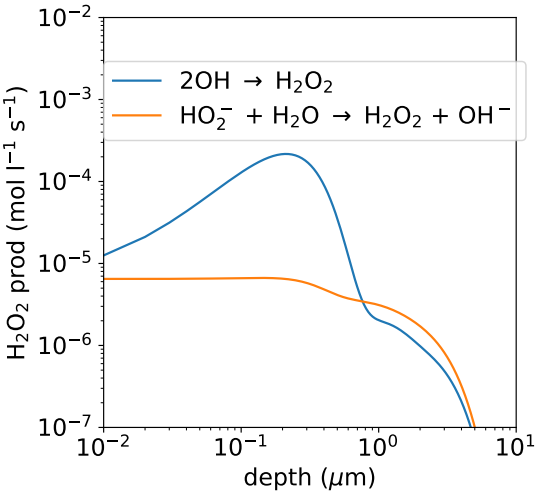

Figure 5.12: Production rate profiles of H_2O_2 due to chemical reactions in the solution as functions of the depth, obtained from the 1D simulation for multiple pulse injections of charged species (Case C) and evaluated at $t = 9.1 \times 10^{-4}$ s, i.e., soon after the 10th pulse.

The stable species generated from the primary reactions are H_2 molecules, as seen in Eq. 5.9. Figure 5.11 shows the production and loss rates of H_2. It is seen in Fig. 5.11(a) that the dominant reaction to produce H_2 is the second-order recombination of solvated electrons. On the other hand, the loss of H_2 in the solution is extremely small, as seen in Fig. 5.11(b). Although the data are not shown here, the primary loss of H_2 molecules occurs as the desorption from the solution surface.

Secondary reactions

Hydroxyl radicalsOH generated by the decay of H_2O^+, i.e., Reaction (5.11), can form hydrogen peroxide H_2O_2 through their second-order recombination reaction R_O041

$$2\,OH \longrightarrow H_2O_2 \tag{5.12}$$

with a rate constant of $5.0\times\ 10^9$ $(mol/l)^{-1}s^{-1}$. Figure 5.12 shows that this reaction is the dominant reaction producing H_2O_2 in the solution. Because H_2O_2 is highly stable, it continues to accumulate in the solution, as indicated in Fig. 5.9. OH

radical also reacts with chlorine anions Cl^- via Reactions $R_{Cl}058$

$$OH + Cl^- \longrightarrow HOCl^- , \tag{5.13}$$

where $HOCl^-$ is a reaction intermediate[7], which further reacts with Cl^- to form a dichloride radical anion $Cl_2{}^-$ via Reaction $R_{Cl}007$

$$HOCl^- + Cl^- \longrightarrow Cl_2{}^- + OH^- . \tag{5.14}$$

Figure 5.13 shows that Rectiion (5.13) is the far dominant mechanism of the consumption of Cl^- ions in the solution. A dichloride radical anion $Cl_2{}^-$ is highly reactive and reacts with an OH radical to generate HOCl via Reaction $R_{Cl}023$

$$Cl_2{}^- + OH \longrightarrow HOCl + Cl^- . \tag{5.15}$$

Figure 5.14 shows that Reaction (5.15) is the dominant reaction to produce HOCl. It is known that HOCl is relatively stable under pH = 7 conditions and, therefore, can accumulate in the solution until its desorption from the solution surface is balanced with its production.

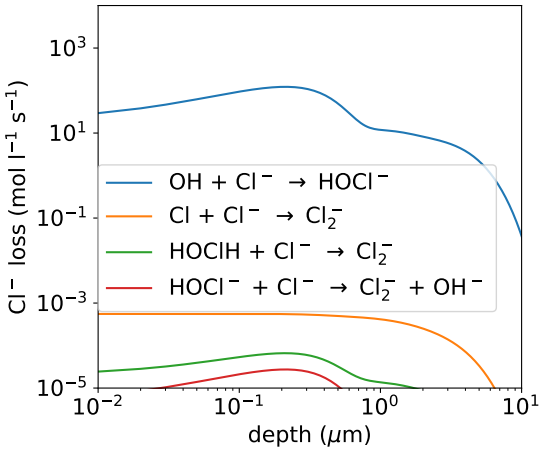

Figure 5.13: Loss rate profiles of Cl^- due to chemical reactions in the solution as functions of the depth, obtained from the 1D simulation for multiple pulse injections of charged species (Case C) and evaluated at $t = 9.1 \times 10^{-4}$ s, i.e., soon after the 10th pulse.

The analysis of the data obtained from the simulations presented above helped to find the most prominent reaction channels in the solution; these are shown

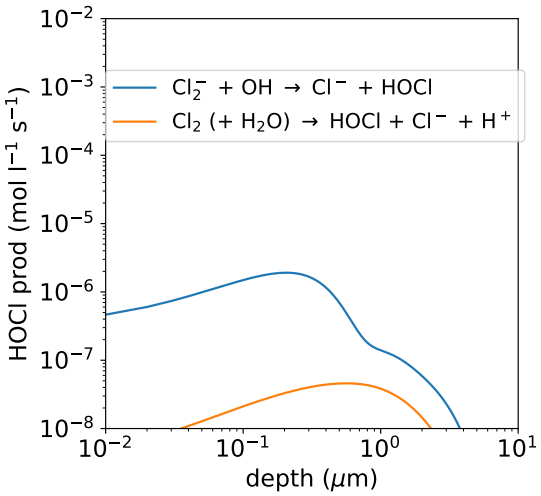

Figure 5.14: Production rate profiles of HOCl due to chemical reactions in the solution as functions of the depth, obtained from the 1D simulation for multiple pulse injections of charged species (Case C) and evaluated at $t = 9.1 \times 10^{-4}$ s, i.e., soon after the 10th pulse.

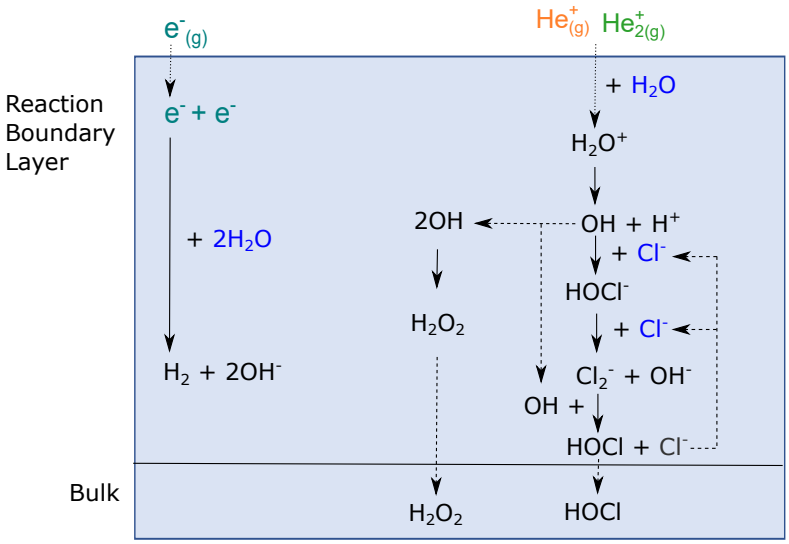

Figure 5.15: The dominant chemical reactions inside the model PBS solution initiated by gas-phase charged species ($e^-_{(g)}$, $He^+_{(g)}$, and $He_2{}^+{}_{(g)}$) that penetrate the model PBS solution.

in Fig. 5.15. The reactions start from the charged species from the gas phase penetrating the model PBS solution. The chemical reactions on the left side of the figure are the ones caused by electrons. Positive ions cause chemical reactions on the right side of the figure.

5.5 Conclusions

Numerical simulations based on the 1D reaction-transport model and the global model were performed to clarify the effects of charged species ($e^-_{(g)}$, $He^+_{(g)}$ ${He_2}^+{}_{(g)}$) injections from He APPs into a model PBS solution. The fluxes of the charged species for a single-pulse plasma activation were derived from 1D PIC/MCC simulations of a nanosecond pulsed He APP. We studied four scenarios to understand the impact of repetitive and continuous charge injections. These simulations identified the dominant chemical reaction pathways inside the PBS solution.

The results obtained from the 1D simulations showed the liquid-phase chemical species produced by the incident charged species from the plasma. In the simulations, all incident gas-phase electrons were assumed to dissolve into the solution as solvated electrons. Solvated electrons are highly reactive and form hydrogen molecules H_2 and hydroxide OH^- through their second-order recombination. Note that the 1D simulation is needed to reproduce these recombination reactions of solvated electrons correctly because they are likely to occur when the concentration of solvated electrons is sufficiently high near the gas-liquid interface before they diffuse into the solution. In the global model, where the diffusion is infinitely high and all chemical species are assumed to be uniformly distributed over the entire liquid volume, the reaction rate of any second-order recombination is typically underestimated.

Although the generation of H_2 molecules is initiated by gas-phase electron irradiation, the reactions to produce H_2 molecules in this study are different from those of water electrolysis, which also produces H_2 gases on the cathode surface. In typical water electrolysis, H^+ ions are produced on the anode surface, and after passing through the membrane, they react with electrons on the cathode surface. In the case of plasma exposure examined in this study, the direct recombination

of a solvated electron and an H^+ ion is less important than the second-order recombination of solvated electrons, as shown in Fig. 5.10(a).

The gas-phase positive ions, i.e., $He^+_{(g)}$ and ${He_2}^+{}_{(g)}$, were assumed to transfer their charges to water molecules when they reached the gas-liquid interface. Because He hardly dissolves in water, no He was assumed to be in the solution in this study. Water ions H_2O^+ readily decompose to form H^+ ions and OH radicals. The latter can form H_2O_2 through their second-order recombination (5.12).

OH radicals also react with Cl^- ions in the solution through Reactions (5.13) to (5.15) to produce HOCl. Starting the generation of H^+ and OH radicals of Reaction (5.11), the sequence of reactions consumes a single H^+ ion, two OH radicals, and a single Cl^- ion and produce a single HOCl molecule and a single H_2O molecule. In other words, the combined reaction may be summarized as

$$2\,H_2O^+ + Cl^- \longrightarrow H^+ + HOCl + H_2O\,. \tag{5.16}$$

In the case of plasma exposure, the same number of electrons and positive ions enter the solution surface eventually. Therefore, the reactions (5.12) or the positive-charge induced reaction sequence (5.16) above and the electron-induced reactions (5.9) take place almost simultaneously. The total reactions, where a H^+ ion generated in Reaction (5.11) or (5.16) recombines with an OH^- ion generated in Reaction (5.9), indicate that, in the absence of a pH buffer, either the production of H_2O_2 occurs with no change in pH or the production of HOCl occurs by converting NaCl to NaOH (i.e., Cl^- to OH^-). In the presence of a pH buffer, OH^- may be replaced with a negative ion of the buffering agent.

The comparison of the 1D simulation results obtained for pulsed and continuous flux injections (Cases C and D) showed that the concentration profiles of generated chemical species were essentially the same between these two cases after sufficiently long plasma exposure. This is because, although some reactions in the RBL are fast, only relatively stable species (whose reaction time scales are much longer than the single-pulse plasma irradiation time) remain in the solution. Therefore, the effects of pulse injections are averaged over time.

The stable chemical species generated by He APP exposure are found to be H_2, H_2O_2, and HOCl. Generated H_2 is mostly lost as desorption from the solution surface because it is generated only near the gas-liquid interface due to

the electron-induced reactions and its solubility is sufficiently low. The global-model simulation of Fig. 5.9 indeed showed the continuous accumulation of H_2O_2 and HOCl under the conditions examined in this study. A practical comparison between the present simulation study and the corresponding experiments would, therefore, be the measurement of the concentrations of H_2O_2 and HOCl in the solution. However, a quantitative comparison also requires an accurate evaluation of the electron and ion fluxes entering the solution surface, which may pose additional technical challenges.

Chapter 6

Summary

This dissertation investigates the interaction of plasma with liquid (PBS-like solution) numerically using a global model (0D) and 1D reaction-transport simulation. The liquid parameter used is a salt solution with constant pH, resembling PBS. This solution is referred to as a PBS-like solution. The salt (NaCl) in the solution is assumed to be fully ionized with equal concentrations of Na^+ and Cl^-, namely 0.137 mol/L. To maintain a constant pH (7), it is assumed that the phosphate buffer does not react with other species, but only contributes to pH consistency by balancing the concentrations of H^+ and OH^- at 10^{-7} mol/L. This PBS-like solution is then used as the object of the study. The following assumption is that during plasma irradiation, the solution is in thermal equilibrium with the ambient air. 80% N_2 and 20% O_2 flow from free air into the solution at a pressure of 1 atm at room temperature (298.15 K).

The first and second investigations study the interaction of plasma irradiation on PBS-like solution. The investigations are conducted within the solution using a global model and 1D reaction-transport simulation for the first and second investigations, respectively. The gas-phase (plasma) chemical species are obtained from previous research conducted by Wende, et al.[240] with a global-kin application. There are 12 gas species that penetrate the PBS solution. In the PBS solution simulation, we employ 318 chemical reactions, consisting of 77 ROS, 77 RNS, 54 chlorine reactions, and 2 reactions related to Na. A total of 60 species are found in our simulation after the gas species penetrate the solution.

In the first investigation, we employ a 0D (global model) to investigate the major reaction pathways of H_2O_2 decomposition in a PBS-like solution. This investigation reveals two distinct cycles for H_2O_2 decomposition in the PBS-like solution. The first cycle involves the direct decomposition of H_2O_2 by ClO^-. ClO^- originates from the reaction of Cl^- in the solution with O supplied from the plasma gas. The decomposition process yields H_2O, O_2, and Cl^-, and Cl^- subsequently reacts with O again. The second cycle involves the decomposition of H_2O_2 by ClO. ClO is formed via the reaction of ClO^- with OH. ClO decomposes H_2O_2 to produce HOCl and HO_2, and $HO_2{}^-$ decomposes to yield $O_2{}^-$ and H^+. $O_2{}^-$ reacts with HOCl to produce Cl^-, O_2, and OH. Subsequently, OH reacts with ClO^- to form ClO. ClO serves as an intermediate in the ClO^- mediated decomposition of H_2O_2. The indirect decomposition of H_2O_2 is ultimately dependent on the amount of O supplied by the gas. The greater the O supply by the plasma gas, the higher the amount of H_2O_2 that can be decomposed.

In the second investigation, we employ a 1D reaction-transport simulation to identify the dominant reaction pathways. The objective and variables used are identical to those in the first investigation. We incorporate transport factors into the calculations, rendering the analysis more realistic. This investigation yields results that are consistent with the first investigation, elucidating the dominant reaction pathways for H2O2 decomposition in a PBS-like solution. It is also found that H2O2 decomposition occurs via two distinct cycles. The first cycle involves the direct decomposition of H2O2 by ClO-, while the second cycle involves the decomposition of H2O2 via ClO.

The advantage of using a 1D reaction-transport simulation is that it allows us to determine the reaction depth. For example, in the first cycle, the reaction can proceed throughout the solution depth. However, in the second cycle, the reaction is only observed in the RBL, where there is a high supply of OH from the plasma gas. The disadvantage of 1D calculations is that they require significant computational time. Therefore, in this investigation, we only obtain data for 0.1 s.

The third investigation aims to complement the first and second investigations by examining the effects of charged species and pulse injection on a PBS-like solution. The plasma generator employed is a pulsed helium plasma. The charged

species assumed to enter the solution are e^-, He^+, and $He_2{}^+$. The particle flux of each species is obtained from simulations based on the Particle-in-Cell/Monte Carlo Collision (PIC/MCC) method.

The charged species flux generated from the PIC/MCC calculations is assumed to completely penetrate the PBS-like solution. We employ 1D reaction-transport simulation and a global model to investigate the generated species and reaction pathways within the PBS-like solution. 1D reaction-transport is utilized for short-time investigation with high accuracy, while the global model is employed for long-time investigation.

Four scenarios are used to understand the effects of plasma pulse on the generated species within the PBS-like solution: single pulse injection, short continuous injection, multiple pulse injection, and long continuous injection. The simulation results (1D) show that 9 species are formed within the PBS-like solution. The investigation results demonstrate that although the plasma gas injection is performed with a pulse, the species produced in the PBS-like solution are the same as those with continuous injection if the total flux is equal.

In the simulation using the global model, which is a time extension of the 1D simulation, the dominant species in the PBS-like solution are $Cl_2{}^-$, Na, HOCl, and H_2O_2. However, the concentrations of $Cl_2{}^-$ and Na reach equilibrium after 0.3 s, while the concentrations of HOCl and H_2O_2 continue to increase and their production continues. Therefore, HOCl and H_2O_2 are the dominant species if the simulation runs for a longer time.

From the three investigations, it can be concluded that the interaction of plasma with a liquid has been thoroughly studied using a global model and 1D reaction-transport simulation. The interaction of neutral gas supplied by the plasma with the PBS-like solution was studied in the first and second investigations. In contrast, the interaction of charged species with the PBS-like solution was studied in the third investigation. These three investigations provide a comprehensive understanding of the reactions of gas species produced by plasma with a chlorine-containing solution. A set of important and influential chemical reactions in the solution has also been obtained, particularly regarding the decomposition of H_2O_2 by a chlorine-containing solution. Moreover, the effect of charged species on a chlorine-containing solution can produce dominant species (H_2O_2 and HOCl).

The most critical aspect of this research is the investigation of the H_2O_2 loss mechanism in plasma-irradiated PBS solution. The mitigation of bactericidal effects resulting from the loss of H_2O_2 may be of interest to the plasma medicine community. With this understanding, the plasma medicine community can more accurately estimate the amount of H2O2 that will be decomposed by ClO/ClO^- in PBS.

From a scientific standpoint, this study reveals that H_2O_2 decomposition is not solely mediated by ClO^-, as is commonly understood, but is also driven by ClO at a high rate and over a very short timescale. This phenomenon has thus far eluded experimental observation. Furthermore, our findings demonstrate that even when only charged species are injected into the PBS, stable species such as H_2, H_2O_2, and HOCl can still be found within the solution.

Bibliography

[1] Ndrl/nist solution kinetics database on the web, 2021.

[2] L. C. Adam, I. Fabian, K. Suzuki, and G. Gordon. Hypochlorous acid decomposition in the ph 5-8 region. *Inorg. Chem.*, 31(17):3534–3541, 8 1992.

[3] I. Adamovich, S. Agarwal, E. Ahedo, L. L. Alves, S. Baalrud, N. Babaeva, A. Bogaerts, A. Bourdon, P. J. Bruggeman, C. Canal, E. H. Choi, S. Coulombe, Z. Donko, D. B. Graves, S. Hamaguchi, D. Hegemann, M. Hori, H.-H. Kim, G. M. W. Kroesen, M. J. Kushner, A. Laricchiuta, X. Li, T. E. Magin, S. M. Thagard, V. Miller, A. B. Murphy, G. S. Oehrlein, N. Puac, R. M. Sankaran, S. Samukawa, M. Shiratani, M. imek, N. Tarasenko, K. Terashima, E. T. Jr, J. Trieschmann, S. Tsikata, M. M. Turner, I. J. van der Walt, M. C. M. van de Sanden, and T. von Woedtke. The 2022 plasma roadmap: low temperature plasma science and technology. *Journal of Physics D: Applied Physics*, 55(37):373001, jul 2022.

[4] I. Adamovich and others. The 2017 plasma roadmap: Low temperature plasma science and technology. *Journal of Physics D: Applied Physics*, 50(32):323001, 2017.

[5] H. Akiyama, T. Sakugawa, T. Namihira, K. Takaki, Y. Minamitani, and N. Shimomura. Industrial applications of pulsed power technology. *IEEE Transactions on Dielectrics and Electrical Insulation*, 14(5):1051–1064, 2007.

[6] J. Albrich and J. Hurst. Oxidative inactivation of escherichia coli by hypochlorous acid: rates and differentiation of respiratory from other reaction sites. *FEBS letters*, 144(1):157–161, 1982.

[7] M. L. Alegre, M. Geronés, J. A. Rosso, S. G. Bertolotti, A. M. Braun, D. O. Mártire, and M. C. Gonzalez. Kinetic study of the reactions of chlorine atoms and cl2 • - radical anions in aqueous solutions. 1. reaction with benzene. *The Journal of Physical Chemistry A*, 104(14):3117–3125, 2000.

[8] Z. V. B. Alfassl, R. E. Huie, S. Mo~eri, and P. Neta. Kinetics of one-electron oxidation by the ClO radical. *Radiat. Phys. Chem*, 32(I):85–88, 1988.

[9] E. Alfianto, K. Ikuse, Z. Donko, and S. Hamaguchi. Numerical simulation of chemical reactions in pbs-like solution exposed to atmospheric-pressure plasmas. *Bulletin of the American Physical Society*, 2022.

[10] E. Alfianto, K. Ikuse, Z. Donkó, and S. Hamaguchi. Numerical simulation of chemical reactions in phosphate-buffered saline (pbs) exposed to helium pulsed plasmas at atmospheric pressure. *Jpn. J. Appl. Phys.*, 64(046002):046002, 2025.

[11] E. Alfianto, K. Ikuse, and S. Hamaguchi. Global numerical simulation of chemical reactions in phosphate-buffered saline (pbs) exposed to atmospheric-pressure plasmas. *Plasma Sources Science and Technology*, 32(8):085014, 2023.

[12] A. Ando, T. Asano, M. A. Sayed, R. Tero, K. Kitano, T. Urisu, and S. Hamaguchi. Extracellular matrix patterning for cell alignment by atmospheric pressure plasma jets. *Japanese Journal of Applied Physics*, 51(3R):036201, feb 2012.

[13] A. Ando, H. Uno, T. Urisu, and S. Hamaguchi. Grid-pattern formation of extracellular matrix on silicon by low-temperature atmospheric-pressure plasma jets for neural network biochip fabrication. *Applied Surface Science*, 276:1–6, 2013.

[14] H. Aoki, K. Kitano, and S. Hamaguchi. Plasma generation inside externally supplied ar bubbles in water. *Plasma Sources Science and Technology*, 17(2):025006, mar 2008.

[15] S. Aryal and G. Bisht. New paradigm for a targeted cancer therapeutic approach: a short review on potential synergy of gold nanoparticles and cold atmospheric plasma. *Biomedicines*, 5(3):38, 2017.

[16] P. Attri, K. Ishikawa, T. Okumura, K. Koga, and M. Shiratani. Plasma agriculture from laboratory to farm: A review. *Processes*, 8(8):1002, 2020.

[17] G. Bauer. Cold atmospheric plasma and plasma-activated medium: Antitumor cell effects with inherent synergistic potential. *Plasma Medicine*, 9(1):57–88, 2019.

[18] G. Bauer and D. B. Graves. Mechanisms of selective antitumor action of cold atmospheric plasma-derived reactive oxygen and nitrogen species. *Plasma Processes and Polymers*, 13(12):1157–1178, 12 2016.

[19] K. H. Becker, J. Kleffmann, R. Kurtenbach, and P. Wiesen. Solubility of nitrous acid (hono) in sulfuric acid solutions. *The Journal of Physical Chemistry*, 100(36):14984–14990, 1 1996.

[20] J. Benedikt, M. M. Hefny, A. Shaw, B. Buckley, F. Iza, S. Schäkermann, and J. Bandow. The fate of plasma-generated oxygen atoms in aqueous solutions: non-equilibrium atmospheric pressure plasmas as an efficient source of atomic o (aq). *Physical Chemistry Chemical Physics*, 20(17):12037–12042, 2018.

[21] T. Bernhardt, M. L. Semmler, M. Schäfer, S. Bekeschus, S. Emmert, and L. Boeckmann. Plasma medicine: Applications of cold atmospheric pressure plasma in dermatology. *Oxidative medicine and cellular longevity*, 2019, 2019.

[22] B. H. Bielski. A pulse radiolysis study of the reaction of ozone with Cl_2^- in aqueous solution. *Radiat. Phys. Chem.*, 41(3):527–530, 3 1993.

[23] B. H. J. Bielski and H. W. Richter. A study of the superoxide radical chemistry by stopped-flow radiolysis and radiation induced oxygen consumption. *J. Am. Chem. Soc.*, 99(9):3019–3023, 4 1977.

[24] E. Bjergbakke, S. Navaratnam, B. J. Parsons, and A. J. Swallow. Reaction between HO_2 and chlorine in aqueous solution. *J. Am. Chem. Soc.*, 103(19):5926–5928, 9 1981.

[25] G. Black, T. G. Slanger, G. A. St John, R. A. Young, J. Chem, M. J. Bevan, D. Husain, J. Photochem, A. B. Callear, R. J. Oldman, T. Faraday Soc, P. P. Sorokin, J. R. Lankard, V. L. Moruzzi, E. C. Hammond, H. Bamford, D. L. Levi, D. M. Newitt, J. Chem Soc, R. J. Field, R. M. Noyes, and D. Postlethwaite. Dissociation energies and spectra of diatomic mole-cules. Technical Report 13, Department of Chemistry, Mellon Instituteof Science, Carnegie-Mellon University, Pennsylvania, 1973.

[26] L. Boeckmann, M. Schäfer, T. Bernhardt, M. L. Semmler, O. Jung, G. Ojak, T. Fischer, K. Peters, B. Nebe, B. Müller-Hilke, et al. Cold atmospheric pressure plasma in wound healing and cancer treatment. *Applied Sciences*, 10(19):6898, 2020.

[27] A. Bogaerts, M. Yusupov, J. Razzokov, and J. Van der Paal. Plasma for cancer treatment: How can rons penetrate through the cell membrane? answers from computer modeling. *Frontiers of Chemical Science and Engineering*, 13(2):253–263, 2019.

[28] D. Boonyawan and C. Chutsirimongkol. Cold atmospheric plasma sources—an upcoming innovation in plasma medicine. In *Plasma Science and Technology for Emerging Economies*, pages 659–691. Springer, 2017.

[29] C. Bradu, K. Kutasi, M. Magureanu, and N. P. S. Zivkovic. Reactive nitrogen species in plasma-activated water: generation, chemistry and application in agriculture. *Journal of Physics D: Applied Physics*, 53(22):223001, apr 2020.

[30] P. Bruggeman, M. J. Kushner, B. R. Locke, J. G. Gardeniers, W. Graham, D. B. Graves, R. Hofman-Caris, D. Maric, J. P. Reid, E. Ceriani, et al. Plasma–liquid interactions: a review and roadmap. *Plasma sources science and technology*, 25(5):053002, 2016.

[31] P. J. Bruggeman, R. R. Frontiera, U. R. Kortshagen, M. J. Kushner, S. Linic, G. C. Schatz, H. Andaraarachchi, S. Exarhos, L. O. Jones, C. M. Mueller,

C. C. Rich, C. Xu, Y. Yue, and Y. Zhang. Plasma-driven solution electrolysis. *Journal of Applied Physics*, 129(20):200902, 5 2021.

[32] S. Bulut and K. A. Karatzas. Inactivation of escherichia coli k12 in phosphate buffer saline and orange juice by high hydrostatic pressure processing combined with freezing. *LWT*, 136:110313, 2021.

[33] W. G. Burns and P. B. Moore. Water radiolysis and its effect upon in-reactor zircaloy corrosion. *Radiation Effects*, 30(4):233–242, 1 1976.

[34] G. V. Buxton. Pulse radiolysis of aqueous solutions. some rates of reaction of OH and O^- and ph dependence of the yield of O_3^-. *Trans. Faraday Soc.*, 65:2150, 1969.

[35] G. V. Buxton, C. L. Greenstock, W. P. Helman, and A. B. Ross. Critical review of rate constants for reactions of hydrated electrons, hydrogen atoms and hydroxyl radicals (oh/O^-)in aqueous solution. *J. Phys. Chem. Ref. Data*, 17(2):513–886, 4 1988.

[36] G. V. Buxton and M. S. Subhani. Radiation chemistry and photochemistry of oxychlorine ions. *J. Chem. Soc. Faraday Trans. 1*, 68:947–957, 10 1972.

[37] X. Cai and C. Du. Thermal plasma treatment of medical waste. *Plasma Chemistry and Plasma Processing*, 41:1–46, 2021.

[38] W. L. Chameides. The photochemistry of a remote marine stratiform cloud. *Journal of Geophysical Research*, 89(D3):4739, 1984.

[39] C. Chen, F. Li, H. Chen, and M. Kong. Aqueous reactive species induced by a pcb surface micro-discharge air plasma device: a quantitative study. *Journal of Physics D: Applied Physics*, 50, 2017.

[40] F. F. Chen et al. *Introduction to plasma physics and controlled fusion*, volume 1. Springer, 1984.

[41] A. Chirokov, A. Gutsol, and A. Fridman. Atmospheric pressure plasma of dielectric barrier discharges. *Pure and Applied Chemistry*, 77(2):487–495, 2005.

[42] M. Cho, J. Kim, J. Y. Kim, J. Yoon, and J.-H. Kim. Mechanisms of escherichia coli inactivation by several disinfectants. *Water research*, 44(11):3410–3418, 2010.

[43] R. E. Connick. The interaction of hydrogen peroxide and hypochlorous acid in acidic solutions containing chloride ion. *J. Am. Chem. Soc.*, 69(6):1509–1514, 6 1947.

[44] P. J. Cullen, J. Lalor, L. Scally, D. Boehm, V. Milosavljević, P. Bourke, and K. Keener. Translation of plasma technology from the lab to the food industry. *Plasma Processes and Polymers*, 15(2):1700085, 2018.

[45] G. Czapski, J. Holcman, and B. H. J. Bielski. Reactivity of nitric oxide with simple short-lived radicals in aqueous solutions. *J. Am. Chem. Soc.*, 116(25):11465–11469, 12 1994.

[46] G. Da Silva, B. Z. Dlugogorski, and E. M. Kennedy. Elementary reaction step model of the n-nitrosation of ammonia. *Int. J. Chem. Kinet.*, 39(12):645–656, 12 2007.

[47] M. Daniels and E. E. Wigg. Radiation chemistry of the aqueous nitrate system. i. gamma ragiolysis of dilute solutions. *J. Phys. Chem.*, 71:1024–1033, 1967.

[48] L. F. de Lima, A. L. Ferreira, M. D. Torres, W. R. de Araujo, and C. de la Fuente-Nunez. Minute-scale detection of sars-cov-2 using a low-cost biosensor composed of pencil graphite electrodes. *Proceedings of the National Academy of Sciences*, 118(30):e2106724118, 2021.

[49] D. Dobrynin, K. Arjunan, A. Fridman, G. Friedman, and A. M. Clyne. Direct and controllable nitric oxide delivery into biological media and living cells by a pin-to-hole spark discharge (phd) plasma. *Journal of Physics D: Applied Physics*, 44(7):075201, 2 2011.

[50] Z. Donkó, A. Derzsi, M. Vass, B. Horváth, S. Wilczek, B. Hartmann, and P. Hartmann. edupic: an introductory particle based code for radio-

frequency plasma simulation. *Plasma Sources Science and Technology*, 30(9):095017, 2021.

[51] Z. Donkó, S. Hamaguchi, and T. Gans. The effect of photoemission on nanosecond helium microdischarges at atmospheric pressure. *Plasma Sources Science and Technology*, 27(5):054001, 2018.

[52] Z. Draganić, A. Negrón-Mendoza, K. Sehested, S. Vujošević, R. Navarro-Gonzáles, M. Albarrán-Sanchez, and I. Draganić. Radiolysis of aqueous solutions of ammonium bicarbonate over a large dose range. *Radiat. Phys. Chem.*, 38(3):317–321, 1 1991.

[53] A. Dubinov, E. Lazarenko, and V. Selemir. Effect of glow discharge air plasma on grain crops seed. *IEEE Transactions on Plasma Science*, 28(1):180–183, 2000.

[54] R. C. Dunn and J. D. Simon. Excited-state photoreactions of chlorine dioxide in water. *J. Am. Chem. Soc*, 114:4856–4860, 1992.

[55] J. L. Durham, J. H. Overton, and V. P. Aneja. Influence of gaseous nitric acid on sulfate production and acidity in rain. *Atmospheric Environment (1967)*, 15(6):1059–1068, 1 1981.

[56] J. Ehlbeck, U. Schnabel, M. Polak, J. Winter, T. von Woedtke, R. Brandenburg, T. von dem Hagen, and K.-D. Weltmann. Low temperature atmospheric pressure plasma sources for microbial decontamination. *Journal of Physics D: Applied Physics*, 44(1):013002, dec 2010.

[57] A. S. El Din and R. Mohammed. Kinetics of the reaction between hydrogen peroxide and hypochlorite. *Desalination*, 115(2):145–153, 1998.

[58] A. J. Elliot. A pulse radiolisys study of the temperature dependence of reactions involving H, OH, and e^-_{aq} in aqueous solutions. *Radiat. Phys. Chem.*, 34(5):753–758, 1989.

[59] A. J. Elliot, D. R. McCracken, G. V. Buxton, and N. D. Wood. Estimation of rate constants for near-diffusion-controlled reactions in water at high temperatures. *J. Chem. Soc. Faraday Trans.*, 86(9):1539, 1990.

[60] T. E. Eriksen, J. Lind, and G. Merényi. Generation of chlorine dioxide from ClO_2^- by pulse radiolysis. *J. Chem. Soc. Faraday Trans. 1*, 77(9):2115, 1981.

[61] B. G. Ershov, E. Janata, A. Henglein, and A. Fojtik. Silver atoms and clusters in aqueous solution: Absorption spectra and the particle growth in the absence of stabilizing Ag^+ ions. *J. Phys. Chem.*, 97(18):4589–4594, 5 1993.

[62] M. Exner, H. Herrmann, and R. Zellner. Rate constants for the reactions of the NO_3 radical with $HCOOH/HCOO^-$ and CH_3COOH/CH_3COO^- in aqueous solution between 278 and 328 k. *J. Atmos. Chem.*, 18(4):359–378, 5 1994.

[63] F. Förster. Atmospheric pressure plasma in industrial applications: Surface treatment of thermally sensitive polymers. *Plasma Processes and Polymers*, 19(10):2100240, 2022.

[64] J. E. Foster. Plasma-based water purification: Challenges and prospects for the future. *Physics of Plasmas*, 24(5):055501, 2017.

[65] A. Fridman and G. Friedman. *Plasma Medicine*. Wiley, New York, 2012.

[66] S. Fukuzaki. Mechanisms of actions of sodium hypochlorite in cleaning and disinfection processes. *Biocontrol science*, 11(4):147–157, 2006.

[67] H. Furusho, K. Kitano, S. Hamaguchi, and Y. Nagasaki. Preparation of stable water-dispersible pegylated gold nanoparticles assisted by nonequilibrium atmospheric-pressure plasma jets. *Chemistry of Materials*, 21(15):3526–3535, 2009.

[68] H. Furusho, D. Miyamoto, Y. Nagasaki, K. Kitano, and S. Hamaguchi. Synthesis of uniformly dispersed metal nanoparticles with dispersion stability by nonequilibrium atmospheric plasma jets. *Journal of Photopolymer Science and Technology*, 20(2):229–233, 2007.

[69] Y. Gao, K. Francis, and X. Zhang. Review on formation of cold plasma activated water (paw) and the applications in food and agriculture. *Food Research International*, 157:111246, 2022.

[70] S. Goldstein and G. Czapski. The reaction of NO with O_2^- and HO_2: a pulse radiolysis study. *Free Radical Biology and Medicine*, 19(4):505–510, 2 1995.

[71] S. Goldstein, J. Lind, and G. Merényi. Chemistry of peroxynitrites as compared to peroxynitrates. *Chem. Rev.*, 105(6):2457–2470, 6 2005.

[72] S. Goldstein and G. Merényi. The chemistry of peroxynitrite: Implications for biological activity. In *Methods in Enzymology*, volume 436, pages 49–61. Academic Press Inc., 2008.

[73] R. Gopalakrishnan, E. Kawamura, A. J. Lichtenberg, M. A. Lieberman, and D. B. Graves. Solvated electrons at the atmospheric pressure plasma-water anodic interface. *Journal of Physics D: Applied Physics*, 49(29), 7 2016.

[74] A. V. Gordeev and B. G. Ershov. Simulation of radiation - chemical transformations in aqueous nitric oxide and nitrite solutions. *High Energy Chem.*, 45(3):188–195, 5 2011.

[75] S. Gordon, E. J. Hart, M. S. Matheson, J. Rabani, and J. K. Thomas. Reactions of the hydrated electron. *Discuss. Faraday Soc.*, 36:193–205, 1963.

[76] D. B. Graves. The emerging role of reactive oxygen and nitrogen species in redox biology and some implications for plasma applications to medicine and biology. *Journal of Physics D: Applied Physics*, 45(26):263001, jun 2012.

[77] D. B. Graves. The emerging role of reactive oxygen and nitrogen species in redox biology and some implications for plasma applications to medicine and biology. *Journal of Physics D: Applied Physics*, 45(26):263001, 2012.

[78] W. R. Haag and J. Hoigné. Ozonation of water containing chlorine or chloramines. *Water Res*, 17(10):1397–1402, 1983.

[79] J. Halpern and J. RabanP. Reactivity of hydrogen atoms toward some cobalt (111) complexes in aqueous solutions. *J. Am. Chem. SOC*, 86(4):26, 10 1966.

[80] S. Hamaguchi. Chemically reactive species in liquids generated by atmospheric-pressure plasmas and their roles in plasma medicine. In *AIP Conference Proceedings*, volume 1545, pages 214–222, 2013.

[81] D. R. Hanson, J. B. Burkholder, C. J. Howard, and A. R. Ravishankara. Measurement of hydroxyl and hydroperoxy radical uptake coefficients on water and sulfuric acid surfaces. *The Journal of Physical Chemistry*, 96(12):4979–4985, 6 1992.

[82] H. Hara and T. Adachi. Molecular mechanisms of non-thermal atmospheric pressure plasma-induced cellular responses. *Japanese Journal of Applied Physics*, 60(2):020501, 2021.

[83] E. J. Hart. Radiation chemistry of aqueous solutions. *Annual Review of Nuclear and Particle Science*, 15(Volume 15, 1965):125–150, 1965.

[84] K. Hasegawa and P. Neta. Rate constants and mechanisms of reaction of Cl_2^- radicals. *J. Phys. Chem.*, 82(8):854–857, 4 1978.

[85] W. Hayduk and H. Laudie. Prediction of diffusion coefficients for nonelectrolytes in dilute aqueous solutions. *AIChE Journal*, 20(3):611–615, 5 1974.

[86] H. Herrmann, B. Ervens, H.-W. Jacobi, R. Wolke, P. Nowacki, and R. Zellner. Capram2.3: A chemical aqueous phase radical mechanism for tropospheric chemistry. *J. Atmos. Chem.*, 36:231–284, 2000.

[87] H. Herrmann, M. Exner, and R. Zellner. Reactivity trends in reactions of the nitrate radical (NO_3) with inorganic and organic cloudwater constituents. *Geochimica et Cosmochimica Acta*, 58(15):3239–3244, 2 1994.

[88] M.-A. Hervé du Penhoat, T. Goulet, Y. Frongillo, M.-J. Fraser, P. Bernat, and J.-P. Jay-Gerin. Radiolysis of liquid water at temperatures up to 300 °c: A monte carlo simulation study. *The Journal of Physical Chemistry A*, 104(50):11757–11770, 12 2000.

[89] B. Hickel and K. Sehested. Activation energies for the reactions oxide + hydrogen and oxide + deuterium in aqueous solution. *J. Phys. Chem*, 95:744–747, 7 1991.

[90] J. Hoigné and H. Bader. Rate constants of reactions of ozone with organic and inorganic compounds in water - ii dissociating organic compounds. *Water Res.*, 17(2):185–194, 1 1983.

[91] J. Hoigne and H. Bader. Kinetics of reactions of chlorine dioxide (oclo) in water - i. rate constants for inorganic and organic compounds. *War. Res*, 28(1):45–55, 1994.

[92] J. Hoigné, H. Bader, W. R. Haag, and J. Staehelin. Rate constants of reactions of ozone with organic and inorganic compounds in water -{iii}. *Water Res*, 19(8):993–1004, 5 1985.

[93] Q. Huang, H. Wang, C. Liu, Y. Wu, M. A. Bashir, and C. Shao. Application of chloride in cold atmospheric plasma jet (capj) and plasma-activated solution (pas) to enhance virus inactivation. *Plasma Medicine*, 13(2):47–63, 2023.

[94] R. E. Huie, C. L. Clifton, and P. Neta. Electron transfer reaction rates and equilibria of the carbonate and sulfate radical anions. *Radiat. Phys. Chem.*, 38(5):477–481, 1 1991.

[95] R. E. Huie, P. Neta, and C. P. Coord. Kinetics of one-electron transfer reactions involving ClO_2 and NO_2. *J. Chem. Soc., Chem. Commun*, 90(1):1149, 1986.

[96] S. Ikawa, K. Kitano, and S. Hamaguchi. Effects of ph on bacterial inactivation in aqueous solutions due to low-temperature atmospheric pressure plasma application. *Plasma Processes and Polymers*, 7(1):33–42, 2010.

[97] K. Ikuse and S. Hamaguchi. Simulation of reactive species: Kinetics in aqueous phase. In *Plasma Medical Science*, pages 100–107. Elsevier, 1 2018.

[98] K. Ikuse and S. Hamaguchi. Roles of the reaction boundary layer and long diffusion of stable reactive nitrogen species (RNS) in plasma-irradiated water as an oxidizing media — Numerical simulation study . *Jpn. J. Appl. Phys.*, 61:076002 (pp.22), 2022.

[99] Y. Ilan and J. Rabani. On some fundamental reactions in radiation chemistry: Nanosecond pulse radiolysis. *Int. J. Radiat. Phys. Chem.*, 8(5):609–611, 1 1976.

[100] M. Ito, J.-S. Oh, T. Ohta, M. Shiratani, and M. Hori. Current status and future prospects of agricultural applications using atmospheric-pressure plasma technologies. *Plasma Processes and Polymers*, 15(2):1700073, 2018.

[101] T. Ito, K. Gotoh, K. Sekimoto, and S. Hamaguchi. Mass spectrometry analyses of ions generated by atmospheric-pressure plasma jets in ambient air. *Plasma Medicine*, 5(2-4):283–298, 2015.

[102] H. Jablonowski, R. Bussiahn, M. U. Hammer, K. D. Weltmann, T. Von Woedtke, and S. Reuter. Impact of plasma jet vacuum ultraviolet radiation on reactive oxygen species generation in bio-relevant liquids. *Physics of Plasmas*, 22(12), 12 2015.

[103] M. Jinno, S. Satoh, Y. Ikeda, and H. Motomura. The new technology of molecular and gene introduction method using discharge plasma: plasma brings features of random genome integration-free and damage-free to cells, genomic-dna and external introducing molecules. *Japanese Journal of Applied Physics*, 2021.

[104] V. Jirásek and P. Lukeš. Formation of reactive chlorine species in saline solution treated by non-equilibrium atmospheric pressure he/o ₂ plasma jet. *Plasma Sources Science and Technology*, 28(3):035015, 3 2019.

[105] S. Kanazawa, M. Kogoma, T. Moriwaki, and S. Okazaki. Stable glow plasma at atmospheric pressure. *Journal of Physics D: Applied Physics*, 21(5):838, may 1988.

[106] T. Kareem and A. Kaliani. Glow discharge plasma electrolysis for nanoparticles synthesis. *Ionic*, 18:315–327, 2012.

[107] Y. Katsumura, P. Y. Jiang, R. Nagaishi, T. Oishi, K. Ishigure, and Y. Yoshida. Pulse radiolysis study of aqueous nitric acid solutions. formation mechanism, yield, and reactivity of NO_3 radical. *J. Phys. Chem*, 95:4435–4439, 1991.

[108] M. C. Kavanaugh and R. R. Trussell. Design of aeration towers to strip volatile contaminants from drinking water. *Journal - American Water Works Association*, 72(12):684–692, 12 1980.

[109] A. Khlyustova, C. Labay, Z. Machala, M.-P. Ginebra, and C. Canal. Important parameters in plasma jets for the production of rons in liquids for plasma medicine: A brief review. *Frontiers of Chemical Science and Engineering*, 13:238–252, 2019.

[110] M. Kim, D. Song, H. Shin, S.-H. Baeg, G. Kim, J.-H. Boo, J. Han, and S. Yang. Surface modification for hydrophilic property of stainless steel treated by atmospheric-pressure plasma jet. *Surface and Coatings Technology*, 171(1-3):312–316, 2003.

[111] M. Kim, S. Yang, J.-H. Boo, and J. Han. Surface treatment of metals using an atmospheric pressure plasma jet and their surface characteristics. *Surface and coatings Technology*, 174:839–844, 2003.

[112] M. Kirsch, H. G. Korth, A. Wensing, R. Sustmann, and H. De Groot. Product formation and kinetic simulations in the ph range 1-14 account for a free-radical mechanism of peroxynitrite decomposition. *Archives Biochem. Biophys.*, 418(2):133–150, 10 2003.

[113] K. Kitano, H. Aoki, and S. Hamaguchi. Radio-frequency-driven atmospheric-pressure plasmas in contact with liquid water. *Japanese Journal of Applied Physics*, 45(10S):8294, oct 2006.

[114] U. K. Klaning, K. Sehested, and J. Holcman. Standard gibbs energy of formation of the hydroxyl radical in aqueous solution. rate constants for the reaction ClO_2^- + O_3 <-> O_3^- + ClO_2. *J. Phys. Chem*, 89:760–763, 1985.

[115] S. J. Klebanoff, A. J. Kettle, H. Rosen, C. C. Winterbourn, and W. M. Nauseef. Myeloperoxidase: a front-line defender against phagocytosed microorganisms. *Journal of leukocyte biology*, 93(2):185–198, 2013.

[116] E. M. Knipping and D. Dabdub. Modeling Cl_2 formation from aqueous nacl particles: Evidence for interfacial reactions and importance of Cl_2 decomposition in alkaline solution. *J. Geophys. Res.*, 107(18):8–1, 2002.

[117] T. Kobayashi, N. Iwata, J.-S. Oh, H. Hahizume, T. Ohta, K. Takeda, K. Ishikawa, M. Hori, and M. Ito. Bactericidal pathway of escherichia coli in buffered saline treated with oxygen radicals. *Journal of Physics D: Applied Physics*, 50(15):155208, 2017.

[118] U. Kogelschatz. Atmospheric-pressure plasma technology. *Plasma Physics and Controlled Fusion*, 46(12B):B63, nov 2004.

[119] A. Komuro, R. Ono, and T. Oda. Behaviour of oh radicals in an atmospheric-pressure streamer discharge studied by two-dimensional numerical simulation. *Journal of Physics D: Applied Physics*, 46(17):175206, apr 2013.

[120] V. S. S. K. Kondeti, U. Gangal, S. Yatom, and P. J. Bruggeman. Ag+ reduction and silver nanoparticle synthesis at the plasma-liquid interface by an rf driven atmospheric pressure plasma jet: Mechanisms and the effect of surfactant. *Journal of Vacuum Science & Technology A*, 35(6):061302, 2017.

[121] B. Kopuk, R. Gunes, and I. Palabiyik. Cold plasma modification of food macromolecules and effects on related products. *Food Chemistry*, 382:132356, 2022.

[122] U. R. Kortshagen, R. M. Sankaran, R. N. Pereira, S. L. Girshick, J. J. Wu, and E. S. Aydil. Nonthermal plasma synthesis of nanocrystals: Fundamental principles, materials, and applications. *Chemical Reviews*, 116(18):11061–11127, 2016. PMID: 27550744.

[123] L. F. Kosak-Channing and G. R. Helz. Solubility of ozone in aqueous solutions of 0-0.6 m ionic strength at 5-30.degree.c. *Environmental Science & Technology*, 17(3):145–149, 3 1983.

[124] T.-N. Ku, S.-Y. Hsu, Y.-T. Lai, S.-Y. Chang, and J.-G. Duh. Plasma-treated soybean dregs solution with various gas mixtures. *IEEE Transactions on Plasma Science*, 2023.

[125] M. J. Kushner. Modelling of microdischarge devices: plasma and gas dynamics. *Journal of Physics D: Applied Physics*, 38(11):1633, may 2005.

[126] M. J. Kushner. Modelling of microdischarge devices: plasma and gas dynamics. *Journal of Physics D: Applied Physics*, 38(11):1633, 2005.

[127] R. Laenen, T. Roth, and A. Laubereau. Novel precursors of solvated electrons in water: evidence for a charge transfer process. *Physical review letters*, 85(1):50, 2000.

[128] N. Lahoutifard, P. Lagrange, and J. Lagrange. Kinetics and mechanism of nitrite oxidation by hypochlorous acid in the aqueous phase. *Chemosphere*, 50(10):1349–1357, 2003.

[129] M. H. Lapena and C. M. A. Lopes. Improvement of aerospace thermoplastic composite adhesion to coating with dielectric barrier discharge atmospheric pressure plasma surface treatment. *Plasma Processes and Polymers*, 20(1):2200081, 2023.

[130] M. Laroussi. Sterilization of contaminated matter with an atmospheric pressure plasma. *IEEE Transactions on Plasma Science*, 24(3):1188–1191, 1996.

[131] M. Laroussi. Low temperature plasma-based sterilization: Overview and state-of-the-art. *Plasma Processes and Polymers*, 2(5):391–400, 2005.

[132] M. Laroussi. Plasma medicine: A brief introduction. *Plasma*, 1(1):47–60, 2 2018.

[133] M. Laroussi. Low temperature plasma jets: Characterization and biomedical applications. *Plasma*, 3(2):54–58, 4 2020.

[134] M. Laroussi, M. G. Kong, and G. Morfill. *Plasma medicine: applications of low-temperature gas plasmas in medicine and biology*. Cambridge University Press, 2012.

[135] Y. Lee, J. Y. Son, J. I. Kang, K. M. Park, and K. D. Park. Hydrogen peroxide-releasing hydrogels for enhanced endothelial cell activities and neo-

vascularization. *ACS applied materials & interfaces*, 10 21:18372–18379, 2018.

[136] Y.-J. Lee, C.-G. Lee, S.-J. Park, J.-K. Moon, and P. J. Alvarez. ph-dependent contribution of chlorine monoxide radicals and byproducts formation during uv/chlorine treatment on clothianidin. *Chemical Engineering Journal*, 428:132444, 2022.

[137] J. Lelieveld and P. J. Crutzen. The role of clouds in tropospheric photochemistry. *Journal of Atmospheric Chemistry*, 12(3):229–267, 4 1991.

[138] M.-T. Leu and R. Zhang. Solubilities of $CH_3c(o)o_2$ no_2 and ho_2no_2 in water and liquid h_2so_4. *Geophysical Research Letters*, 26(8):1129–1132, 4 1999.

[139] A. V. Levanov, O. Y. Isaykina, N. K. Amirova, E. E. Antipenko, and V. V. Lunin. Photochemical oxidation of chloride ion by ozone in acid aqueous solution. *Environmental Science and Pollution Research*, 22(21):16554–16569, 6 2015.

[140] D. R. Lide and G. W. Milne. *Handbook of data on common organic compounds*. CRC press, 1995.

[141] C. Lierse, J. C. Sullivan, and K. H. Schmidt. Rates of oxidation of selected actinides by Cl_2^-. *Inorg. Chem*, 26(9):1408–1410, 5 1987.

[142] A. M. Lietz and M. J. Kushner. Air plasma treatment of liquid covered tissue: Long timescale chemistry. *J. Phys. D: Appl. Phys.*, 49(42):425204, 9 2016.

[143] J. Lilie, R. Hanrahan, and A. Henglein. O^- transfer reactions of the carbonate radical anion. *Radiat. Phys. Chem.*, 11(5):225–227, 1 1978.

[144] D. X. Liu, P. Bruggeman, F. Iza, M. Z. Rong, and M. G. Kong. Global model of low-temperature atmospheric-pressure he + h2o plasmas. *Plasma Sources Science and Technology*, 19(2):025018, mar 2010.

[145] Y. Liu, D. Liu, J. Zhang, B. Sun, S. Luo, H. Zhang, L. Guo, M. Rong, and M. G. Kong. Fluid model of plasma-liquid interaction: The effect of

interfacial boundary conditions and henry's law constants. *AIP Advances*, 11(5), 5 2021.

[146] Z. C. Liu, L. Guo, D. X. Liu, M. Z. Rong, H. L. Chen, and M. G. Kong. Chemical kinetics and reactive species in normal saline activated by a surface air discharge. *Plasma Processes and Polymers*, 14(4-5):1600113, 2017.

[147] Z. C. Liu, L. Guo, D. X. Liu, M. Z. Rong, H. L. Chen, and M. G. Kong. Chemical Kinetics and Reactive Species in Normal Saline Activated by a Surface Air Discharge. *Plasma Processes and Polymers*, 14(4-5):1600113, 4 2017.

[148] Z. C. Liu, D. X. Liu, C. Chen, D. Li, A. J. Yang, M. Z. Rong, H. L. Chen, and M. G. Kong. Physicochemical processes in the indirect interaction between surface air plasma and deionized water. *Journal of Physics D: Applied Physics*, 48(49):495201, 11 2015.

[149] G. Lloyd, G. Friedman, S. Jafri, G. Schultz, A. Fridman, and K. Harding. Gas plasma: Medical uses and developments in wound care. *Plasma Processes and Polymers*, 7(3-4):194–211, 2010.

[150] B. R. Locke, M. Sato, P. Sunka, M. R. Hoffmann, and J.-S. Chang. Electrohydraulic discharge and nonthermal plasma for water treatment. *Industrial & Engineering Chemistry Research*, 45(3):882–905, 2006.

[151] B. R. Locke and K.-Y. Shih. Review of the methods to form hydrogen peroxide in electrical discharge plasma with liquid water. *Plasma Sources Science and Technology*, 20(3):034006, apr 2011.

[152] T. Løgager and K. Sehested'. Formation and decay of peroxynitrous acid: A pulse radiolysis study. *J. Phys. Chem*, 97:6664–6669, 4 1993.

[153] C. A. Long and B. H. J. Bielski. Rate of reaction of superoxide radical with chloride-containing species. *J. Phys. Chem.*, 84(5):555–557, 3 1980.

[154] P. Lukes, E. Dolezalova, I. Sisrova, and M. Clupek. Aqueous-phase chemistry and bactericidal effects from an air discharge plasma in contact with water:

Evidence for the formation of peroxynitrite through a pseudo-second-order post-discharge reaction of H_2O_2 and HNO_2. *Plasma Sources Sci. Technol.*, 23(1), 2 2014.

[155] S. Luo, Z. Liu, D. Liu, H. Zhang, L. Guo, M. Rong, and M. G. Kong. Modeling study of the indirect treatment of phosphate buffered saline in surface air plasma. *Journal of Physics D: Applied Physics*, 54(6):065203, 2 2021.

[156] S. V. Lymar and J. K. Hurst. Rapid reaction between peroxonitrite ion and carbon dioxide: Implications for biological activity. *J. Am. Chem. Soc.*, 117(34):8867–8868, 8 1995.

[157] B. Mayer, P. Klatt, E. R. Werner, and K. Schmidt. Kinetics and mechanism of tetrahydrobiopterin-induced oxidation of nitric oxide. *J. Biol. Chem.*, 270(2):655–659, 1 1995.

[158] M. Minsart, S. Van Vlierberghe, P. Dubruel, and A. Mignon. Commercial wound dressings for the treatment of exuding wounds: an in-depth physico-chemical comparative study. *Burns & trauma*, 10, 2022.

[159] S. A. Mir, M. A. Shah, and M. M. Mir. Understanding the role of plasma technology in food industry. *Food and Bioprocess Technology*, 9:734–750, 2016.

[160] T. Miura, A. Ando, K. Hirano, C. Ogura, T. Kanazawa, M. Ikeguchi, A. Seki, S. Nishihara, and S. Hamaguchi. Proliferation assay of mouse embryonic stem (es) cells exposed to atmospheric-pressure plasmas at room temperature. *Journal of Physics D: Applied Physics*, 47(44):445402, oct 2014.

[161] T. Miura, S. Hamaguchi, and S. Nishihara. Atmospheric-pressure plasma-irradiation inhibits mouse embryonic stem cell differentiation to mesoderm and endoderm but promotes ectoderm differentiation. *Journal of Physics D: Applied Physics*, 49(16):165401, mar 2016.

[162] K. Miyamoto, S. Ikehara, H. Takei, Y. Akimoto, H. Sakakita, K. Ishikawa, M. Ueda, J. ichiro Ikeda, M. Yamagishi, J. Kim, T. Yamaguchi, H. Nakanishi,

T. Shimizu, N. Shimizu, M. Hori, and Y. Ikehara. Red blood cell coagulation induced by low-temperature plasma treatment. *Archives of Biochemistry and Biophysics*, 605:95–101, 2016. Special Issue: Low-temperature plasma in biology and medicine.

[163] T. Mizuno, H. Tsuno, and H. Yamada. Development of ozone self-decomposition model for engineering design. *Ozone: Science and Engineering*, 29(1):55–63, 1 2007.

[164] L. Moravsky, B. Michalczuk, J. Hrd, S. Hamaguchi, and S. Matejcik. Monitoring of nonthermal plasma degradation of phthalates by ion mobility spectrometry. *Plasma Processes and Polymers*, 18(7):2100032, 2021.

[165] M. Mozetič. Surface modification to improve properties of materials, 2019.

[166] T. Murakami, K. Niemi, T. Gans, D. O'Connell, and W. G. Graham. Chemical kinetics and reactive species in atmospheric pressure helium-oxygen plasmas with humid-air impurities. *Plasma Sources Science and Technology*, 22(1):015003, dec 2012.

[167] T. Murakami, K. Niemi, T. Gans, D. O'Connell, and W. G. Graham. Chemical kinetics and reactive species in atmospheric pressure helium-oxygen plasmas with humid-air impurities. *Plasma Sources Science and Technology*, 22(1), 2 2013.

[168] T. Murakami, K. Niemi, T. Gans, D. O'Connell, and W. G. Graham. Afterglow chemistry of atmospheric-pressure helium-oxygen plasmas with humid air impurity. *Plasma Sources Science and Technology*, 23(2):025005, mar 2014.

[169] T. Murakami, K. Niemi, T. Gans, D. O'Connell, and W. G. Graham. Afterglow chemistry of atmospheric-pressure helium-oxygen plasmas with humid air impurity. *Plasma Sources Science and Technology*, 23(2), 2014.

[170] E. Murphy and A. Friedman. Hydrogen peroxide and cutaneous biology: Translational applications, benefits, and risks. *Journal of the American Academy of Dermatology*, 2019.

[171] Y. Nagasaki, M. Umeyama, M. Iijima, K. Kitano, and S. Hamaguchi. Design of biointerface by nonequilibrium atmospheric plasma jets-approach from plasma susceptible polymers-. *Journal of Photopolymer Science and Technology*, 21(2):267–270, 2008.

[172] A. V. Nastuta, I. Topala, C. Grigoras, V. Pohoata, and G. Popa. Stimulation of wound healing by helium atmospheric pressure plasma treatment. *Journal of Physics D: Applied Physics*, 44(10):105204, 2011.

[173] S. Nehari and J. Rabani. The reaction of H atoms with OH^- in the radiation chemistry of aqueous solutions. *J. Phys. Chem.*, 67(8):1609–1613, 8 1963.

[174] J. S. Nicoson and D. W. Margerum. Kinetics and mechanisms of aqueous chlorine reactions with chlorite ion in the presence of chloride ion and acetic acid/acetate buffer. *Inorg. Chem.*, 41(2):342–347, 1 2002.

[175] R. Nisticò, S. Lista, G. Nappi, C. Cereda, and N. Mercuri. Potential therapeutic usefulness of hydrogen peroxide in conditions of brain ischemia. *Medical hypotheses*, 71 1:162, 2008.

[176] T. Oda, A. Kumada, K. Tanaka, T. Takahashi, and S. Masuda. Low temperature atmospheric pressure discharge plasma processing for volatile organic compounds. *Journal of Electrostatics*, 35(1):93–101, 1995. Selected Papers from the 1994 Joint ESA/IEJ Symposium on Electrostatics.

[177] J.-S. Oh, E. J. Szili, S. Ito, S.-H. Hong, N. Gaur, H. Furuta, R. D. Short, and A. Hatta. Slow molecular transport of plasma-generated reactive oxygen and nitrogen species and o₂ through agarose as a surrogate for tissue. *Plasma Medicine*, 5(2-4):125–143, 2015.

[178] D. W. O'Sullivan, M. Lee, B. C. Noone, and B. G. Heikes. Henry's law constant determinations for hydrogen peroxide, methyl hydroperoxide, hydroxymethyl hydroperoxide, ethyl hydroperoxide, and peroxyacetic acid. *The Journal of Physical Chemistry*, 100(8):3241–3247, 1 1996.

[179] N. S. Pandis and J. H. Einfeld. Sensitivity analysis of a chemical mechanism for aqueous-phase atmospheric chemistry. *J. Geophys. Res.*, 94(D1):1105–1126, 1989.

[180] B. Pang, Z. Liu, H. Zhang, S. Wang, Y. Gao, D. Xu, D. Liu, and M. G. Kong. Investigation of the chemical characteristics and anticancer effect of plasma-activated water: The effect of liquid temperature. *Plasma Processes and Polymers*, 19(1):2100079, 1 2022.

[181] S. K. Pankaj, C. Bueno-Ferrer, N. Misra, V. Milosavljević, C. O'donnell, P. Bourke, K. Keener, and P. Cullen. Applications of cold plasma technology in food packaging. *Trends in Food Science & Technology*, 35(1):5–17, 2014.

[182] S. K. Pankaj, Z. Wan, and K. M. Keener. Effects of cold plasma on food quality: A review. *Foods*, 7(1):4, 2018.

[183] B. Pastina and J. A. LaVerne. Effect of molecular hydrogen on hydrogen peroxide in water radiolysis. *J. Phys. Chem. A*, 105(40):9316–9322, 10 2001.

[184] M. Pavlik and J. D. Skalny. Generation of [h3o]+.(h2o) clusters by positive corona discharge in air. *Rapid Communications in Mass Spectrometry*, 11(16):1757–1766, 1997.

[185] G. Peintler, I. Nagypal, and I. R. Epstein. Systematic design of chemical oscillators. 60. kinetics and mechanism of the reaction between chlorite ion and hypochlorous acid. *J. Phys. Chem.*, 94(7):2954–2958, 4 1990.

[186] C. Pignata, D. D'angelo, E. Fea, and G. Gilli. A review on microbiological decontamination of fresh produce with nonthermal plasma. *Journal of Applied Microbiology*, 122(6):1438–1455, 2017.

[187] R. R. Pillai and V. Thomas. Plasma surface engineering of natural and sustainable polymeric derivatives and their potential applications. *Polymers*, 15(2):400, 2023.

[188] G. A. Poskrebyshev, P. Neta, and R. E. Huie. Equilibrium constant of the reaction OH + HNO_3 <-> H_2O + NO_3 in aqueous solution. *J. Geophys. Res.*, 106(D5):4995–5004, 3 2001.

[189] N. Puač, M. Gherardi, and M. Shiratani. Plasma agriculture: A rapidly emerging field. *Plasma processes and polymers*, 15(2):1700174, 2018.

[190] B. Rao, T. A. Anderson, A. Redder, and W. A. Jackson. Perchlorate formation by ozone oxidation of aqueous chlorine/oxy-chlorine species: Role of cl x o y radicals. *Environmental Science & Technology*, 44(8):2961–2967, 4 2010.

[191] W. Rao, Y. Li, H. Dhaliwal, M. Feng, Q. Xiang, M. Roopesh, D. Pan, and L. Du. The application of cold plasma technology in low-moisture foods. *Food Engineering Reviews*, pages 1–27, 2023.

[192] J.-M. Régimbal and M. Mozurkewich. Peroxynitric acid decay mechanisms and kinetics at low ph. *The Journal of Physical Chemistry A*, 101(47):8822–8829, 11 1997.

[193] S. Reuter, T. von Woedtke, and K.-D. Weltmann. The kinpen—a review on physics and chemistry of the atmospheric pressure plasma jet and its applications. *Journal of Physics D: Applied Physics*, 51(23):233001, may 2018.

[194] F. Rezaei, P. Vanraes, A. Nikiforov, R. Morent, and N. De Geyter. Applications of plasma-liquid systems: A review. *Materials*, 12(17):2751, 2019.

[195] C. Richmonds and R. M. Sankaran. Plasma-liquid electrochemistry: Rapid synthesis of colloidal metal nanoparticles by microplasma reduction of aqueous cations. *Applied Physics Letters*, 93(13):131501, 2008.

[196] A. Rohatgi. Webplotdigitizer: Version 4.6, 2022.

[197] E. S. Rudakov, V. L. Lobachev, and Y. V. Geletii. Does peroxynitrite partition between aqueous and gas phases? implication for lipid peroxidation. *Chemical Research in Toxicology*, 14(9):1232–1238, 9 2001.

[198] P. Rumbach, D. M. Bartels, R. M. Sankaran, and D. B. Go. The effect of air on solvated electron chemistry at a plasma/liquid interface. *Journal of Physics D: Applied Physics*, 48(42), 9 2015.

[199] S. K. Saha, J. Nakanishi, K. Kitano, S. Hamaguchi, and Y. Nagasaki. Creation of biointerface by atmospheric plasma treatment of plasma sensitive polymeric materials. *Journal of Photopolymer Science and Technology*, 22(4):481–484, 2009.

[200] Y. Sakiyama, D. B. Graves, H.-W. Chang, T. Shimizu, and G. E. Morfill. Plasma chemistry model of surface microdischarge in humid air and dynamics of reactive neutral species. *Journal of Physics D: Applied Physics*, 45(42):425201, 2012.

[201] E. Samson, J. Marchand, and K. A. Snyder. Calculation of ionic diffusion coefficients on the basis of migration test results. *Materials and Structures*, 36(3):156–165, 4 2003.

[202] R. Sander. Compilation of henry's law constants (version 4.0) for water as solvent. *Atmospheric Chemistry and Physics*, 15(8):4399–4981, 4 2015.

[203] M. C. Sauer, W. G. Brown, and E. J. Hart. O(^{3}P) atom formation by the photolysis of hydrogen peroxide in alkaline aqueous solutions. *J. Phys. Chem.*, 88(7):1398–1400, 3 1984.

[204] D. L. Scharfetter and H. K. Gummel. Large-signal analysis of a silicon read diode oscillator. *IEEE Transactions on electron devices*, 16(1):64–77, 1969.

[205] S. Schüttler, A. L. Schöne, E. Jeß, A. R. Gibson, and J. Golda. Production and transport of plasma-generated hydrogen peroxide from gas to liquid. *Physical Chemistry Chemical Physics*, 2024.

[206] A. Schutze, J. Jeong, S. Babayan, J. Park, G. Selwyn, and R. Hicks. The atmospheric-pressure plasma jet: a review and comparison to other plasma sources. *IEEE Transactions on Plasma Science*, 26(6):1685–1694, 1998.

[207] H. A. Schwarz. Reaction of the hydrated electron with water. *J. Phys. Chem.*, 96(22):8937–8941, 10 1992.

[208] W. A. Seddon, J. W. Fletcher, and F. C. Sopchyshyn. Pulse radiolysis of nitric oxide in aqueous solution. *Can. J. Chem.*, 51:1123–1130, 10 1973.

[209] K. Sehested, H. Corfitzen, J. Holcman, and E. J. Hart. Decomposition of ozone in aqueous acetic acid solutions (pH 0-4). *J. Phys. Chem.*, 96(2):1005–1009, 1 1992.

[210] T. Shao, R. Wang, C. Zhang, and P. Yan. Atmospheric-pressure pulsed discharges and plasmas: mechanism, characteristics and applications. *High voltage*, 3(1):14–20, 2018.

[211] R. K. Singh, S. Fernando, S. F. Baygi, N. Multari, S. M. Thagard, and T. M. Holsen. Breakdown products from perfluorinated alkyl substances (pfas) degradation in a plasma-based water treatment process. *Environmental science & technology*, 53(5):2731–2738, 2019.

[212] B. Smaller, E. C. Avery, and J. R. Remko. Epr pulse radiolysis studies of the hydrogen atom in aqueous solution. i. reactivity of the hydrogen atom. *J. Chem. Phys.*, 55(4):2414–2418, 1971.

[213] E. Stoffels, Y. Sakiyama, and D. B. Graves. Cold atmospheric plasma: Charged species and their interactions with cells and tissues. *IEEE Transactions on Plasma Science*, 36(4):1441–1457, 2008.

[214] D. G. Storch and M. J. Kushner. Destruction mechanisms for formaldehyde in atmospheric pressure low temperature plasmas. *Journal of Applied Physics*, 73(1):51–55, 1993.

[215] S. Sumitani, H. Murotani, M. Oishi, K. Kitano, S. Hamaguchi, and Y. Nagasaki. Nonequilibrium atmospheric plasma jets assisted stabilization of drug delivery carriers: Preparation and characterization of biodegradable polymeric nano-micelles with enhanced stability. *Journal of Photopolymer Science and Technology*, 22(4):467–471, 2009.

[216] E. J. Szili, J. W. Bradley, and R. D. Short. A 'tissue model'to study the plasma delivery of reactive oxygen species. *Journal of Physics D: Applied Physics*, 47(15):152002, 2014.

[217] E. J. Szili, J.-S. Oh, S.-H. Hong, A. Hatta, and R. D. Short. Probing the transport of plasma-generated rons in an agarose target as surrogate for real

tissue: dependency on time, distance and material composition. *Journal of Physics D: Applied Physics*, 48(20):202001, apr 2015.

[218] K. Takahashi, Y. Sasaki, S. Mukaigawa, K. Takaki, T. Fujiwara, and N. Satta. Purification of high-conductivity water using gas–liquid phase discharge reactor. *IEEE Transactions on Plasma Science*, 38(10):2694–2700, 2010.

[219] H. Tanaka, M. Mizuno, K. Ishikawa, K. Nakamura, H. Kajiyama, H. Kano, F. Kikkawa, and M. Hori. Plasma-activated medium selectively kills glioblastoma brain tumor cells by down-regulating a survival signaling molecule, akt kinase. *Plasma Medicine*, 1(3-4):265–277, 2011.

[220] T. Telser and U. Schindewolf. Reaction of hydrated electrons with alkali metal cations in alkaline aqueous solutions. *J. Phys. Chem.*, 90(21):5378–5382, 10 1986.

[221] C. Tendero, C. Tixier, P. Tristant, J. Desmaison, and P. Leprince. Atmospheric pressure plasmas: A review. *Spectrochimica Acta Part B: Atomic Spectroscopy*, 61(1):2–30, 2006.

[222] J. K. Thomas, S. Gordon, and E. J. Hart. The rates of reaction of the hydrated electron in aqueous inorganic solutions. *J. Phys. Chem.*, 68(6):1524–1527, 6 1964.

[223] K. Thomas, A. Volz-Thomas, D. Mihelcic, H. G. J. Smit, and D. Kley. On the exchange of no3 radicals with aqueous solutions: Solubility and sticking coefficient. *Journal of Atmospheric Chemistry*, 29(1):17–43, 1998.

[224] W. Tian and M. J. Kushner. Atmospheric pressure dielectric barrier discharges interacting with liquid covered tissue. *J. Phys. D: Appl. Phys.*, 47(16), 4 2014.

[225] S. Toyokuni, Y. Ikehara, F. Kikka, and M. Hori, editors. *Plasma Medical Science*. Academic Press, 2018.

[226] A. Treinin, E. Hayon, M. Gratzel, A. Henglein, J. Lillis, G. Beck, and B. Bunsenges. Absorption spectra and reaction kinetics of NO_2, N_2O_3, and N_2O_4 in aqueous solution. *J. Am. Chem. Soc.*, 92(20):5821–5828, 10 1970.

[227] A. Treshchalov, S. Tsarenko, T. Avarmaa, R. Saar, A. Lohmus, A. Vanetsev, and I. Sildos. He/h₂ pulsed-discharge plasma as a tool for synthesis of surfactant-free colloidal silver nanoparticles in water. *Plasma Medicine*, 6(1):85–100, 2016.

[228] H. Turkoglu Sasmazel, M. Alazzawi, and N. Kadim Abid Alsahib. Atmospheric pressure plasma surface treatment of polymers and influence on cell cultivation. *Molecules*, 26(6):1665, 2021.

[229] B. K. Ulrik Klaning and T. Wolff. Ozone formation in laser flash photolysis of oxoacids and oxoanions of chlorine and bromine. *J. Chem. Soc. Faraday Trans. 1*, 80:2969–2979, 1984.

[230] W. Van Boxem, J. Van Der Paal, Y. Gorbanev, S. Vanuytsel, E. Smits, S. Dewilde, and A. Bogaerts. Anti-cancer capacity of plasma-treated pbs: Effect of chemical composition on cancer cell cytotoxicity. *Scientific Reports*, 7(1), 12 2017.

[231] P. Vanraes and A. Bogaerts. Plasma physics of liquids—a focused review. *Applied Physics Reviews*, 5(3):031103, 2018.

[232] P. Vanraes and A. Bogaerts. The essential role of the plasma sheath in plasma–liquid interaction and its applications—a perspective. *Journal of Applied Physics*, 129(22):220901, 2021.

[233] R. Vartak, S. M. Patil, A. Saraswat, M. Patki, N. K. Kunda, and K. Patel. Aerosolized nanoliposomal carrier of remdesivir: an effective alternative for covid-19 treatment in vitro. *Nanomedicine*, 16(14):1187–1202, 2021.

[234] H.-E. Wagner, R. Brandenburg, K. Kozlov, A. Sonnenfeld, P. Michel, and J. Behnke. The barrier discharge: basic properties and applications to surface treatment. *Vacuum*, 71(3):417–436, 2003.

[235] T. Wakida, S. Tokino, S. Niu, H. Kawamura, Y. Sato, M. Lee, H. Uchiyama, and H. Inagaki. Surface characteristics of wool and poly (ethylene terephthalate) fabrics and film treated with low-temperature plasma under atmospheric pressure. *Textile Research Journal*, 63(8):433–438, 1993.

[236] T. X. Wang and D. W. Margerum. Kinetics of reversible chlorine hydrolysis: Temperature dependence and general-acid/base-assisted mechanisms. *Inorg. Chem*, 33:1050–1055, 1994.

[237] Y. G. Wang Richard Finke, K. D. Fogelman, D. M. Walker, and D. W. Margerum. Non-metal redox kinetics: Hypochlorite and hypochlorous acid reactions with sulfite. Technical Report 26, Department of Chemistry, Purdue University, West Lafayette, Indiana, 1988.

[238] M. J. Welch, J. F. Lifton, and J. A. Seck. Tracer studies with radioactive oxygen-15. exchange between carbon dioxide and water. *J. Phys. Chem.*, 73(10), 3 1969.

[239] K. D. Weltmann, J. F. Kolb, M. Holub, D. Uhrlandt, M. Šimek, K. K. Ostrikov, S. Hamaguchi, U. Cvelbar, M. Černák, B. Locke, A. Fridman, P. Favia, and K. Becker. The future for plasma science and technology. *Plasma Processes and Polymers*, 16(1), 1 2019.

[240] K. Wende, P. Williams, J. Dalluge, W. Van Gaens, H. Aboubakr, J. Bischof, T. von Woedtke, S. M. Goyal, K.-D. Weltmann, A. Bogaerts, K. Masur, and P. J. Bruggeman. Identification of the biologically active liquid chemistry induced by a nonthermal atmospheric pressure plasma jet. *Biointerphases*, 10(2):029518, 6 2015.

[241] P. Westerhoff, R. Song, G. Amy, and R. Minear. Applications of ozone decomposition models. *Ozone Sci. Eng.*, 19(1):55–73, 1997.

[242] G. B. Wills and H.-S. Yeh. Diffusion coefficient of aqueous nitric acid at 25.deg. as function of concentration from 0.1 to 1.0m. *Journal of Chemical & Engineering Data*, 16(1):76–77, 1 1971.

[243] D. M. Wilmouth, R. J. Salawitch, and T. P. Canty. Stratospheric ozone depletion and recovery. In *Green chemistry*, pages 177–209. Elsevier, 2018.

[244] C. C. Winterbourn, A. J. Kettle, and M. B. Hampton. Reactive oxygen species and neutrophil function. *Annual review of biochemistry*, 85:765–792, 2016.

[245] D. Wu, D. Wong, and B. Di Bartolo. Evolution of Cl_2^- in aqueous nacl solutions. *J. Photochem.*, 14:303–310, 1980.

[246] Y. Yang, Y. I. Cho, and A. Fridman. *Plasma discharge in liquid: water treatment and applications*. CRC press, 2017.

[247] M. Yasir, A. K. Vijay, and M. Willcox. Antiviral effect of multipurpose contact lens disinfecting solutions against coronavirus. *Contact Lens and Anterior Eye*, 45(5):101513, 2022.

[248] H. Yasuda, T. Miura, H. Kurita, K. Takashima, and A. Mizuno. Biological evaluation of dna damage in bacteriophages inactivated by atmospheric pressure cold plasma. *Plasma Processes and Polymers*, 7(3-4):301–308, 2010.

[249] T. Yokoyama, M. Kogoma, S. Kanazawa, T. Moriwaki, and S. Okazaki. The improvement of the atmospheric-pressure glow plasma method and the deposition of organic films. *Journal of Physics D: Applied Physics*, 23(3):374, mar 1990.

[250] A. Yusuf, H. K. Amusa, J. O. Eniola, A. Giwa, O. Pikuda, A. Dindi, and M. R. Bilad. Hazardous and emerging contaminants removal from water by plasma-based treatment: a review of recent advances. *Chemical Engineering Journal Advances*, page 100443, 2023.

[251] Y. Zhang. *A new flat dark discharge lamp for backlight applications based on electron-excited-phodphor luminescence*. PhD thesis, Université Toulouse 3 Paul Sabatier (UT3 Paul Sabatier), 2014.

Appendix A

Reaction list

Table A.1: The list of chemical reaction for simulation

No	Chemical Reactions	Rate Coef.	Ref
	ROS & water reactions		
R_O001	$OH^- + H^+ \rightleftharpoons H_2O$	1.4×10^{11}, 2.6×10^{-5}	33
R_O002	$e^- + H^+ \rightleftharpoons H$	2.3×10^{10}, 3.9	183
R_O003	$e^- + H_2O \rightleftharpoons H + OH^-$	1.9×10^{1}, 2.2×10^{7}	183
R_O004	$H + H_2O \rightleftharpoons H_2 + OH$	1.1×10^{1}, 4.3×10^{7}	183
R_O005	$2\,e^- \longrightarrow H_2 + 2\,OH^-$	5.5×10^{9}	183
R_O006	$e^- + H\,(+\,H_2O) \longrightarrow H_2 + OH^-$	2.5×10^{10}	183
R_O007	$e^- + O^-\,(+\,H_2O) \longrightarrow 2\,OH^-$	2.2×10^{10}	183
R_O008	$e^- + OH \longrightarrow OH^-$	3.0×10^{10}	183
R_O009	$e^- + O_2 \longrightarrow {O_2}^-$	1.9×10^{10}	183
R_O010	$e^- + {O_2}^-\,(+\,H_2O) \longrightarrow {HO_2}^- + OH^-$	1.3×10^{10}	183
R_O011	$e^- + HO_2 \longrightarrow {HO_2}^-$	2.0×10^{10}	183
R_O012	$e^- + {HO_2}^- \longrightarrow O^- + OH^-$	3.5×10^{9}	183
R_O013	$e^- + H_2O_2 \longrightarrow OH + OH^-$	1.1×10^{10}	183
R_O014	$2\,H \longrightarrow H_2$	7.8×10^{9}	183
R_O015	$H + O^- \longrightarrow OH^-$	1.0×10^{10}	183
R_O016	$H + OH \longrightarrow H_2O$	7.0×10^{9}	183
R_O017	$H + O_2 \longrightarrow HO_2$	2.1×10^{10}	183
R_O018	$H + {O_2}^- \longrightarrow {HO_2}^-$	1.8×10^{10}	183
R_O019	$H + HO_2 \longrightarrow H_2O_2$	1.8×10^{10}	183
R_O020	$H + {HO_2}^- \longrightarrow OH + OH^-$	9.0×10^{7}	183
R_O021	$H + H_2O_2 \longrightarrow OH + H_2O$	9.0×10^{7}	183
R_O022	$H_2 + O^- \longrightarrow H + OH^-$	8.0×10^{7}	183

Continued on next page

Table A.1 – *Continued from previous page*

No	Chemical Reactions	Rate Coef.	Ref
R_O023	$H_2 + O^- \longrightarrow e^- + H_2O$	1.1×10^8	89
R_O024	$H_2 + OH \longrightarrow H + H_2O$	4.2×10^7	224
R_O025	$H_2 + O_2{}^- \longrightarrow H + HO_2{}^-$	1.0	25
R_O026	$H_2 + HO_2 \longrightarrow H + H_2O_2$	1.0	25
R_O027	$H_2 + H_2O_2 \longrightarrow H + OH + H_2O$	6.0×10^6	224
R_O028	$O + e^- \longrightarrow O^-$	1.8×10^{10}	142
R_O029	$O + OH^- \longrightarrow HO_2{}^-$	4.2×10^8	203
R_O030	$O + H_2O \longrightarrow 2\,OH$	1.3×10^4	142
R_O031	$O + HO_2{}^- \longrightarrow OH + O_2{}^-$	5.3×10^9	203
R_O032	$O + H_2O_2 \longrightarrow OH + HO_2$	1.6×10^9	203
R_O033	$O^- + H^+ \rightleftharpoons OH$	1.0×10^{11}, 1.3×10^{-1}	183
R_O034	$O^- + H_2O \rightleftharpoons OH + OH^-$	1.0×10^8, 1.3×10^{10}	183
R_O035	$2\,O^- \longrightarrow HO_2{}^- + OH^-$	1.0×10^9	183
R_O036	$O^- + OH \longrightarrow HO_2{}^-$	2.5×10^{10}	183
R_O037	$O^- + O_2{}^- \longrightarrow O_2 + 2\,OH^-$	6.0×10^8	183
R_O038	$O^- + HO_2 \longrightarrow O_2 + OH^-$	6.0×10^9	183
R_O039	$O^- + HO_2{}^- \longrightarrow O_2{}^- + OH^-$	4.0×10^8	183
R_O040	$O^- + H_2O_2 \longrightarrow O_2 + H_2O$	5.0×10^8	183
R_O041	$2\,OH \longrightarrow H_2O_2$	5.0×10^9	163
R_O042	$OH + O_2{}^- \longrightarrow O_2 + OH^-$	8.2×10^9	183
R_O043	$OH + HO_2 \longrightarrow O_2 + H_2O$	6.0×10^9	183
R_O044	$OH + HO_2{}^- \longrightarrow O_2{}^- + H_2O$	7.5×10^9	183
R_O045	$OH + H_2O_2 \longrightarrow HO_2 + H_2O$	2.7×10^7	183
R_O046	$H_2O^+ \longrightarrow OH + H^+$	3.3×10^5	142
R_O047	$O_2{}^- + H^+ \rightleftharpoons HO_2$	2.0×10^{10}, 3.2×10^5	163
R_O048	$O_2{}^- + H_2O \rightleftharpoons HO_2 + OH^-$	1.9×10^1, 5.0×10^{10}	183
R_O049	$2\,O_2{}^- (+\,2\,H_2O) \longrightarrow O_2 + H_2O_2 + 2\,OH^-$	1.0×10^2	183
R_O050	$O_2{}^- + HO_2 \longrightarrow O_2 + HO_2{}^-$	8.0×10^7	183
R_O051	$O_2{}^- + HO_2{}^- \longrightarrow O_2 + O^- + OH^-$	1.3×10^{-1}	183
R_O052	$O_2{}^- + H_2O_2 \longrightarrow O_2 + OH + OH^-$	1.3×10^{-1}	183
R_O053	$2\,HO_2 \longrightarrow O_2 + H_2O_2$	7.0×10^5	183
R_O054	$HO_2 + HO_2{}^- \longrightarrow O_2 + OH + OH^-$	5.0×10^{-1}	183
R_O055	$HO_2 + H_2O_2 \longrightarrow O_2 + OH + H_2O$	5.0×10^{-1}	183
R_O056	$HO_2{}^- + H^+ \rightleftharpoons H_2O_2$	2.0×10^{10}, 4.5×10^{-2}	163
R_O057	$HO_2{}^- + H_2O \rightleftharpoons H_2O_2 + OH^-$	5.8×10^7, 1.3×10^{10}	183
R_O058	$O_3 \rightleftharpoons O + O_2$	3.0×10^{-6}, 4.0×10^9	209
R_O059	$O_3{}^- \rightleftharpoons O^- + O_2$	3.3×10^3, 3.6×10^9	183

Continued on next page

Table A.1 – *Continued from previous page*

No	Chemical Reactions	Rate Coef.	Ref
R_O060	$O_3 + e^- \longrightarrow O_3^-$	3.6×10^{10}	183
R_O061	$O_3 + H \longrightarrow HO_3$	3.8×10^{10}	183
R_O062	$O_3 + O^- \longrightarrow O_2 + O_2^-$	5.0×10^{9}	183
R_O063	$O_3 + OH \longrightarrow O_2 + HO_2$	9.0×10^{5}	163
R_O064	$O_3 + OH^- \longrightarrow HO_2 + O_2^-$	7.0×10^{1}	163
R_O065	$O_3 + O_2^- \longrightarrow O_2 + O_3^-$	1.6×10^{9}	163
R_O066	$O_3 + HO_2^- \longrightarrow O_2 + OH + O_2^-$	2.8×10^{6}	163
R_O067	$O_3 + H_2O_2 \longrightarrow 2\,O_2 + H_2O$	6.5×10^{-3}	163
R_O068	$O_3^- + H^+ \rightleftharpoons HO_3$	5.2×10^{10}, 3.3×10^{2}	163
R_O069	$O_3^- + e^- \longrightarrow O_2 + 2\,OH^-$	1.6×10^{10}	183
R_O070	$O_3^- + H \longrightarrow O_2 + OH^-$	1.0×10^{10}	183
R_O071	$O_3^- + O^- \longrightarrow 2\,O_2^-$	7.0×10^{8}	183
R_O072	$O_3^- + OH \longrightarrow O_3 + OH^-$	2.6×10^{9}	183
R_O073	$O_3^- + OH \longrightarrow 2\,O_2^- + H^+$	6.0×10^{9}	183
R_O074	$HO_3 \longrightarrow O_2 + OH$	1.1×10^{5}	163
R_O075	$2\,HO_3 \longrightarrow 2\,O_2 + H_2O_2$	5.0×10^{9}	163
R_O076	$HO_3 + OH \longrightarrow O_2 + H_2O_2$	5.0×10^{9}	163
R_O077	$HO_3 + O_2^- \longrightarrow 2\,O_2 + OH^-$	1.0×10^{10}	163
	RNS reactions		
R_N001	$N\,(+\,H_2O) \longrightarrow NH + OH$	2.3×10^{-16}	142
R_N002	$2\,N \longrightarrow N_2$	3.0×10^{7}	142
R_N003	$NH + O_2 \longrightarrow HNO + O$	1.4×10^{8}	142
R_N004	$NH + NO \longrightarrow N_2O + H$	7.8×10^{8}	142
R_N005	$NO + e^- \longrightarrow NO^-$	2.1×10^{10}	74
R_N006	$NO + H \longrightarrow NO^- + H^+$	1.1×10^{10}	74
R_N007	$NO + OH \longrightarrow HNO_2$	1.0×10^{10}	74
R_N008	$NO + HO_2 \longrightarrow ONOOH$	3.2×10^{9}	70
R_N009	$2\,NO + O_2 \longrightarrow 2\,NO_2$	2.3×10^{6}	157
R_N010	$HNO + H \longrightarrow OH + NH$	1.3×10^{-1}	142
R_N011	$HNO + O_2 \longrightarrow HO_2 + NO$	4.8	142
R_N012	$HNO + O_3 \longrightarrow O_2 + HNO_2$	5.8×10^{6}	142
R_N013	$HNO + OH \longrightarrow NO + H_2O$	4.8×10^{10}	142
R_N014	$NO_2 + H \longrightarrow HNO_2$	1.0×10^{10}	152
R_N015	$NO_2 + OH \longrightarrow NO_3^- + H^+$	1.2×10^{10}	86
R_N016	$NO_2^- + H^+ \rightleftharpoons HNO_2$	5.0×10^{10}, 2.7×10^{7}	86
R_N017	$NO_2^- + e^- \longrightarrow NO_2^{2-}$	4.5×10^{9}	74
R_N018	$NO_2^- + H \longrightarrow NO + OH^-$	7.1×10^{8}	212

Continued on next page

Table A.1 – *Continued from previous page*

No	Chemical Reactions	Rate Coef.	Ref
R_N019	$NO_2^- + O_3 \longrightarrow O_2 + NO_3^-$	3.7×10^5	92
R_N020	$NO_2^- + O^- \longrightarrow NO_2 + 2\,OH^-$	2.5×10^8	226
R_N021	$NO_2^- + OH \longrightarrow NO_2 + OH^-$	4.5×10^9	74
R_N022	$NO_2^- + O_2^- \longrightarrow NO_2^{2-} + O_2$	5.0×10^6	1
R_N023	$NO_2^- + HO_2 \longrightarrow NO_2^{2-} + O_2 + H^+$	5.0×10^6	1
R_N024	$NO_2^- + H_2O_2 + H^+ \longrightarrow ONOOH + H_2O$	1.1×10^3	154
R_N025	$HNO_2 + H \longrightarrow NO + H_2O$	4.5×10^8	79
R_N026	$HNO_2 + O_3 \longrightarrow O_2 + NO_3^- + H^+$	2.5×10^2	92^{*b}
R_N027	$HNO_2 + OH \longrightarrow NO_2 + H_2O$	3.0×10^9	74
R_N028	$HNO_2 + NO_2^- + H^+ \longrightarrow N_2O_3 + H_2O$	3.2×10^4	46
R_N029	$NO_2^{2-} (+ H_2O) \longrightarrow NO + 2\,OH^-$	5.5×10^4	1
R_N030	$NO_3 + H_2O \rightleftharpoons HNO_3 + OH$	3.0×10^2, 8.6×10^7	188
R_N031	$NO_3 + OH^- \longrightarrow OH + NO_3^-$	9.4×10^7	86
R_N032	$NO_3 + O_2^- \longrightarrow O_2 + NO_3^-$	3.0×10^9	86
R_N033	$NO_3 + HO_2 \longrightarrow O_2 + NO_3^- + H^+$	3.0×10^9	86
R_N034	$NO_3 + H_2O_2 \longrightarrow HO_2 + NO_3^- + H^+$	7.1×10^6	87
R_N035	$NO_3 + NO_2^- \longrightarrow NO_2 + NO_3^-$	1.4×10^9	86
R_N036	$NO_3 + HNO_2 \longrightarrow NO_2 + NO_3^- + H^+$	8.0×10^6	107
R_N037	$NO_3^- + H^+ \rightleftharpoons HNO_3$	5.0×10^{10}, 1.1×10^{12}	86
R_N038	$NO_3^- + e^- \longrightarrow NO_3^{2-}$	9.7×10^9	74
R_N039	$NO_3^{2-} (+ H_2O) \longrightarrow NO_2 + 2\,OH^-$	1.0×10^5	1
R_N040	$NO_3^{2-} + O_2 \longrightarrow NO_3^- + O_2^-$	2.4×10^8	47
R_N041	$NO_3^{2-} + OH \longrightarrow NO_3^- + OH^-$	3.0×10^9	152
R_N042	$NO_3^- + H \longrightarrow HNO_3^-$	1.0×10^7	152
R_N043	$NO_3^{2-} + H^+ \longrightarrow HNO_3^-$	4.5×10^{10}	$assumed^{*c}$
R_N044	$HNO_3^- \longrightarrow NO_2 + OH^-$	2.0×10^5	152
R_N045	$ONOO^- + H^+ \rightleftharpoons ONOOH$	5.0×10^{10}, 7.9×10^3	112
R_N046	$ONOO^- \rightleftharpoons O_2^- + NO$	1.7×10^{-2}, 6.7×10^9	74
R_N047	$ONOOH \rightleftharpoons OH + NO_2$	3.5×10^{-1}, 4.5×10^9	72, 152
R_N048	$ONOO^- \longrightarrow NO_3^-$	8.0×10^{-6}	71
R_N049	$ONOO^- \longrightarrow NO_2^- + O^-$	1.0×10^{-6}	71
R_N050	$ONOO^- + OH \longrightarrow NO + O_2 + OH^-$	4.8×10^9	74
R_N051	$ONOO^- + N_2O_3 \longrightarrow 2\,NO_2 + NO_2^-$	3.1×10^8	72
R_N052	$ONOOH \longrightarrow NO_3^- + H^+$	9.0×10^{-1}	72
R_N053	$O_2NO_2^- + H^+ \rightleftharpoons HO_2NO_2$	5.0×10^{10}, 5.0×10^5	86
R_N054	$O_2NO_2^- \rightleftharpoons O_2^- + NO_2$	1.0, 4.5×10^9,	152
R_N055	$HO_2NO_2 \rightleftharpoons HO_2 + NO_2$	4.6×10^{-3}, 1.0×10^7	86

Continued on next page

Table A.1 – *Continued from previous page*

No	Chemical Reactions	Rate Coef.	Ref
R_N056	$HO_2NO_2 \longrightarrow O_2 + HNO_2$	7.0×10^{-4}	152
R_N057	$HO_2NO_2 + HNO_2 \longrightarrow 2\,{NO_3}^- + 2\,H^+$	1.2×10^{1}	152
R_N058	$N_2O + e^- \longrightarrow O^- + N_2$	9.1×10^{9}	74
R_N059	$N_2O + H \longrightarrow OH + N_2$	2.1×10^{6}	74
R_N060	$N_2O + O \longrightarrow 2\,NO$	4.0×10^{10}	142
R_N061	$N_2O + O_3 \longrightarrow 2\,O_2 + N_2$	1.0×10^{-3}	92^{*b}
R_N062	$N_2O_3 \rightleftharpoons NO + NO_2$	8.4×10^{4}, 1.1×10^{9}	72
R_N063	$N_2O_3\,(+H_2O) \longrightarrow 2\,HNO_2$	2.0×10^{3}	226
R_N064	${N_2O_3} + {OH}^- \longrightarrow HNO_2 + {NO_2}^-$	1.0×10^{8}	226
R_N065	$N_2O_4 \rightleftharpoons 2\,NO_2$	6.8×10^{3}, 4.7×10^{8}	188
R_N066	$N_2O_4\,(+H_2O) \longrightarrow HNO_2 + {NO_3}^- + H^+$	1.0×10^{3}	188
R_N067	$N_2O_5 \rightleftharpoons NO_2 + NO_3$	4.7×10^{3}, 1.7×10^{9}	142, 107
R_N068	$N_2O_5\,(+H_2O) \longrightarrow 2\,{NO_3}^- + 2\,H^+$	6.7×10^{1}	142
R_N069	$N_2O_5\,(+H_2O) \longrightarrow 2\,ONOOH$	6.7×10^{1}	142
R_N070	${N_2O_2}^- + H^+ \rightleftharpoons HN_2O_2$	9.8×10^{9}, 5.5×10^{6}	208
R_N071	${N_2O_2}^- \rightleftharpoons NO + {NO}^-$	6.6×10^{4}, 1.7×10^{9}	74
R_N072	${N_2O_2}^-\,(+H_2O) \longrightarrow N_2O + OH + {OH}^-$	3.5×10^{2}	74
R_N073	${N_2O_2}^- + NO \longrightarrow {N_3O_3}^-$	3.0×10^{6}	208
R_N074	$HN_2O_2 + NO \longrightarrow HN_3O_3$	8.0×10^{6}	208
R_N075	${N_3O_3}^- + H^+ \rightleftharpoons HN_3O_3$	6.9×10^{9}, 5.5×10^{6}	208, *assumed*^{*d}
R_N076	${N_3O_3}^- \longrightarrow N_2O + {NO_2}^-$	2.4×10^{2}	74
R_N077	$HN_3O_3 \longrightarrow N_2O + HNO_2$	1.6×10^{4}	74
	Chlorine reactions		
$R_{Cl}001$	$Cl\,(+H_2O) \rightleftharpoons HOClH$	2.5×10^{5}, 5.0×10^{4}	116
$R_{Cl}002$	$2\,Cl \longrightarrow Cl_2$	8.8×10^{7}	245
$R_{Cl}003$	$Cl + {OH}^- \longrightarrow {HOCl}^-$	1.8×10^{10}	1
$R_{Cl}004$	$Cl + HO_2 \longrightarrow {Cl}^- + O_2 + H^+$	3.1×10^{9}	179
$R_{Cl}005$	$Cl + H_2O_2 \longrightarrow {Cl}^- + HO_2 + H^+$	4.5×10^{7}	179
$R_{Cl}006$	$Cl + {ClO}^- \longrightarrow {Cl}^- + ClO$	8.2×10^{9}	1
$R_{Cl}007$	$Cl + HOCl \longrightarrow {Cl}^- + ClO + H^+$	3.0×10^{9}	1
$R_{Cl}008$	${Cl}^- + O \longrightarrow {ClO}^-$	3.0×10^{9}	*assumed*^{*e}
$R_{Cl}009$	${Cl}^- + O_3 \longrightarrow {ClO}^- + O_2$	1.5×10^{-3}	1^{*f}
$R_{Cl}010$	${Cl}^- + H_2O_2 \longrightarrow {ClO}^- + H_2O$	1.8×10^{-9}	116
$R_{Cl}011$	${Cl}^- + H_2O_2 + H^+ \longrightarrow HOCl + H_2O$	8.3×10^{-7}	116
$R_{Cl}012$	${Cl}^- + NO_3 \longrightarrow Cl + {NO_3}^-$	1.0×10^{7}	86
$R_{Cl}013$	$Cl_2 + {OH}^- \rightleftharpoons HOCl + {Cl}^-$	1.0×10^{8}, 2.0×10^{-3}	116
$R_{Cl}014$	$Cl_2\,(+H_2O) \rightleftharpoons HOCl + {Cl}^- + H^+$	2.1×10^{4}, 2.2×10^{1}	116, 236

Continued on next page

Table A.1 – *Continued from previous page*

No	Chemical Reactions	Rate Coef.	Ref
$R_{Cl}015$	$Cl_2^- \rightleftharpoons Cl + Cl^-$	6.0×10^4, 8.5×10^9	116
$R_{Cl}016$	$Cl_2^- (+ H_2O) \rightleftharpoons HOClH + Cl^-$	1.3×10^3, 8.0×10^9	116
$R_{Cl}017$	$Cl_2^- + OH^- \rightleftharpoons HOCl^- + Cl^-$	4.0×10^6, 1.0×10^4	116
$R_{Cl}018$	$Cl_2 + HO_2 \longrightarrow Cl_2^- + O_2 + H^+$	1.0×10^9	24
$R_{Cl}019$	$Cl_2 + HO_2^- \longrightarrow 2\,Cl^- + O_2 + H^+$	1.0×10^8	116
$R_{Cl}020$	$Cl_2 + H_2O_2 \longrightarrow 2\,Cl^- + O_2 + 2\,H^+$	1.8×10^2	24
$R_{Cl}021$	$2\,Cl_2^- \longrightarrow 2\,Cl^- + Cl_2$	8.7×10^8	86
$R_{Cl}022$	$Cl_2^- + H \longrightarrow 2\,Cl^- + H^+$	8.0×10^9	141
$R_{Cl}023$	$Cl_2^- + OH \longrightarrow Cl^- + HOCl$	1.0×10^9	1
$R_{Cl}024$	$Cl_2^- + O_2^- \longrightarrow 2\,Cl^- + O_2$	6.0×10^9	86
$R_{Cl}025$	$Cl_2^- + HO_2 \longrightarrow 2\,Cl^- + O_2 + H^+$	1.3×10^{10}	86
$R_{Cl}026$	$Cl_2^- + OH^- \longrightarrow 2\,Cl^- + OH$	4.0×10^6	86
$R_{Cl}027$	$Cl_2^- + H_2O_2 \longrightarrow 2\,Cl^- + HO_2 + H^+$	5.0×10^4	58
$R_{Cl}028$	$Cl_2^- + O_3 \longrightarrow Cl^- + ClO + O_2$	9.0×10^7	22^{*b}
$R_{Cl}029$	$Cl_2^- + NO_2^- \longrightarrow 2\,Cl^- + NO_2$	2.5×10^8	179
$R_{Cl}030$	$Cl_2^- + ClO_2 \longrightarrow Cl^- + 2\,ClO$	1.0×10^9	1^{*b}
$R_{Cl}031$	$ClO^- (+ H_2O) \rightleftharpoons HOCl + OH^-$	1.8×10^3, 3.0×10^9	237
$R_{Cl}032$	$2\,ClO \longrightarrow Cl + ClO_2$	2.5×10^9	1^{*b}
$R_{Cl}033$	$ClO + O_3^- \longrightarrow ClO^- + O_3$	1.0×10^9	229
$R_{Cl}034$	$ClO + ClO_2^- \longrightarrow ClO^- + ClO_2$	9.4×10^8	8
$R_{Cl}035$	$ClO^- + e^- \longrightarrow Cl^- + O^-$	7.3×10^9	1^{*g}
$R_{Cl}036$	$ClO^- + O^- (+ H_2O) \longrightarrow ClO + 2\,OH^-$	2.4×10^8	36
$R_{Cl}037$	$ClO^- + OH \longrightarrow ClO + OH^-$	8.8×10^9	36
$R_{Cl}038$	$ClO^- + H_2O_2 \longrightarrow Cl^- + O_2 + H_2O$	2.8×10^3	43
$R_{Cl}039$	$ClO^- + O_3 \longrightarrow Cl^- + 2\,O_2$	1.1×10^2	78
$R_{Cl}040$	$ClO^- + O_3 \longrightarrow ClO_2^- + O_2$	3.0×10^1	78
$R_{Cl}041$	$ClO_2 + O_3^- \rightleftharpoons ClO_2^- + O_3$	1.8×10^5, 4.0×10^6	114
$R_{Cl}042$	$ClO_2 + Cl_2^- \rightleftharpoons ClO_2^- + Cl_2$	5.2×10^9, 5.7×10^5	174
$R_{Cl}043$	$ClO_2 \longrightarrow Cl + O_2$	6.7×10^9	54
$R_{Cl}044$	$ClO_2 + O^- \longrightarrow ClO_3^-$	2.7×10^9	114
$R_{Cl}045$	$ClO_2 + OH \longrightarrow ClO_3^- + H^+$	4.0×10^9	114
$R_{Cl}046$	$ClO_2 + O_2^- \longrightarrow ClO_2^- + O_2$	3.0×10^9	95
$R_{Cl}047$	$ClO_2 + HO_2^- \longrightarrow ClO_2^- + HO_2$	1.3×10^5	91
$R_{Cl}048$	$ClO_2 + NO_2^- \longrightarrow ClO_2^- + NO_2$	1.1×10^2	91
$R_{Cl}049$	$ClO_2^- + e^- \longrightarrow ClO^- + O^-$	2.5×10^9	60
$R_{Cl}050$	$ClO_2^- + O^- (+ H_2O) \longrightarrow ClO_2 + 2\,OH^-$	2.0×10^8	36^{*g}
$R_{Cl}051$	$ClO_2^- + OH \longrightarrow ClO_2 + OH^-$	7.0×10^9	60

Continued on next page

Table A.1 – *Continued from previous page*

No	Chemical Reactions	Rate Coef.	Ref
$R_{Cl}052$	$ClO_2^- + O_2^- (+ H_2O) \longrightarrow ClO_2 + HO_2^- + OH^-$	2.0×10^1	153^{*f}
$R_{Cl}053$	$2\,HOCl \rightleftharpoons Cl_2O (+ H_2O)$	8.0×10^{-2}, 7	116
$R_{Cl}054$	$HOCl + O_2^- \longrightarrow Cl^- + O_2 + OH$	7.5×10^6	153
$R_{Cl}055$	$HOCl + HO_2^- \longrightarrow Cl^- + O_2 + H_2O$	4.4×10^7	116
$R_{Cl}056$	$2\,HOCl + ClO^- \longrightarrow 2\,Cl^- + ClO_3^- + 2\,H^+$	1.3×10^{-2}	2
$R_{Cl}057$	$2\,HOCl + ClO_2^- \longrightarrow Cl_2 + ClO_3^- + H_2O$	2.1×10^3	185
$R_{Cl}058$	$HOCl^- \rightleftharpoons OH + Cl^-$	6.1×10^9, 4.3×10^9	116
$R_{Cl}059$	$HOCl^- + H^+ \rightleftharpoons HOClH$	3.0×10^{10}, 1.0×10^8	116
$R_{Cl}060$	$ClO + H_2O_2 \longrightarrow HOCl + HO_2$	3.0×10^8	139
$R_{Cl}061$	$ClO + HO_2 \longrightarrow HOCl + O_2$	4.2×10^9	139
$R_{Cl}062$	$HClO + OH \longrightarrow ClO + H_2O$	1.4×10^8	190
	COx reactions		
R_C001	$CO_2 (+ H_2O) \rightleftharpoons H_2CO_3$	3.8×10^{-2}, 2.3×10^1	238
R_C002	$CO_2^- + HCO_3^- \rightleftharpoons CO_3^- + HCO_2^-$	2.0×10^3, 1.5×10^5	1
R_C003	$CO_2 + e^- \longrightarrow CO_2^-$	7.7×10^9	75
R_C004	$CO_2 + H \longrightarrow CO_2^- + H^+$	1.0×10^6	1
R_C005	$CO_2 + OH \longrightarrow CO_3^- + H^+$	1.0×10^6	1
R_C006	$CO_2 + ONOO^- \longrightarrow CO_3^- + NO_2$	2.9×10^4	156^{*h}
R_C007	$CO_2 + HOCl + H^+ \longrightarrow HCO_3^- + Cl_2 + H_2O$	2.7	116
R_C008	$CO_2^- + e^- (+ H_2O) \longrightarrow HCO_2^- + OH^-$	1.0×10^9	61
R_C009	$CO_2^- + O_2 \longrightarrow CO_2 + O_2^-$	4.2×10^9	99
R_C010	$CO_2^- + H_2O_2 \longrightarrow CO_2 + OH + OH^-$	6.0×10^5	207
R_C011	$CO_2^- + NO \longrightarrow NOCO_2^-$	2.9×10^9	45
R_C012	$CO_2^- + N_2O (+ H_2O) \longrightarrow CO_2 + N_2 + OH + OH^-$	1.6×10^3	1
R_C013	$CO_2^- + CO_3^- \longrightarrow CO_2 + CO_3^{2-}$	5.0×10^7	52
R_C014	$CO_3^- + H^+ \rightleftharpoons HCO_3$	5.0×10^{10}, 1.3×10^2	241
R_C015	$CO_3^- + ClO^- \rightleftharpoons CO_3^{2-} + ClO$	5.7×10^5, 6.0×10^2	94
R_C016	$2\,CO_3^- + O_2 \longrightarrow 2\,CO_2 + 2\,O_2^-$	8.1×10^9	86
R_C017	$CO_3^- + O_2^- \longrightarrow CO_3^{2-} + O_2$	6.5×10^8	86
R_C018	$CO_3^- + HO_2 \longrightarrow HCO_3^- + O_2$	6.5×10^8	86
R_C019	$CO_3^- + HO_2^- \longrightarrow CO_3^{2-} + HO_2$	3.0×10^7	116
R_C020	$CO_3^- + H_2O_2 \longrightarrow HCO_3^- + HO_2$	4.3×10^5	86
R_C021	$CO_3^- + O_3^- \longrightarrow CO_3^{2-} + O_3$	6.0×10^7	116
R_C022	$CO_3^- + NO \longrightarrow CO_2 + NO_2^-$	3.5×10^9	45
R_C023	$CO_3^- + NO_2 \longrightarrow CO_2 + NO_3^-$	1.0×10^9	143
R_C024	$CO_3^- + NO_2^- \longrightarrow CO_3^{2-} + NO_2$	6.6×10^5	86
R_C025	$CO_3^- + ClO_2^- \longrightarrow CO_3^{2-} + ClO_2$	3.4×10^7	94

Continued on next page

Table A.1 – *Continued from previous page*

No	Chemical Reactions	Rate Coef.	Ref
R_C026	$CO_3^{2-} + H^+ \rightleftharpoons HCO_3^-$	5.0×10^{10}, 2.4	86
R_C027	$CO_3^{2-} + O^- (+ H_2O) \longrightarrow CO_3^- + 2\,OH^-$	5.0×10^5	116
R_C028	$CO_3^{2-} + OH \longrightarrow CO_3^- + OH^-$	3.9×10^8	86
R_C029	$CO_3^{2-} + O_3 \longrightarrow CO_3^- + O_3^-$	1.0×10^{-1}	92^{*b}
R_C030	$CO_3^{2-} + NO_3 \longrightarrow CO_3^- + NO_3^-$	4.1×10^7	86
R_C031	$CO_3^{2-} + Cl \longrightarrow CO_3^- + Cl^-$	5.0×10^8	116
R_C032	$CO_3^{2-} + Cl_2 (+ H_2O) \longrightarrow HCO_3^- + HOCl + Cl^-$	1.4×10^5	116
R_C033	$CO_3^{2-} + Cl_2^- \longrightarrow CO_3^- + 2\,Cl^-$	2.7×10^6	116
R_C034	$HCO_2^- + e^- \longrightarrow CO_2^- + H_2 + OH^-$	8.0×10^3	207^{*b}
R_C035	$HCO_2^- + H \longrightarrow CO_2^- + H_2$	2.1×10^8	35
R_C036	$HCO_2^- + O^- \longrightarrow CO_2^- + OH^-$	1.4×10^9	34^{*b}
R_C037	$HCO_2^- + OH \longrightarrow CO_2^- + H_2O$	4.3×10^9	59
R_C038	$HCO_2^- + O_2^- \longrightarrow CO_2^- + HO_2^-$	1.0×10^{-2}	$23^{*b,*f}$
R_C039	$HCO_2^- + O_3 \longrightarrow CO_2^- + HO_3$	1.0×10^2	90^{*b}
R_C040	$HCO_2^- + NO_3 \longrightarrow CO_2^- + NO_3^- + H^+$	5.0×10^7	62
R_C041	$HCO_2^- + Cl_2^- \longrightarrow CO_2^- + 2\,Cl^- + H^+$	1.9×10^6	84
R_C042	$HCO_2^- + ClO \longrightarrow CO_2^- + HClO$	1.0×10^6	$1^{*b,*f}$
R_C043	$HCO_2^- + ClO_2 \longrightarrow CO_2^- + ClO_2^- + H^+$	6.0×10^{-4}	1^{*i}
R_C044	$HCO_3^- + H^+ \rightleftharpoons H_2CO_3$	5.0×10^{10}, 1.0×10^7	86
R_C045	$HCO_3^- + e^- \longrightarrow CO_3^- + H_2 + OH^-$	1.0×10^6	222^{*b}
R_C046	$HCO_3^- + H \longrightarrow CO_3^- + H_2$	4.4×10^4	173^{*b}
R_C047	$HCO_3^- + O_2^- \longrightarrow CO_3^- + HO_2^-$	1.5×10^6	116
R_C048	$HCO_3^- + O_3 \longrightarrow CO_3^- + HO_3$	1.0×10^{-3}	92^{*b}
R_C049	$HCO_3^- + OH \longrightarrow CO_3^- + H_2O$	1.7×10^7	86
R_C050	$HCO_3^- + Cl \longrightarrow CO_3^- + Cl^- + H^+$	2.2×10^8	116
R_C051	$HCO_3^- + Cl_2 (+ H_2O) \longrightarrow H_2CO_3 + HOCl + Cl^-$	3.2×10^3	116
R_C052	$HCO_3^- + Cl^- + HOCl \longrightarrow CO_3^{2-} + Cl_2 + H_2O$	1.2×10^{-2}	116
R_C053	$H_2CO_3 + OH \longrightarrow CO_3^- + H_2O + H^+$	7.0×10^4	116
R_C054	$NOCO_2^- + NO \longrightarrow N_2O_2^- + CO_2$	6.8×10^6	45
	Others		
R_X001	$Na^+ + e^- \longrightarrow Na$	2.0×10^4	220
R_X002	$2\,Na \longrightarrow 2\,Na^+ + H_2 + 2\,OH^-$	1.5×10^9	220

^{*a} The units of each rate constant are $M^{(1-O)}s^{-1}$ with O being the reaction order.

^{*b} Only the rate constant is given in the reference and the reaction products are assumed for this study.

^{*c} Ref. 188 lists the reaction products as $NO_2 + OH^-$,
instead of HNO_3^-. However, as HNO_3^- is known to be an intermediate of this reaction and
we have R_N044 from Ref. 188, we have assumed that this reaction

Continued on next page

Table A.1 – *Continued from previous page*

No	Chemical Reactions	Rate Coef.	Ref
produces $HNO_3{}^-$ with the rate constant of the reaction of Ref. 188 mentioned above.			
^{*d} The rate constant of the backward reaction is assumed to be the same as that of the the backward reaction of R_N070.			
^{*e} The rate constant is assumed to be similar to that of the backward reaction of $R_{Cl}058$.			
^{*f}] The rate constant is assumed based on the suggestion of the reference.			
^{*g}] The reaction "$O^{2-} + H_2O \longrightarrow 2\,OH^-$" is assumed to take place immediately. with a high rate constant.			
^{*h}] The reaction product given in the reference is assumed to decompose immediately to form the reaction products given here.			

Appendix B

Input File

Table B.1: Incident flux from Ar gas feed

No	Species	Incident flux distance 0.25cm (mol cm^{-2} s^{-1})	distance 0.8cm (mol cm^{-2} s^{-1})	distance 1cm (mol cm^{-2} s^{-1})
1	H	2.01×10^{-7}	2.82×10^{-10}	5.87×10^{-10}
2	H_2O_2	1.67×10^{-8}	2.43×10^{-8}	2.67×10^{-8}
3	HNO_2	1.13×10^{-8}	2.48×10^{-8}	2.75×10^{-8}
4	HNO_3	4.70×10^{-10}	2.44×10^{-9}	3.11×10^{-9}
5	HO_2	1.05×10^{-8}	3.03×10^{-9}	2.03×10^{-9}
6	N	5.60×10^{-8}	1.85×10^{-8}	1.15×10^{-8}
7	N_2O_5	1.68×10^{-12}	8.03×10^{-10}	1.45×10^{-10}
8	NO	5.60×10^{-8}	2.80×10^{-8}	2.53×10^{-8}
9	NO_2	2.86×10^{-9}	4.32×10^{-9}	4.51×10^{-9}
10	O	7.35×10^{-7}	4.25×10^{-8}	2.27×10^{-7}
11	O_2	1.85×10^{-7}	2.60×10^{-7}	2.03×10^{-7}
12	O_3	4.04×10^{-9}	1.46×10^{-6}	3.36×10^{-7}
13	OH	3.26×10^{-8}	9.46×10^{-9}	6.73×10^{-9}

Table B.2: Incident flux from Ar/H_2O 0.27 % gas feed

No	Species	Incident flux distance 0.25cm (mol cm^{-2} s^{-1})	distance 0.8cm (mol cm^{-2} s^{-1})	distance 1cm (mol cm^{-2} s^{-1})
1	H	5.71×10^{-8}	1.51×10^{-10}	4.02×10^{-10}
2	H_2O_2	2.34×10^{-8}	6.85×10^{-8}	6.65×10^{-8}
3	HNO_2	1.29×10^{-8}	2.25×10^{-8}	2.24×10^{-8}
4	HNO_3	6.07×10^{-10}	2.73×10^{-9}	3.21×10^{-9}
5	HO_2	1.63×10^{-8}	4.61×10^{-9}	3.03×10^{-9}
6	N	1.89×10^{-8}	1.34×10^{-8}	7.19×10^{-9}
7	N_2O_5	3.77×10^{-13}	2.75×10^{-11}	4.12×10^{-11}
8	NO	3.58×10^{-8}	2.67×10^{-8}	2.36×10^{-8}
9	NO_2	2.34×10^{-9}	4.52×10^{-9}	4.29×10^{-9}
10	O	1.09×10^{-7}	1.61×10^{-7}	1.11×10^{-7}
11	O_2	3.76×10^{-7}	3.54×10^{-7}	3.43×10^{-7}
12	O_3	9.77×10^{-10}	4.71×10^{-8}	1.19×10^{-7}
13	OH	3.72×10^{-8}	1.03×10^{-8}	6.78×10^{-9}

Table B.3: Incident flux from Ar/Air 1% gas feed

No	Species	Incident flux distance 0.25cm (mol cm^{-2} s^{-1})	distance 0.8cm (mol cm^{-2} s^{-1})	distance 1cm (mol cm^{-2} s^{-1})
1	H	5.74×10^{-8}	2.82×10^{-10}	1.88×10^{-10}
2	H_2O_2	1.37×10^{-8}	2.43×10^{-9}	1.69×10^{-8}
3	HNO_2	3.97×10^{-8}	2.48×10^{-9}	4.72×10^{-8}
4	HNO_3	3.00×10^{-9}	2.44×10^{-9}	5.14×10^{-9}
5	HO_2	5.32×10^{-9}	3.03×10^{-10}	1.04×10^{-9}
6	N	2.39×10^{-8}	1.85×10^{-8}	7.86×10^{-9}
7	N_2O_5	2.29×10^{-10}	8.03×10^{-10}	4.94×10^{-10}
8	NO	6.27×10^{-8}	2.80×10^{-8}	2.40×10^{-8}
9	NO_2	6.61×10^{-9}	4.32×10^{-9}	4.95×10^{-9}
10	O	7.93×10^{-7}	4.25×10^{-8}	1.33×10^{-7}
11	O_2	4.13×10^{-7}	2.60×10^{-7}	1.95×10^{-7}
12	O_3	2.12×10^{-8}	1.46×10^{-7}	3.37×10^{-7}
13	OH	1.76×10^{-8}	9.46×10^{-9}	3.79×10^{-9}

Table B.4: Incident flux from Ar/O_2 1% gas feed

No	Species	Incident flux distance 0.25cm (mol cm^{-2} s^{-1})	distance 0.8cm (mol cm^{-2} s^{-1})	distance 1cm (mol cm^{-2} s^{-1})
1	H	4.76×10^{-8}	1.33×10^{-10}	2.74×10^{-10}
2	H_2O_2	8.51×10^{-9}	1.16×10^{-8}	1.23×10^{-8}
3	HNO_2	3.64×10^{-9}	1.08×10^{-8}	1.22×10^{-8}
4	HNO_3	5.18×10^{-10}	1.71×10^{-9}	2.06×10^{-9}
5	HO_2	4.68×10^{-9}	1.73×10^{-9}	1.07×10^{-9}
6	N	1.23×10^{-8}	8.31×10^{-9}	4.29×10^{-9}
7	N_2O_5	9.24×10^{-12}	6.25×10^{-10}	9.39×10^{-11}
8	NO	3.14×10^{-8}	2.69×10^{-8}	2.36×10^{-8}
9	NO_2	3.34×10^{-9}	3.83×10^{-9}	4.04×10^{-9}
10	O	1.81×10^{-6}	3.91×10^{-7}	1.72×10^{-7}
11	O_2	8.10×10^{-7}	4.43×10^{-7}	2.93×10^{-7}
12	O_3	1.69×10^{-7}	3.96×10^{-7}	5.35×10^{-7}
13	OH	1.67×10^{-8}	6.75×10^{-9}	4.81×10^{-9}

Table B.5: Henry's constant

No	Species	Henry's constant (mol L^{-1} atm $^{-1}$)	Ref.	No	Species	Henry's constant (mol L^{-1} atm $^{-1}$)	Ref.
1	H	$2.63x10^{-4}$	[202]	21	HNO_2	$5.0x10^{1}$	[19]
2	H_2	$7.8x10^{-4}$	[140]	22	HNO_3	$2.1x10^{5}$	[137]
3	O	$1.3x10^{-2}$	[142]	23	ONOOH	$1.26x10^{4}$	[197]
4	O_2	$1.3x10^{-3}$	[140]	24	HO_2NO_2	$4.0x10^{1}$	[138]
5	O_3	$1.1x10^{-2}$	[123]	25	HN_2O_2	∞*	-
6	OH	$3.0x10^{1}$	[81]	26	HN_2O_3	∞*	-
7	HO_2	$5.7x10^{3}$	[192]	27	Cl	$2.33x10^{1}$	[202]
8	H_2O_2	$8.3x10^{4}$	[178]	28	Cl_2	$9.32x10^{-2}$	[202]
9	HO_3	∞*	-	29	ClO	$7.09x10^{-1}$	[202]
10	N	$6.5x10^{-4}$	[142]	30	ClO_2	1.01	[202]
11	N_2	$6.1x10^{-4}$	[108]	31	Cl_2O	$1.72x10^{1}$	[202]
12	NH	$5.97x10^{1}$	[142]	32	HOCl	$6.59x10^{2}$	[202]
13	NO	$1.9x10^{-3}$	[140]	33	HOClH	$6.59x10^{2}$*	-
14	NO_2	$1.2x10^{-2}$	[38]	34	CO	$9.5x10^{-4}$	[202]
15	NO_3	1.8	[223]	35	CO_2	$3.4x10^{-2}$	[202]
16	N_2O	$2.5x10^{-2}$	[140]	36	HCO_3	∞*	-
17	N_2O_3	$2.6x10^{1}$	[55]	37	H_2CO_3	∞*	-
18	N_2O_4	1.6	[55]				
19	N_2O_5	1.97	[202]				
20	HNO	$4.67x10^{1}$	[202]				

Table B.6: Heat velocity of every species

No	Chem. Spec.	Heat velocity (m s^{-1})
1	H	1.57×10^3
2	H_2O_2	2.70×10^2
3	HNO_2	2.30×10^2
4	HNO_3	1.98×10^2
5	HO_2	2.74×10^2
6	N	4.20×10^2
7	N_2O_5	1.51×10^2
8	NO	2.87×10^2
9	NO_2	2.32×10^2
10	O	3.93×10^2
11	O_2	2.78×10^2
12	O_3	2.27×10^2
13	OH	3.82×10^2

Table B.7: Solubility limit for liquid phase from Ar gas feed

No	Species	Incident flux distance 0.25cm (mol L^{-1})	distance 0.8cm (mol L^{-1})	distance 1cm (mol L^{-1})
1	H	2.09×10^{-12}	2.93×10^{-15}	6.12×10^{-15}
2	H_2O_2	3.19×10^{-4}	4.65×10^{-4}	5.09×10^{-4}
3	HNO_2	1.53×10^{-7}	3.35×10^{-7}	3.73×10^{-7}
4	HNO_3	3.09×10^{-5}	1.61×10^{-4}	2.05×10^{-4}
5	HO_2	1.35×10^{-5}	3.92×10^{-6}	2.63×10^{-6}
6	N	5.37×10^{-12}	1.78×10^{-12}	1.11×10^{-12}
7	N_2O_5	1.35×10^{-12}	6.49×10^{-10}	1.17×10^{-10}
8	NO	2.30×10^{-11}	1.15×10^{-11}	1.04×10^{-11}
9	NO_2	9.19×10^{-12}	1.39×10^{-11}	1.45×10^{-11}
10	O	1.51×10^{-9}	8.72×10^{-11}	4.66×10^{-10}
11	O_2	5.37×10^{-11}	7.55×10^{-11}	5.89×10^{-11}
12	O_3	1.21×10^{-11}	4.38×10^{-9}	1.01×10^{-9}
13	OH	1.59×10^{-7}	4.62×10^{-8}	3.28×10^{-8}

Table B.8: Solubility limit for liquid phase from Ar/H_2O 0.27% gas feed

No	Species	Incident flux distance 0.25cm (mol L^{-1})	distance 0.8cm (mol L^{-1})	distance 1cm (mol L^{-1})
1	H	5.95×10^{-13}	1.57×10^{-15}	4.19×10^{-15}
2	H_2O_2	4.48×10^{-4}	1.31×10^{-3}	1.27×10^{-3}
3	HNO_2	1.75×10^{-7}	3.05×10^{-7}	3.03×10^{-7}
4	HNO_3	3.99×10^{-5}	1.80×10^{-4}	2.11×10^{-4}
5	HO_2	2.11×10^{-5}	5.96×10^{-6}	3.92×10^{-6}
6	N	1.81×10^{-12}	1.29×10^{-12}	6.90×10^{-13}
7	N_2O_5	3.05×10^{-13}	2.22×10^{-11}	3.32×10^{-11}
8	NO	1.47×10^{-11}	1.09×10^{-11}	9.70×10^{-12}
9	NO_2	7.51×10^{-12}	1.45×10^{-11}	1.38×10^{-11}
10	O	2.23×10^{-10}	3.30×10^{-10}	2.27×10^{-10}
11	O_2	1.09×10^{-10}	1.03×10^{-10}	9.95×10^{-11}
12	O_3	2.94×10^{-12}	1.42×10^{-10}	3.59×10^{-10}
13	OH	1.82×10^{-7}	5.05×10^{-8}	3.31×10^{-8}

Table B.9: Solubility limit for liquid phase from Ar/Air 1% gas feed

No	Species	Incident flux distance 0.25cm (mol L^{-1})	distance 0.8cm (mol L^{-1})	distance 1cm (mol L^{-1})
1	H	5.98×10^{-13}	2.93×10^{-15}	1.96×10^{-15}
2	H_2O_2	2.61×10^{-4}	4.65×10^{-5}	3.23×10^{-4}
3	HNO_2	5.37×10^{-7}	3.35×10^{-8}	6.38×10^{-7}
4	HNO_3	1.97×10^{-4}	1.61×10^{-4}	3.38×10^{-4}
5	HO_2	6.87×10^{-6}	3.92×10^{-7}	1.34×10^{-6}
6	N	2.30×10^{-12}	1.78×10^{-12}	7.55×10^{-13}
7	N_2O_5	1.85×10^{-10}	6.49×10^{-10}	3.99×10^{-10}
8	NO	2.57×10^{-11}	1.15×10^{-11}	9.85×10^{-12}
9	NO_2	2.12×10^{-11}	1.39×10^{-11}	1.59×10^{-11}
10	O	1.63×10^{-9}	8.72×10^{-11}	2.73×10^{-10}
11	O_2	1.20×10^{-10}	7.55×10^{-11}	5.67×10^{-11}
12	O_3	6.38×10^{-11}	4.38×10^{-10}	1.01×10^{-9}
13	OH	8.57×10^{-8}	4.62×10^{-8}	1.85×10^{-8}

Table B.10: Solubility limit for liquid phase from Ar/O_2 1% gas feed

No	Species	Incident flux distance 0.25cm (mol L^{-1})	distance 0.8cm (mol L^{-1})	distance 1cm (mol L^{-1})
1	H	4.96×10^{-13}	1.39×10^{-15}	2.86×10^{-15}
2	H_2O_2	1.63×10^{-4}	2.21×10^{-4}	2.34×10^{-4}
3	HNO_2	4.92×10^{-8}	1.46×10^{-7}	1.64×10^{-7}
4	HNO_3	3.41×10^{-5}	1.12×10^{-4}	1.36×10^{-4}
5	HO_2	6.05×10^{-6}	2.24×10^{-6}	1.38×10^{-6}
6	N	1.18×10^{-12}	7.97×10^{-13}	4.12×10^{-13}
7	N_2O_5	7.47×10^{-12}	5.05×10^{-11}	7.59×10^{-11}
8	NO	1.29×10^{-11}	1.10×10^{-11}	9.70×10^{-12}
9	NO_2	1.07×10^{-11}	1.23×10^{-11}	1.30×10^{-11}
10	O	3.72×10^{-9}	8.03×10^{-10}	3.52×10^{-10}
11	O_2	2.35×10^{-10}	1.28×10^{-10}	8.51×10^{-11}
12	O_3	5.07×10^{-10}	1.19×10^{-9}	1.61×10^{-9}
13	OH	8.15×10^{-8}	3.30×10^{-8}	2.35×10^{-8}

Table B.11: Diffusion coefficient of charged species

No	Species	Diffusion coefficient ($x10^{-9}$ m^2 s^{-1})	Ref
1	aqueos electron	4.9	[59]
2	H^+	9.46	[59]
3	O^-	2.0*	-
4	O_2^-	1.75	[88]
5	O_3^-	2.0	[88]
6	OH^-	5.3	[88]
7	HO_2^-	1.4	[88]
8	H_2O^+	2.0	-
9	NO^-	2.0*	-
10	NO_2^-	1.9	[59]
11	NO_2^{2-}	2.0*	-
12	NO_3^-	1.9	[59]
13	NO_3^{2-}	2.0*	-
14	$ONOO^-$	2.0*	-
15	$O_2NO_2^-$	2.0*	-
16	$N_2O_2^-$	2.0*	-
17	$N_3O_3^-$	2.0*	-
18	Cl^-	2.03	[201]
19	Cl_2^-	2.0*	-
20	ClO^-	2.0*	-
21	ClO_2^-	2.0*	-
22	ClO_3^-	2.0*	-
23	$HOCl^-$	2.0*	-
24	CO_2^-	2.0*	-
25	CO_3^-	2.0*	-
26	CO_3^{2-}	2.0*	-
27	HCO_2^-	2.0*	-
28	HCO_3^-	2.0*	-
29	$NOCO_2^-$	2.0*	-
30	Na^+	1.33	[201]

*assumption in this study

Table B.12: Diffusion coefficient and Henry's constant of neutral species

No	Species	Diffusion Coef. ($x10^{-9}$ m^2 s^{-1})	Ref.	Henry's constant (mol L^{-1} atm $^{-1}$)	Ref.
1	H	7.0	[59]	$2.63x10^{-4}$	[202]
2	H_2	4.8	[59]	$7.8x10^{-4}$	[140]
3	O	2.0*	-	$1.3x10^{-2}$	[142]
4	O_2	2.4	[59]	$1.3x10^{-3}$	[140]
5	O_3	2.0	[88]	$1.1x10^{-2}$	[123]
6	OH	2.2	[59]	$3.0x10^{1}$	[81]
7	HO_2	2.3	[88]	$5.7x10^{3}$	[192]
8	H_2O_2	2.3	[59]	$8.3x10^{4}$	[178]
9	HO_3	2.0*	-	∞*	-
10	N	2.0*	-	$6.5x10^{-4}$	[142]
11	N_2	2.0*	-	$6.1x10^{-4}$	[108]
12	NH	2.0*	-	$5.97x10^{1}$	[142]
13	NO	2.0	[49]	$1.9x10^{-3}$	[140]
14	NO_2	2.0*	-	$1.2x10^{-2}$	[38]
15	NO_3	1.0	[188]	1.8	[223]
16	N_2O	2.11	[59]	$2.5x10^{-2}$	[140]
17	N_2O_3	2.0*	-	$2.6x10^{1}$	[55]
18	N_2O_4	2.0*	-	1.6	[55]
19	N_2O_5	2.0*	-	1.97	[202]
20	HNO	2.0*	-	$4.67x10^{1}$	[202]
21	HNO_2	2.0*	-	$5.0x10^{1}$	[19]
22	HNO_3	2.8	[242]	$2.1x10^{5}$	[137]
23	ONOOH	2.0*	-	$1.26x10^{4}$	[197]
24	HO_2NO_2	2.0*	-	$4.0x10^{1}$	[138]
25	HN_2O_2	2.0*	-	∞*	-
26	HN_2O_3	2.0*	-	∞*	-
27	Cl	2.0*	-	$2.33x10^{1}$	[202]
28	Cl_2	1.48	[85]	$9.32x10^{-2}$	[202]
29	ClO	2.0*	-	$7.09x10^{-1}$	[202]
30	ClO_2	2.0*	-	1.01	[202]
31	Cl_2O	2.0*	-	$1.72x10^{1}$	[202]
32	HOCl	2.0*	-	$6.59x10^{2}$	[202]
33	HOClH	2.0*	-	$6.59x10^{2}$*	-
34	CO	2.3	[85]	$9.5x10^{-4}$	[202]
35	CO_2	1.92	[85]	$3.4x10^{-2}$	[202]
36	HCO_3	2.0*	-	∞*	-
37	H_2CO_3	2.0*	-	∞*	-

*assumption in this study

Appendix C

Research Achievements

C.1 Research Paper

1. **Alfianto, E.**, Ikuse, K., & Hamaguchi, S., (2023). "Global numerical simulation of chemical reactions in phosphate-buffered saline (pbs) exposed to atmospheric-pressure plasmas.", Plasma Sources Science and Technology, 32(8), 085014. https://doi.org/1361-6595/aceeae

2. **Alfianto, E.**, Ikuse, K., Donkó, Z., & Hamaguchi, S., (2025). "Numerical simulation of chemical reactions in phosphate-buffered saline (PBS) exposed to helium pulsed plasmas at atmospheric pressure.", Japanese Journal of Applied Physics, 64(4), 046002. https://doi.org/10.35848/1347-4065/adc6d5

3. **Alfianto, E**, Ikuse, K., Hamaguchi, S., (2025). "Depth Profile Dynamics of Hydrogen Peroxide (H_2O_2) Decomposition in Phosphate-Buffered Saline (PBS) Solution Exposed to Plasmas – A Numerical Simulation Study." Plasma Medicine, 15(1):79–98. https://doi.org/10.1615/PlasmaMed.2025059711

C.2 Conferences and Seminars

1. "Generation of solvated electrons and water ions in phosphate-buffered saline (PBS) solutions exposed to pulsed He plasmas" Enggar Alfianto, Kazumasa Ikuse, Zoltan Donko, Satoshi Hamaguchi: The 14th EU-Japan Joint Sympo-

sium on Plasma Processing (JSPP-14), 16 to 21 April 2023, Okinawa, Japan, https://www-camt.eng.osaka-u.ac.jp/JSPP-14/

2. "One-dimensional reaction-transport simulation of chemical reactions in a pbs-like solution irradiated by atmospheric-pressure pulsed helium plasmas", Enggar Alfianto, Kazumasa Ikuse, Zoltan Donko, Satoshi Hamaguchi: Workshop on Ion Chemistry and Plasmas - Fundamentals for micro analyses in atmosphere for biological and environmental applications. Oral session (29 August - 2 September 2022). http://neon.dpp.fmph.uniba.sk/WICP2022/, Bratislava, Slovakia

3. "Numerical simulation of chemical reactions in a PBS-like solution exposed to atmospheric-pressure pulsed He plasmas" Enggar Alfianto, Kazumasa Ikuse, Zoltan Donko, Satoshi Hamaguchi: THE 22ND INTERNATIONAL VACUUM CONGRESS IVC-22, Oral session (12-16 September 2022), Sapporo, Japan, https://ivc22.org/

4. "Numerical simulation of chemical reactions in PBS-like solution exposed to atmospheric-pressure plasmas", Enggar Alfianto, Kazumasa Ikuse, Zoltan Donko, Satoshi Hamaguchi: 75th Annual Gaseous Electronics Conference, Oral session (3-7 October 2022), Sendai, Japan.

   https://www.apsgec.org/gec2022/

5. "Investigation of reactive species in NaCl solution by one-dimensional reaction-diffusion numerical simulation" Enggar Alfianto, Kazumasa Ikuse, Satoshi Hamaguchi: The 74th Annual Gaseous Electronics Conference (74th GEC) Oral session (October 4-8, 2021), as a virtual only event

   https://www.apsgec.org/gec2021/

6. "Global simulation of chemical reactions in a NaCl solution exposed to an atmospheric-pressure plasma" Enggar Alfianto, Kazumasa Ikuse, Satoshi Hamaguchi: 68th JSAP Spring Meeting (March 16-19, 2021)

   https://meeting.jsap.or.jp/jsap2021s/english

7. ”Numerical investigation of chemical reactions in NaCl solution exposed to atmospheric-pressure plasma” Enggar Alfianto, Kazumasa Ikuse, Satoshi Hamaguchi: ISPlasma2021/IC-PLANT2021 (March 7-11,2021)

   https://www.isplasma.jp/www2021/

C.3 Poster

- “Depth profiles of dominant chemical reactions in a plasma-irradiated NaCl solution obtained from reaction-transport simulation” **Enggar Alfianto**, Kazumasa Ikuse, and Satoshi Hamaguchi, RUB-Japan Workshop: Bridging the Pandemic: Reigniting Cooperation on Plasma Research, Poster Session (25 November 2021, online).

C.4 Research activities

- “3D Graphene-Coupled Aerogel Nanoarchitectures: Emerging Paradigm Toward Sustainable Applications in Fuel Cell”, Osman, S. H., Kamarudin, S. K., Jamil, M. H., **Alfianto, E.,** Shaari, N., & Zakaria, Z. (2025). Korean Journal of Chemical Engineering, 1-21.

- “Performance and Gas Emissions Analysis on Four Stroke Diesel Engine with Multi-Feedstock Biodiesel”, Sa’diyah, A., Aulatama, A. A., Ramadhan, H. D., Fairuza, M. N., & **Alfianto, E.** (2024). ksergi,2023), 60-67.

- “Internet of Things Based Air Conditioner Monitoring System”, Anaz, V. F., Sujono, H. A., Sulistyowati, R., Erwanti, N. S., & **Alfianto, E.** (2024, May).. In Prosiding Seminar Nasional Teknik Elektro, Sistem Informasi, dan Teknik Informatika (SNESTIK) (Vol. 1, No. 1, pp. 237-244). (Indonesian)

- “Load control battery strategy based on backpropagation and simulated annealing training performance”, Pambudi, W. S., Firmansyah, R. A., Dawenan, C. M., Muharom, S., Rachman, A., **Alfianto, E.**, ⋯ & Tompunu, A. N. (2024). Przeglad Elektrotechniczny, 100.

- "Alcohol Level Detection System for Bus Drivers Using TGS2620 Sensor Based on Internet of Things", Setiawan, R., Sujono, H. A., Fahruzi, A., & **Alfianto, E.** (2023, November). In Prosiding Seminar Nasional Sains dan Teknologi Terapan. (Indonesian)

C.5 Books

- "Konsep Pesawat Terbang", **E Alfianto**, NPY Nurmalasari, A Sa'diyah, A Fatkhulloh, C Wibowo, (2023), Get Press Indonesia (Indonesian)
- "Fisika Dasar Pada Industri", A Sa'diyah, R Andari, PC Wardhani, **E Alfianto**, MR Asrori, J Setiawan, (2022) Get Press Indonesia (Indonesian)